Ejosat

Cilt/Vol: - Sayı/Issue: Özel/Special Aralık/December 2017

AVRUPA BILIM & TEKNOLOJI DERGISI
EUROPEAN JOURNAL OF SCIENCE & TECHNOLOGY

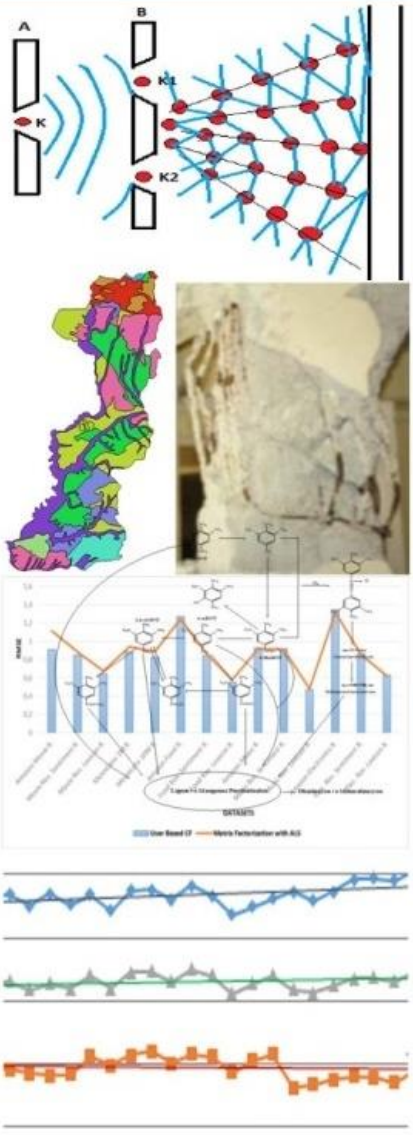

AVRUPA BİLİM & TEKNOLOJİ DERGİSİ

EUROPEN JOURNAL OF SCIENCE & TECHNOLOGY

E-posta: ejosat@gmail.com **Web Adresi:** www.ejosat.com.tr

EJOSAT dergisi hakemli bir dergi olup, senede Ocak, Mayıs ve Eylül aylarında olmak üzere yılda 3 kez yayınlanmaktadır.

Avrupa Bilim ve Teknoloji Dergisi
Özel Sayı, S. 2-6, Aralık 2017

Konferans Bildirisi

www.ejosat.com ISSN:2148-2683

European Journal of Science and Technology
SpecialIssue , pp. 2-6, December 2017

Conference Paper

Numerical Investigation of Anisotropic Electrical Conductivity Effects in Proton Exchange Membrane Fuel Cell

Gülşah Elden[1*], Mert TAŞ[2]

[1] Corresponding author: Erciyes University, Faculty of Engineering, Department of Energy Systems Engineering, Melikgazi, 38039, Kayseri, Turkey, gulsah@erciyes.edu.tr

[2] Erciyes University, Faculty of Engineering, Department of Energy Systems Engineering, Melikgazi, 38039, Kayseri, Turkey, merttas@erciyes.edu.tr

Abstract

The purpose of this study is to investigate numerically the effects of anisotropic electrical conductivity of gas diffusion layers on charge transport in Proton Exchange Membrane (PEM) fuel cell. To achieve this purpose, a single phase, three dimensional and anisotropic model is developed by using COMSOL Multiphysics 4.2a software. The numerical model is validated in experimental data which is obtained at the cell temperature of 343 K for the PEM fuel cell having 5x5 cm^2 active surface area. To find out numerically the effects of anisotropic electrical conductivity of gas diffusion layers on charge transport, two cases are examined. In the first case, the in-plane electrical conductivity of its is increased gradually as the through plane electrical conductivity is kept constant. In the second case, while the value of in-plane electrical conductivity is a constant, the through plane electrical conductivity is increased. When the both electrical conductivities are compared for all cases, the through plane conductivity has a greater effect on charge transport in PEM fuel cell than the in-plane plane electrical conductivity.

Keywords: PEM fuel cell, anisotropic electrical conductivity, numerical model.

[*] Corresponding author : Erciyes University, Engineering Faculty, Melikgazi, Kayseri, Turkey, gulsah@erciyes.edu.tr, phone: +90 352 207 6666

1. Introduction

Proton exchange membrane fuel cells (PEMFCs) are considered as a promising energy conversion technology because of their scalability, rapid start up and zero emission. Their electrochemical, mass and heat transfer phenomena have been tried to understand by computational simulations and experimental studies over the last decades. Modelling of fuel cell is used to analyse profoundly their performance and transfer phenomena. There are a wide range of PEM fuel cell numerical models in literature [Bernardi and Verbrugge (1990)-Haghayegh et al (2017)]. But anisotropic 3-D model studies are less than the others. Bapat and Thynell (2008) conducted two phase two dimensional PEMFC model operated at 353 K. The researchers tried to investigate that the effect of anisotropic electrical conductivity on current density and temperature distributions. The results of this study bring out that through plane electrical conductivity is more effective than in-plane electrical conductivity on the current density and temperature distributions. Zhou and Liu (2006) developed a 3D PEMFC model operated at 343 K. The purpose of their study is to investigate the effect of anisotropic electrical conductivity on cell performance. It is observed that increasing in-plane conductivity affects to fuel cell performance slightly. Ismail et al (2012) modelled a single phase, 3D, PEMFC model with serpentine and straight channel type. Furthermore, several cases which have different anisotropic electrical conductivities. It is shown that anisotropic electrical conductivity of gas diffusion layer influences to significantly fuel cell performance.

The main objective of this study is to investigate the effects of anisotropic electrical conductivity on electrochemical phenomena in detail. In order to achieve this objective, a single phase, three dimensional, having constant operating temperature and anisotropic PEM fuel cell model is developed and two cases are examined. In the first case [Case Group A], the in-plane electrical conductivities of gas diffusion layers are increased gradually (100 S/m, 200 S/m and 400 S/m) as the through plane electrical conductivity is kept constant (400 S/m). In the second case [Case Group B], when the value of in-plane electrical conductivity of gas diffusion layers is a constant (400 S/m), the through plane electrical conductivity is increased step by step (100 S/m, 200 S/m and 400 S/m).

2. Mathematical Modeling

The 3D PEM fuel cell model consists of seven layers which are anode channel, anode gas diffusion layer, anode catalyst layer, membrane, cathode catalyst layer, cathode gas diffusion layer and cathode channel as is shown in Figure 1.

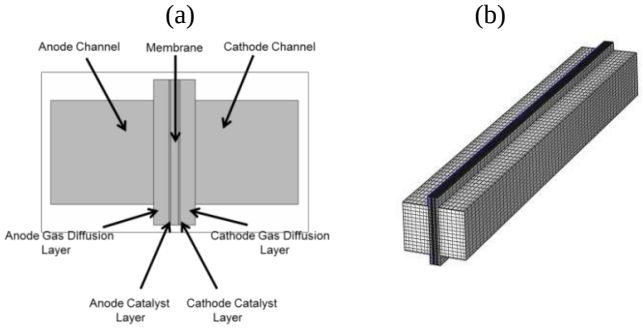

Figure 1. Schematic illustration of PEM fuel cell (a) PEM fuel cell components (b) Mesh of 3D domain.

2.1 Model Assumptions and Equations

In the presented study, to better understand the effects of anisotropic electrical conductivity on electrochemical phenomena, PEM fuel cell is modelled numerically which solves mass, momentum, species and charge conservation equations under the certain assumptions. Table 1 depicts the using conservation equations in the mathematical model. Source terms using equations and boundary conditions are given in Table 2. The following assumptions are made to reduce complexity of the model.

- Model operated at steady-state conditions.
- The porous layers are considered as homogeneous pore structure.
- In all interface, contact resistances are neglected.
- All gases are ideal gas.

Table 1. Governing Equations

Continuity equation	$\nabla(\varepsilon\rho\vec{u}) = 0$
Navier Stokes Equation	$\nabla(\varepsilon\rho u u) = -\varepsilon\nabla P + \nabla^*(\varepsilon\mu^{eff}\nabla u) + S_u$
Darcy Law	$u = -\frac{k_p}{\mu}$
Stephan-Maxwell equation	$\rho\nabla m_i = \nabla[\rho\varepsilon m_i \sum_{j=i}^{N} D_{ij}\{\frac{M}{M_j}(\nabla m_i + m_i\frac{\nabla M}{M})\}]$
Species conservation equation	$\nabla(\varepsilon u\, c_k) = \nabla(D_k^{eff}\nabla c_k) + S_k$
Charge conservation equation	$\nabla.(k_e^{eff}\nabla\Phi_e) + S_\Phi = 0$

Table 2. Source terms using equations and boundary conditions

Equations	Flow Channels	GDL	Catalyst Layer	Membrane
Momentum	$S_u=0$	$S_u=-\nabla P\frac{k_p}{\mu}$	$u=0$	$u=0$
Species	$S_k=0$	$S_k=0$	$S_k=-\nabla n_d F I_e - s_k j n F$	$S_k=-\nabla n_d F I_e$
Charge	$S_\Phi=0$	$S_\Phi=0$	$S_\Phi=j$	$S_\Phi=0$
Boundary Conditions				
$U_{in,anode}=U_{a,in}, U_{in,cathode}=U_{c,in}$				
$c_{H2,anode}=c_{H2,a}$; $c_{O2,cathode}=c_{O2,c}$; $c_{H2O,anode}=c_{H2O,a}$; $c_{H2O,cathode}=c_{H2O,c}$				

3. Results

3.1 Validation of the numerical model

The computational model solved for reference conditions and polarization curve validated with Ismail et al's (2012) experimental and computational resuts. As shown in Figure 2, model values and reference values fitted each other.

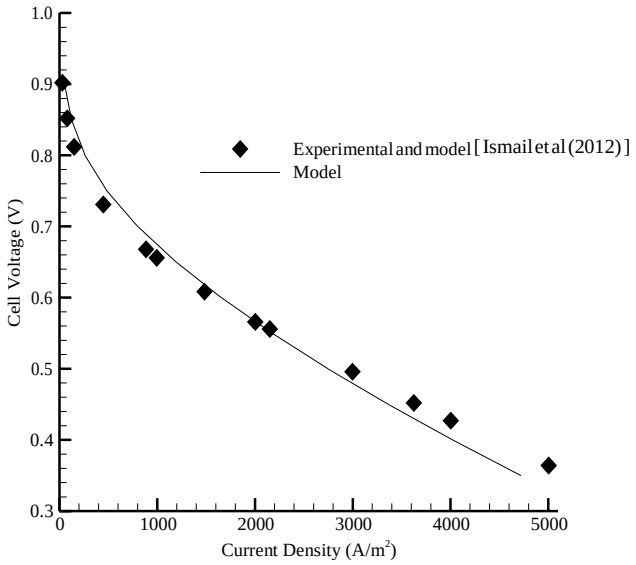

Figure 2. Validation of model with reference experimental and model values.

3.2 Results of case studies

For two different case groups (as shown in Table 3), the effects of anisotropic electrical conductivity on electrochemical phenomena in PEM fuel cell are analyzed separately. Figure 3 illustrates the interface that measuring of potentials and current densities values of fuel cell.

Table 3. Case Study Parameters

Case Group A		
Case Number	**In-plane conductivity [S/m]**	**Through-plane conductivity [S/m]**
1	100	400
2	200	400
3	400	400
Case Group B		
1	400	100
2	400	200
3	400	400

Polarization curves of the two different case groups are demonstrated in Figure 4. As it is seen in the figure, for the Case Group A, when the in-plane electrical conductivities of gas diffusion layers increase gradually, fuel cell performance decreases dramatically at constant through plane electrical conductivity. Furthermore, there is an increment in fuel cell performance by increasing through plane electrical conductivities of gas diffusion layers at constant in-plane electrical conductivity.

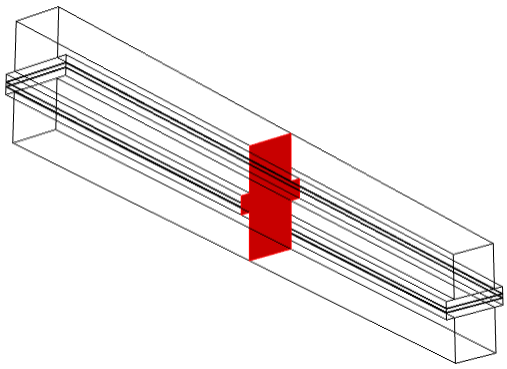

Figure 3. Interface that measuring potentials and current densities.

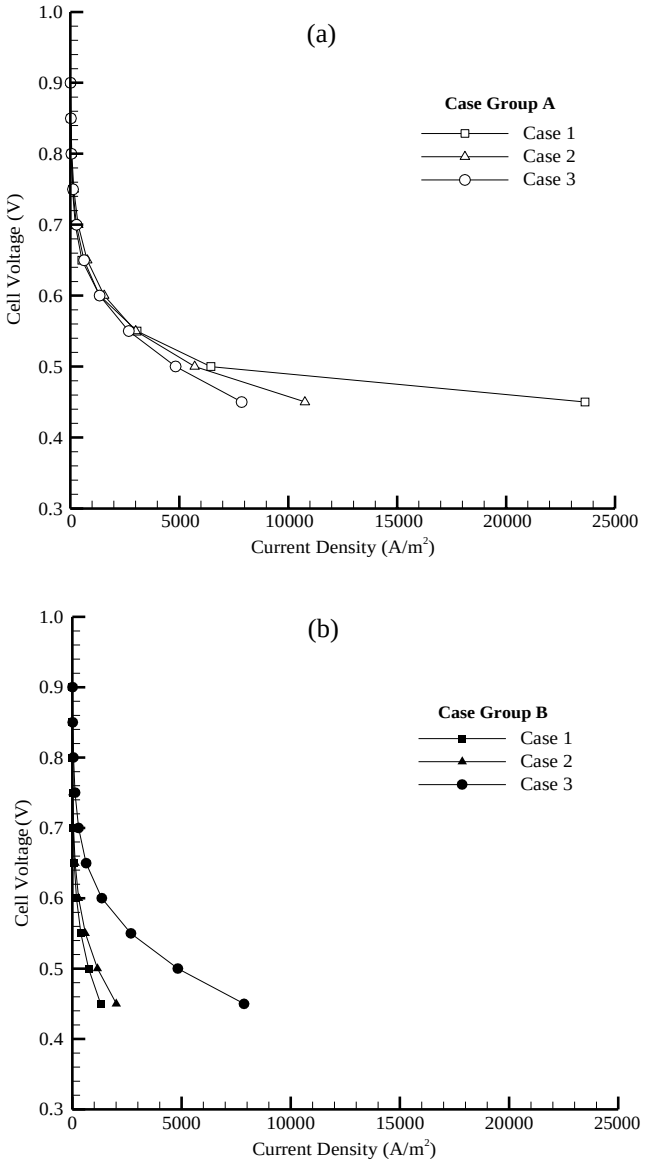

Figure 4. The variations of polarization curves for cases (a) Case Group A (b) Case Group B.

The variations of electrolyte potential depending on anisotropic electrical conductivities are shown in Figure 5. As the electrolyte potential increases by increasing through plane electrical conductivity at constant in-plane electrical conductivity, the increment of in-plane electrical conductivity leads to decreases in electrolyte potential. The reason of the increasing in the electrolyte potential is that charged particles go towards rapidly triple phase boundary in through plane.

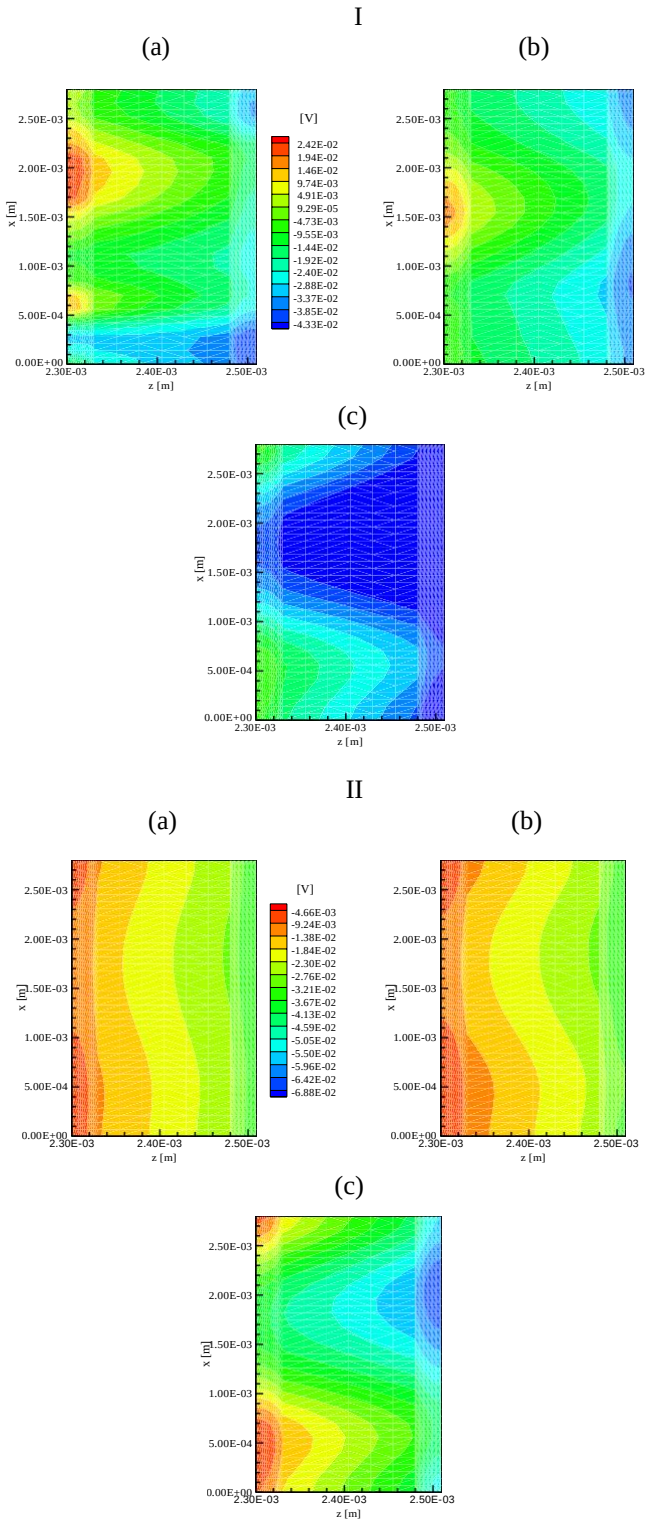

Figure 5. The variation of electrolyte potential depending on anisotropic electrical conductivities, Vcell=0.45 V [I. at in plane a) σIP = 100 S/m, b) σIP = 200 S/m, c)σIP = 400 S/m, constant σTP = 400 S/m II. a) σTP = 100 S/m, b) σTP = 200 S/m, c) σTP = 400 S/m, constant σIP = 400 S/m].

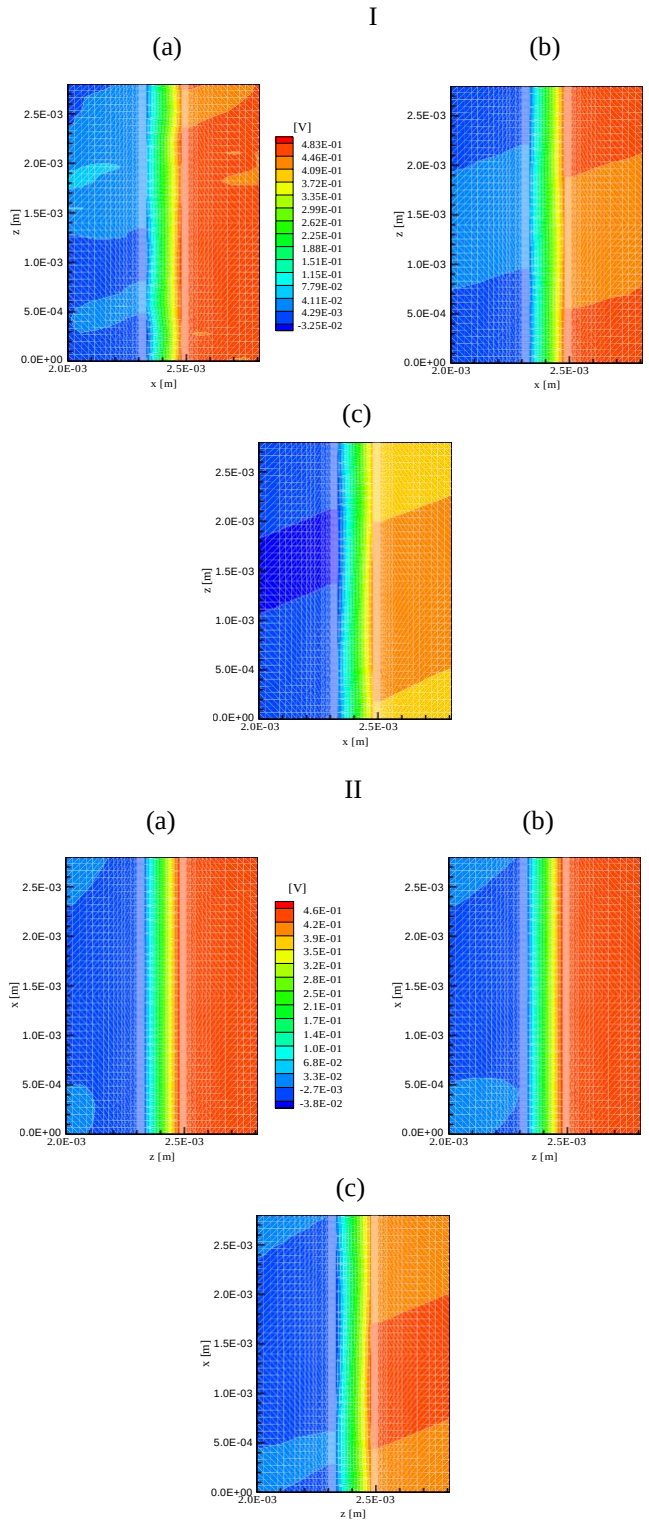

Figure 6. The variation of electrode potential depending on anisotropic electrical conductivities, Vcell=0.45 V [I. at in plane a) σIP = 100 S/m, b) σIP=200 S/m, c) σIP = 400 S/m, constant σTP = 400 S/m II. a) σTP = 100 S/m, b) σTP=200 S/m, c) σTP = 400 S/m, constant σIP = 400 S/m].

Figure 6 illustrates the variation of electrode potentials depending on anisotropic electrical conductivities. As shown this figure, when the electrode potential increases approximately from 0.03V to 0.46 V in the Case Group A, the electrode potential increases from 0.03V to 0.48 V in the Case Group B.

The variations of electrolyte current density depending on anisotropic electrical conductivities are indicated in Figure 7. It is shown that electrolyte current density has uniform distributions on membrane electrode assembly in Case Group B.

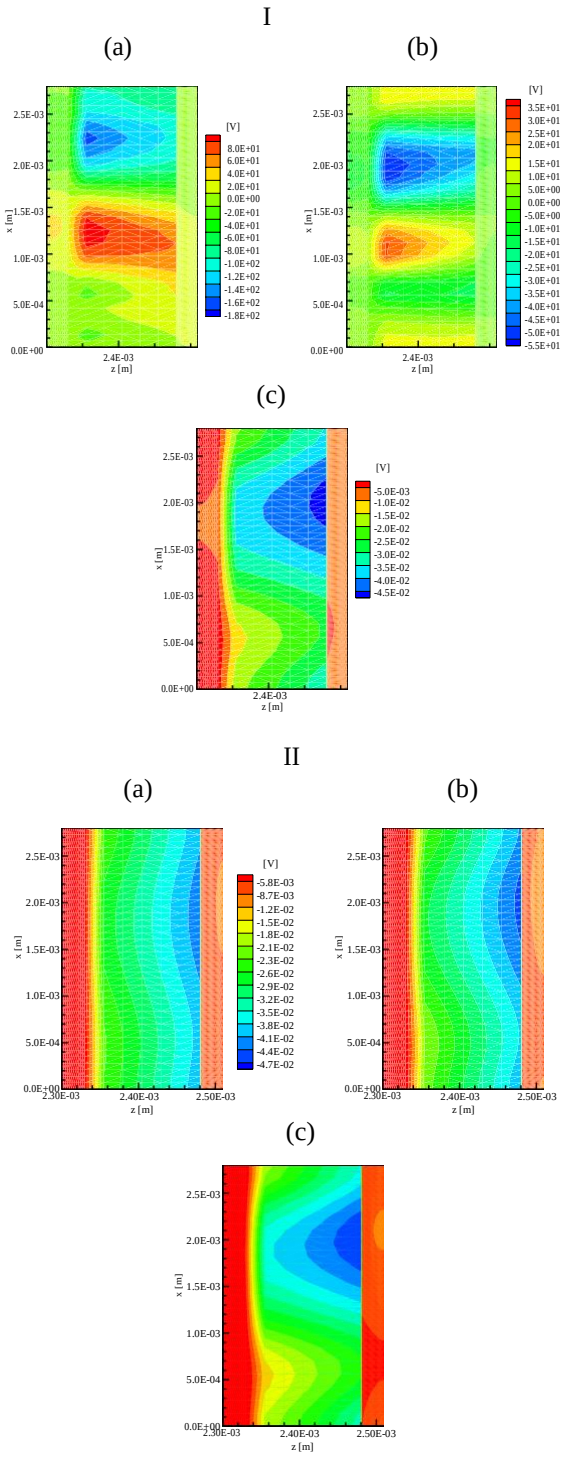

Figure 7. The variation of electrolyte current density depending on anisotropic electrical conductivities, Vcell=0.45 V [I. at in plane a) σIP = 100 S/m, b) σIP=200 S/m, c) σIP = 400 S/m, constant σTP = 400 S/m II. a) σTP = 100 S/m, b) σTP=200 S/m, c) σTP = 400 S/m, constant σIP = 400 S/m].

4. Conclusion

The effects of anisotropic electrical conductivity of gas diffusion layers on charge transport in PEM are investigated in this paper. Conclusions of the study are listed briefly as follows:

Through plane conductivity has more important influence impact on fuel cell performance and electrochemical phenomena than in-plane electrical conductivity.

The electrolyte current density on membrane electrode assembly is distributed uniformly by increasing through plane electrical conductivity at constant in-plane electrical conductivity. Thus, membrane electrode assembly can have better mechanic stability and durability.

Acknowledgements

The authors would like to thank the Scientific Research Projects Unit of Erciyes University for funding and supporting the project under the contract no: FYL-2017-7235.

References

Bernardi D.M., Verbrugge M.W. 1990. Mathematical model of a gas diffusion electrode bonded to a polymer electrolyte. AIChE Journal 37(8), 1151–1163.

Berning T., Djilali N. 2003. A 3D, multiphase, multicomponent model of the cathode and anode of a PEM Fuel Cell. Journal of The Electrochemical Society 150(12), A1589.

Um S., Wang C.Y. 2004. Three-dimensional analysis of transport and electrochemical reactions in polymer electrolyte fuel cells. Journal of Power Sources 125(1), 40–51.

Dutta S., Shimpalee S., Van Zee J.W. 2000. Three-dimensional numerical simulation of straight channel PEM fuel cells. Journal of Applied Electrochemistry 30, 135-146.

Berning T., Lu D. M., Djilali, N. 2002. Three-dimensional computational analysis of transport phenomena in a PEM fuel cell. Journal of Power Sources 106(1), 284–294.

Ramesh P., Duttagupta S.P, 2013. Effect of channel dimensions on micro PEM fuel cell performance using 3D modeling. International Journal of Renewable Energy Research 3(2). 353-358.

Gurau V., Liu H., Kakaç S. 1998. Two-Dimensional Model for Proton Exchange Membrane Fuel Cells. American Institute of Chemical Engineers Journal 44(11), 2410–22.

Um S., Wang C. Y., Chen C.S. 2000. Computational fluid dynamics modeling of proton exchange membrane fuel cells. Journal of the Electrochemical Society 147(12), 4485–4493.

Ju H., Wang C.Y. 2004. Experimental Validation of a PEM fuel cell model by current distribution data. Journal of the Electrochemical Society 151(11), A1954.

Iranzo A., Munoz M., Rosa F., Pino J. 2010. Numerical model for the performance prediction of a PEM fuel cell model results and experimental validation. International Journal of Hydrogen Energy 35(20), 11533–11550.

Haghayegh M., Eikani M. H., Rowshanzamir S. 2017. Modeling and simulation of a proton exchange membrane fuel cell using computational fluid dynamics. International Journal of Hydrogen Energy 42(34), 21944–21954.

Bapat C. J., Thynell S. T. 2008. Effect of anisotropic electrical resistivity of gas diffusion layers (GDLs) on current density and temperature distribution in a Polymer Electrolyte Membrane (PEM) fuel cell. Journal of Power Sources 185(1), 428–432.

Zhou T., Liu, H. 2006. Effects of the electrical resistances of the GDL in a PEM fuel cell. Journal of Power Sources 161(1), 444–453.

Ismail M.S., Hughes K.J., Ingham D.B., Ma L., Pourkashanian, M. 2012. Effects of anisotropic permeability and electrical conductivity of gas diffusion layers on the performance of proton exchange membrane fuel cells. Applied Energy 95, 50–63.

Avrupa Bilim ve Teknoloji Dergisi
Özel Sayı, S. 7-11, Aralık 2017

Konferans Bildirisi

www.ejosat.com ISSN:2148-2683

European Journal of Science and Technology
Special Issue, pp. 7-11, Aralık 2017

Conference Paper

An Application of Data Mining in Individual Pension Savings and Investment System

Zeynep CEYLAN[1,2*], Samet GÜRSEV[2], Serol BULKAN[2]

[1] Corresponding author: Ondokuz Mayıs University, Faculty of Engineering, Department of Industrial Engineering, Samsun, Turkey
[2] Marmara University, Faculty of Engineering, Department of Industrial Engineering, Istanbul, Turkey,

(First received 3 November 2016 and in final form 22 July 2017)

Abstract

Individual Pension System (IPS) is a personal future investment system that allows individuals to regularly save for their retirement. IPS is enacted by the law and supported by the government through state contribution. In Turkey, IPS entered into force on October 27, 2003 and it achieved an impressive progress over the last years. This improvement has caused increase in amount of raw data stored in databases. However, accumulated data are complicated and big to be processed and cannot be analyzed by classical methods. Data mining is becoming an essential tool to discover hidden and potentially useful knowledge from raw data. For this reason, application of data mining techniques on Individual Pension Savings and Investment system is necessary. In this study, one of the data mining techniques, decision tree classification, was used to determine customers' profile. SPSS Clementine 12.0 software was used to develop a classification model. Analyses were performed by various decision tree algorithms. Some customer information of a pension company operating in Turkey were extracted from system. The significant rules about customers were revealed by analysis. The results of analysis indicated that the CHAID algorithm showed the best prediction with an accuracy of 85.64% among C5.0, C&R Tree, QUEST.

Keywords: Data mining, customer profile, individual pension system

[*] Corresponding author : Ondokuz Mayıs University, Faculty of Engineering, Department of Industrial Engineering , Atakum, 55139, Samsun, Turkey, zeynep.dokumaci@omu.edu.tr, phone: +90 362 312 19 19 - 1098

1. Introduction

The individual (private) pension system (IPS) is a personal future investment system which was created to complement the existing public social security systems in Turkey, such as SSK, Bağ-Kur or Government Retirement Fund. The system's target is to contribute economic development by providing long term funds and thereby increasing employment. It helps to citizens to live a more comfortable life in their retirement and to maintain their living standards. The government pays a 25% portion as government contribution for each contribution amount paid by participants. Turkish Individual Pension System started on October 27, 2003 with the contribution of six pension companies. The demographic distribution indicates most part of participants is located in Istanbul. In addition, between 25-40 ages are the most effective part of pension users and majority of this population's education level is university or master degree.

In this study, IPS customers of a well-known company in Turkey were investigated. The study aims to classify IPS customers according to their demographic attributes. This allows company to identify the profitable or unprofitable customer's profiles in detail. Thus, the company could carefully evaluate a number of important criteria that affect the potential participation of customers to the system. For example, what kind of customers would likely use these services? How many new customers could be attracted to the system? How much contribution rate they attend? and etc.

2. Research Method

2.1 Data mining

Companies databases contain hidden information. Data mining (DM), also called knowledge discovery in databases, is used for discovering interesting and useful (previously unknown and valuable) information or patterns from large data in databases. It is widely used for decision making in business (insurance, banking, retail), science research (medicine, astronomy), and government security (detection of criminals and terrorists). It is also a powerful technique with great potential to help companies focus on important information about their customers. Therefore, it provides companies to determine the impact on sales, customer satisfaction, and corporate profits (Tan et al., 2006; Chen et al., 2006; Yin et al., 2011).

In business environments, determination of profitable costumers is a significant and competitive factor of an organization. Because identification of customers to meet their product or service provides benefits to remain in the current economic environment. Moreover, analyzing customer profile helps organizations to know customers' value and special features, to identify the most profitable ones and to increase high quality relations with them. This helps much deeper and more comprehensive understanding of costumers. However, its application on individual pension savings and investment system is rare in literature.

In this study, we aimed to fill the research gap. For this purpose, decision tree model, data mining approach was performed to discover relation between demographic attributes of customers (Apeh et al., 2014).

2.2 Decision tree

Decision tree (DT) is a data mining method that is often used for classification, prediction, interpretation, and data manipulation. Because of easy interpretation and comprehension, decision tree has the advantages for the decision makers. A decision tree is a decision support tool that includes a root node, branches, and leaf nodes. Each internal node represents a test on an attribute, each branch represents an outcome of the test, and each leaf node (or terminal node) represents a class label. The top most node in a tree is the root node. The decisions are made at each node and each records of data continues through the tree along a path until the record reaches a leaf or terminal node of the tree (Han et al., 2012; Lee et al., 2007).

Several statistical algorithms such as Classification and Regression Trees (C&RT), Chi-Squared Automatic Interaction Detection (CHAID), Quick, Unbiased, Efficient, Statistical Tree (QUEST), and C5.0 (upgraded version of C4.5) have been developed for building decision trees. They work differently in the following ways. For example, how many splits are allowed at each level of the tree, when the tree is built how those splits are chosen, and how the tree growth is limited to avoid from over-fitting (Linoff and Berry, 2011; Prasad and Madhavi, 2012). These algorithms can be separated in terms of different characteristics as shown on Table 1 (Chien and Chen, 2008).

3. Application

3.1 Data description

The real data was derived from a company database in Turkey. This dataset contains 171625 customer records with 7 attributes for the year of 2014. The decision tree models generated from the dataset using demographic variables of customers. Detailed information about attributes in the customer dataset is shown in Table 2. As seen from table, the dataset includes continuous and discrete attributes. In order to measure performance of the algorithms without any bias, continuous variables was converted into categorical variables.

Table 1. Comparison of CHAID, QUEST, C5.0, and CART

Algorithm	Data Type	Split Criteria	Number of branches at each node	Target variable	Input variable
CHAID	Discrete	Chi-square test	Two or more	Categorical	Categorical/ Continuous
QUEST	Discrete	Chi-square for categorical variables / J-way ANOVA for continuous/ordinal variables	Two	Categorical	Categorical/ Continuous
C5.0	Discrete/ Continuous	Gain Ratio Entropy info	Two or more	Categorical/ Continuous	Categorical/ Continuous
C&RT	Discrete/ Continuous	Gini index entropy	Two	Categorical/ Continuous	Categorical/ Continuous

Table 2. Details of customer data

Variable	Variable Type	Description
Contribution rate (Target)	Categorical	Monthly contribution rate (₺) 0-250, 251-500, 501-750, 751-1000, or 1000+
Payment Type (Input)	Categorical	Credit card, Remittance, or Salary
Gender (Input)	Binary	Male or Female
Marriage Status (Input)	Binary	Single or Married
Kids Status (Input)	Binary	Yes or No
Age (Input)	Continuous	Age of customers
Education Level (Input)	Categorical	High School level and below, Bachelor degree, or Master and above

3.2 Modeling

Clementine V12.0 software developed by SPSS was used to build predictive model in classifying the customer dataset above. SPSS Clementine includes a wide variety data mining techniques associated with data preparation, manipulation and visualizations tools. In the study, the decision tree models were worked using data set node, predictive model node and assessment node.

Several algorithms (QUEST, CHAID, C5.0, C&RT) in SPSS Clementine software were employed to build the decision trees, and then all models were evaluated by using target variable (contribution rate) and input variables (payment type, age, gender, marriage status, kids status, education level). The data stream can be found in Fig. 1.

4. Results and Discussion

For the analysis, the data is firstly divided into training data and testing data. The training set is used to build the classifier, while the test set is used to validate it. In this study the percentages used for training and testing data are 75% and 25%, respectively. The accuracy measure, which is used widely to compare the performance of classifiers, was obtained by using Eq. (1).

$$Accuracy\ (\%) = \frac{TP+TN}{TP+TN+FP+FN} \qquad (1)$$

(True Negative) is the number of true negative cases and *FN (True Positive)* is the number of false negative cases. The where *TP (True Positive)* is the number of true positive cases, *FP (True Positive)* is the number of false positive cases, *TN* performance of all models was recorded by using highest testing and validation predictive accuracy rate.

As shown on Fig. 2, the CHAID decision tree model is more accurate than other techniques. In overall performance, the CHAID model recorded an impressive of accuracy score of 85.64% compared of that to the other models: C5.0 (84.59%), C&RT (82.63%) and QUEST (64.35%), see Fig. 3.

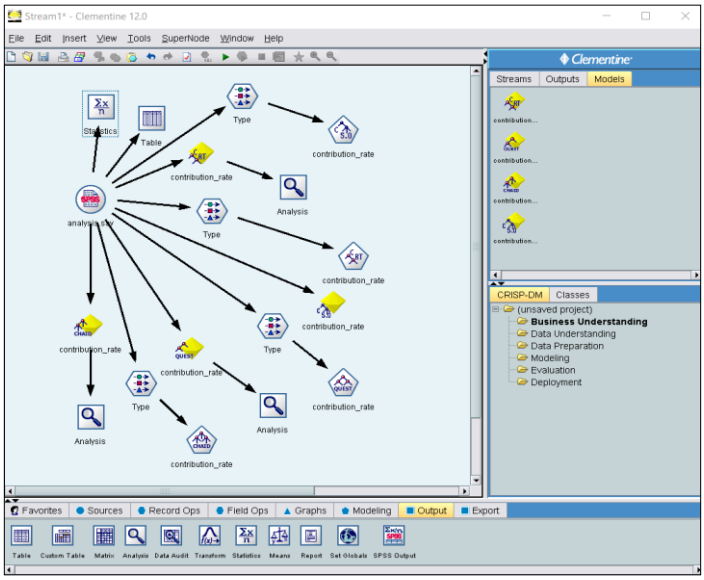

Figure 1. SPSS Clementine workspace with four decision tree models

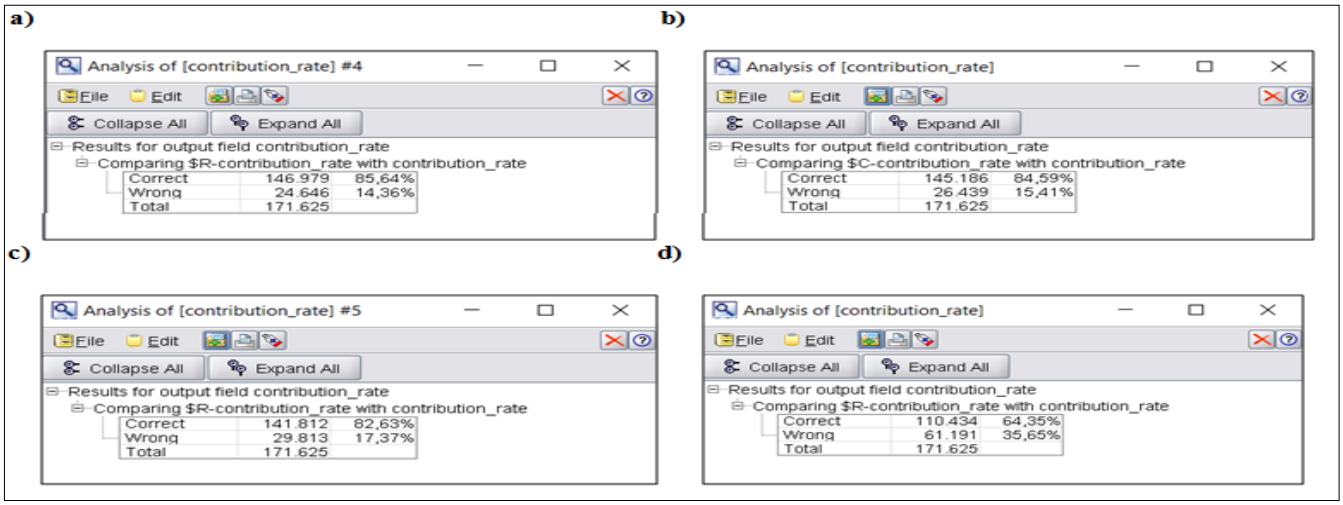

Figure 2. a) Model performance for CHAID algorithm b) Model performance for C5.0 algorithm c) Model performance for C&RT algorithm d) Model performance for QUEST algorithm

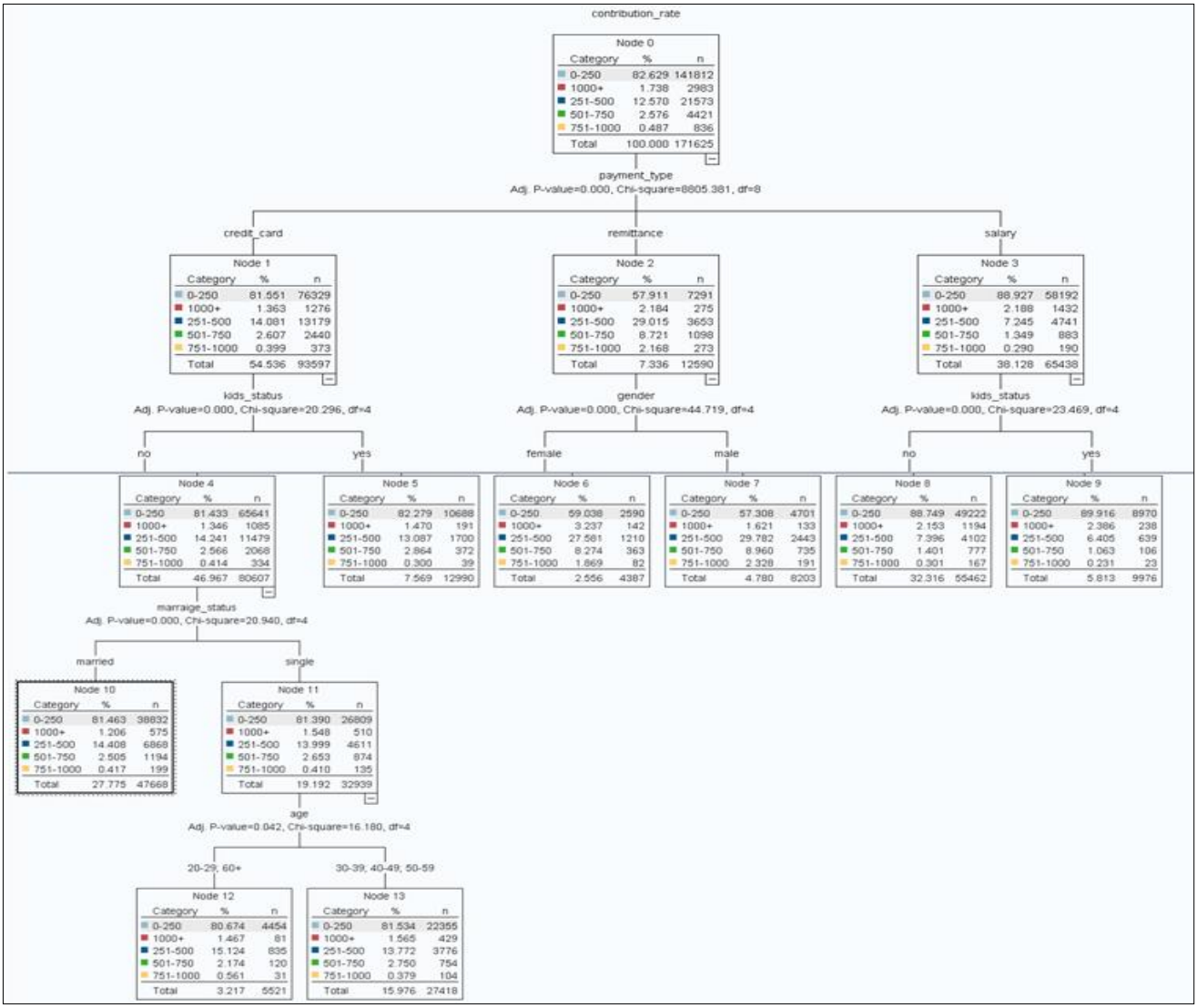

Figure 3. A sample part of CHAID classification tree

5. Conclusion

Determination of customers profile is very important for sales and marketing strategies for companies. For this reason, analyzing of customer behavior according to their features will be necessary. Data mining provides the companies to define and classify customers in detail to understand their behaviors. In addition, data mining provide strategic information for many customer-centric applications.

Data mining focuses on the practical importance of the information or knowledge gained from the models. The study results showed that the construction and evaluation of decision tree algorithms on individual pension system is important. This study will be a guiding start for Individual Pension Savings and Investment System. It might be beneficial for further studies for application of other data mining techniques. Using customer profiling through data mining might be the new competitive strength for the company owners in this sector

References

Apeh E., Gabrys B., Schierz A. 2014. Customer profile classification: To adapt classifiers or to Relabel customer profiles?, Neurocomputing 132, 3-13.

Chen Y.-L., Chen J.-M., Tung C.-W. 2006. Data Mining Approach for Retail Knowledge Discovery with Consideration of the Effect of Shelf-Space Adjacency on Sales. Decision Support Systems 42, 1503–1520.

Chien C.-F., Chen L.F. 2008. Data mining to improve personnel selection and enhance human capital: A case study in high-technology industry. Expert systems with applications 34, 280-290.

Han J., Kamber M., Pei J. 2012. Data Mining Concepts and Techniques. Morgan Kaufmann Publishers Inc., 3. Edition, Waltham, USA.

Lee S., Lee S., Park Y. 2007. A prediction model for success of services in e-commerce using decision tree: E-customer's attitude towards online service. Expert Systems with Applications 33, 572-581.

Linoff G.S., Berry M.J. 2011. Data mining techniques: For marketing, sales and customer relationship management. (3rd ed.) Indianapolis, Wiley Publishing Inc.

Prasad U.D., Madhavi S., 2012. Prediction of Churn Behavior Of Bank Customers Using Data Mining Tools. Business Intelligence Journal 5(1), 96.

Tan P.-N., Steinbach M., Kumar V. 2006. Introduction to Data Mining. International Edition, Pearson Education Inc., Boston, USA.

Yin Y., Kaku I., Tang J., Zhu J.M. 2011. Data Mining: Concepts, Methods and Applications in Management and Engineering Design.

Avrupa Bilim ve Teknoloji Dergisi
Özel Sayı, S.12-15, Aralık 2017

Konferans Bildirisi

www.ejosat.com ISSN:2148-2683

European Journal of Science and Technology
Special Issue, pp. 12-15, December 2017

Conference Paper

Standards and Testing Experiments for a Photovoltaic Module

Zuhal ER[11] , Zahir ROUABAH[2], Gokhan KIZILKAN[3], Alp Tolga ORKEN[3]

[1]Istanbul Technical University, Faculty of Science and Letters, Physics Engineering Department (13b), 34469 Maslak-Istanbul/TURKEY, erzuh@itu.edu.tr
[2] University of BordjBouArreridj, ALGERIA, zahir.rouabah@gmail.com
[3]Istanbul Technical University, Faculty of Science and Letters, Physics Engineering Department, 34469 Maslak-Istanbul/TURKEY, zuhaler@yahoo.com.tr

Abstract

This study examines the effect of irradiance and temperature on the performance of a PV panel. Additionally this study was focused on two main multi-disciplinary topics. Firstly, the standards and testing for solar modules with main focus being on TS EN 61215 related criteria which has regional nonconformities such as Standard Test Condition with respect to the 250C and testing is examined. This scrutinize will also give insight on selecting to examine this particular standard over many other standards related to solar modules with Natural Test Condition (NTC). Secondly, the knowledge of standards is applied to a real life experiment for a photovoltaic module. Voltage values, current values and temperature values were taken and graphs were singled out in this paper. Consequently, the panel which was deemed unfit to meet the standards was subjected to testing in this study. An average cell temperature higher than NOCT value is observed. Higher temperatures in solar modules decreases open circuit voltage, causing the panel to enter the breakdown region where current drops earlier. Thus, due to this aberration we were able to observe the breakdown region for the tested panel.

Keywords: Photovoltaic, Solar panel test, Solar panel standards, Solar panel efficiency, Solar panel performance, I-V graphs of PV panel

PACS– 07.05.Tp, 07.05.Bx, 07.05.Kf.

[1] Corresponding Author: Istanbul Technical University, Faculty of Science and Letters, Physics Engineering Department (13b), 34469 Maslak-Istanbul/TURKEY, erzuh@itu.edu.tr

1. INTRODUCTION

Energy consumption of the world is increasing rapidly over centuries due to the growth of technology [1,2,3]. However, even with all of its advantages, with enormous amount of manufacturers all around the globe, standards for PV panels must guarantee cost effectiveness for investors. Standards ensure the products are safe, reliable and of good quality. International standards also give confidence to the customers that the products will do the job they were intended for and they can buy and use a product manufactured anywhere, even in another country safely. They help to bridge the gap between research and marketable services or products. They are also proven to boost productivity and help economy [http1]. This study is set on the several main topics such as that the theory working principles of solar cells and also standards and testing for solar modules with main focus being on TS EN 61215 related criteria and testing. Therefore, the evaluations will also give insight on selecting to examine this particular standard over many other standards related to solar modules. In this respect, the knowledge has been applied to a real life experiment. The experimental study shows what kind of conditions affect the efficiency of a PV panel. Evaluation of the results of the PV panel efficiency in the system. Thereby, these experimental studies has made withtogether the focusing on standards and testing of photovoltaic modules.

1.1. TESTING AND STANDARDS FOR PV PANEL

New electrical standards projects are jointly planned between European Committee for Electrotechnical Standardization(CENELEC) and International Electrotechnical Commission (IEC), and where possible most are carried out at international level. After 20 years of partnership CENELEC and IEC have reconfirmed their longstanding cooperation on 17 October 2016, by signing the Frankfurt Agreement [http2].

These agreements allowed mutual code numbers for standards. IEC standards are also found preceded by EN to indicate that the IEC standard is also adopted by CENELEC as a European standard (e.g. IEC 61215 is also available as EN 61215).

Also worth mentioning; International Organization for Standardization (ISO) is a sister organization to IEC and the European Committee for Standardization (CEN) is a sister organization to CENELEC. CEN and CENELEC are the regional mirror bodies to their international counterparts, IEC and ISO[http3]. National standards for Turkey about PV modules are prepared by Turkish Standards Institution (TSE) and they are a projection of both global standard of ISO and European standards (EN). TSE become a full member of ISO and IEC by 1956, and a full member of CEN and CENELEC by 2012 [http4, http5, http6, http7, http8]. The main standards related to PV modules by TSE are;

•TS EN 61215: Terrestrial photovoltaic (PV) modules - Design qualification and type approval

•TS EN 61646: Thin-film terrestrial photovoltaic (PV) modules – Design qualification and type approval

•TS EN 61730-1: Photovoltaic (PV) module safety qualification- Requirements for construction

•TS EN 61730-2: Photovoltaic (PV) module safety qualification- Requirements for testing

•TS EN 61345: UV test of photovoltaic (PV) modules

• TS EN 62716: Photovoltaic (PV) modules Ammonia corrosion testing

•TS EN 61701: Salt mist corrosion testing of photovoltaic (PV) modules

For a PV module to be approved (branded) by TSE, it should pass all the related standard testing.This study is focused on TS EN 61215 as it is the main standard for crystalline photovoltaic modules, which is most commonly used. Therefore, in this study, the experimental setup consisted of the solar module which is made by Siemens with product type of SP75 as shown in the Figure 1.

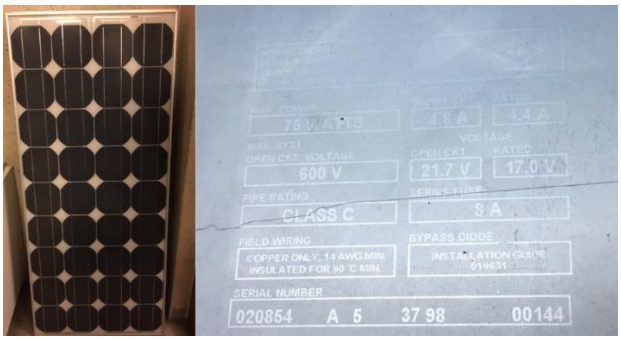

Figure 1. Solar module used in the experiments and technical parameters from the documentation of the panel on the name plate (These values are tested in Standard Test Conditions (STC), which is; 1000W/m² Irradiance, 25 ºC Cell Temperature and Air Mass: 1.5).

Certifications and qualifications of the panel are;

• IEC 61215 • UL-Listing 1703 • TÜV safety class II

• JPL Specification No. 5101-161 • CE mark • FM Certification

The technical data of the panel is as Max Power is 75 Watts, Open Circuit Voltage is 21.7 V

Fire Rating is Class C, and For Current; Short Circuit is 4.8 A, Rated: 4.4 A, For Voltage; Open Circuit is 21.7 V , Rated is 17.0 V and also NOCT (Nominal Operating Cell Temperature) 45±2 ºC . The experiments in this study was conducted in Göztepe/ Istanbul-Turkey that the coordinates are 40º 58' 47.06'N and 29º 3' 36.35'' E as shown in the Figure2.

Figure2. Location of the experiment via the computer calculation program that is combined by the Google Maps JavaScript API

2. RESULTS AND DISCUSSION

The real life experiments support the understanding on what kind of conditions affect the efficiency of a photovoltaic module. Voltage, current and temperature values were taken and graphs were singled out in this paper to understand the efficiency of module as shown in the Figure 3 and Table 1.

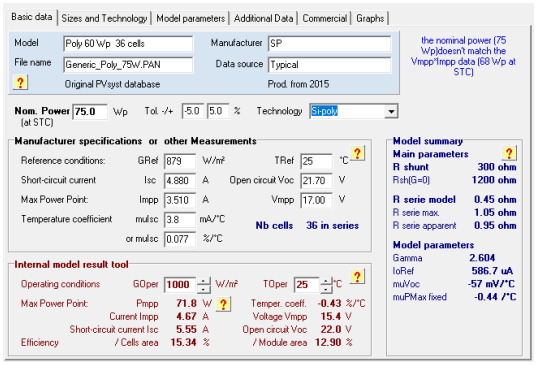

Figure 3. Definition of PV module parameters via computer program

The results are also checked with respect to the TS EN 61215 [4,5]. The standard explains the requirements ofname plate, documentation accompanying to the module and pass criteria thoroughly.As it can be observed in *Figure 1,* the name plate is not complexly readable. As an example according to TS EN 61215-1 section 5.1 each module should include clear and indelible markings of (section 5.1, clause a) “name, registered trade name or registered trade mark of the manufacturer” [4]. Thus, if this module was a test sample for TS EN 61215-1in the state it is in when the experiment was conducted, this flaw alone would cause this module to be deemed not to have met the qualification requirements.

Table 1. The open circuit values of the experiment in 1st of June

Time	Degree	Temperature	V_oc (V)	I_sc (A)	P_sc (W)	T_1sc (°C)	T_2sc (°C)	T_3sc (°C)	T_4sc (°C)	T_sc_abs (°C)
14:34	0°	24°C	18,56	3,86	71,6416	65,9	68,4	68,5	67	67,45
14:42	10°	24°C	18,7	4,02	75,174	60,8	63,8	65,6	65,3	63,875
14:51	20°	24°C	18,9	3,91	73,899	59,1	61,1	61,3	61,7	60,8
15:02	30°	24°C	18,9	3,75	70,875	56,1	56,8	57,1	55,1	56,275
15:11	40°	23°C	18,92	3,38	63,9496	52,9	51,6	53,1	52,8	52,6
15:19	50°	23°C	18,95	3,17	60,0715	52,6	56,5	56,4	52,9	54,6
15:30	60°	23°C	18,95	2,85	54,0075	53,9	54,1	52,9	53	53,475
15:38	70°	23°C	18,92	2,41	45,5972	51,6	53,3	55,2	52,1	53,05

Testing was conducted in different times of the day for multiple days; both for open circuit system and closed circuit system. Experimental results for 1st June 2017 are given by the Table 1 and their evaluations are illustrated by the Figure 4 and Figure 6.

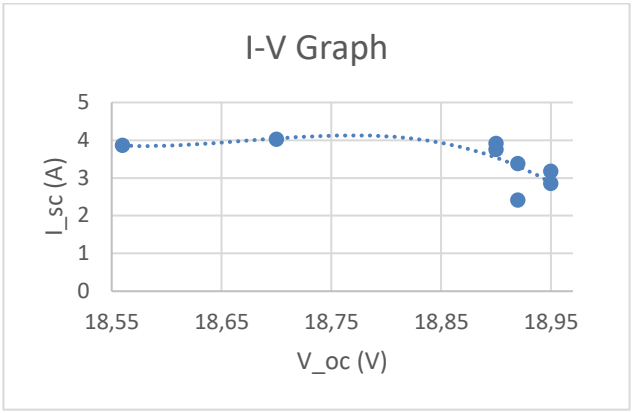

Figure4. The I-V graph of the experiment in 1st of June in the open circuit arrangement

The computed results are also analyzed and compared with the graph of datasheet calculated. These computer evaluations are illustrated on the Figure 5 and Figure 7. Solar radiation power per unit area on the horizontal surface is calculated using by average values of the results in this study. This calculation is given by the Equation 1.

$$E_{inc} = \frac{1000\frac{W}{m^2} * I_{sc(avg)}}{I_{sc(stc)}} = 712{,}240\,\frac{W}{m^2} \quad (1)$$

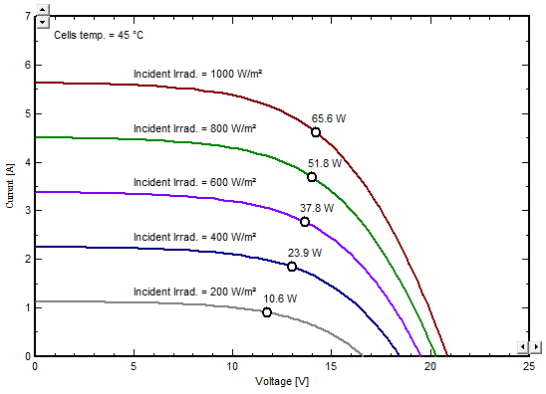

Figure 5. Module behavior according to the incident irradiation (W/m2)

The Figure 5 represents the current-voltage evaluation with respect to incident radiance which is solar power per unit area. The green line in the Figure 5 is compatible with our calculation.

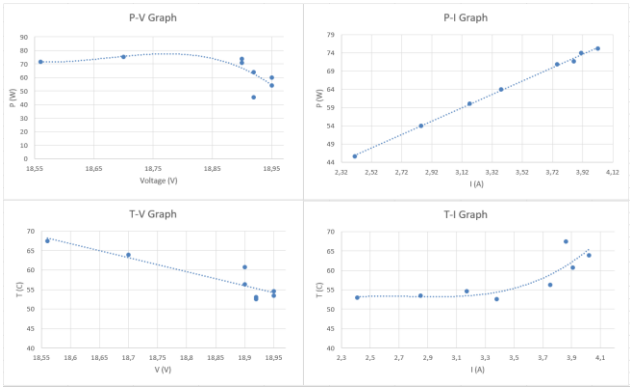

Figure 6. Other graphics for the open circuit arrangement for 1st of June

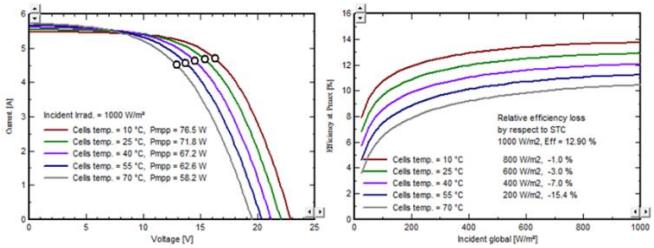

Figure7.Temperature dependency of I-V characteristics (left-hand side) and efficiency (right-hand side) of the module

The performance of the panel was unsatisfactory. Cell temperatures were ranging between 47,33ºC to 67,45ºC, indicating the module was not working properly, as the NOCT of the module is 45ºC. This value is valid under 1000 W/m^2 and wind speed of maximum 1 m/s.

$$T_{leftstring(avg)} = 56{,}525\ ℃$$

$$T_{rightstring(avg)} = 57{,}225\ ℃$$

Moreover, because the panel is time-worn, there is a defect in a cell as it can be observed in *Figure 8*..As it is dictated in TS EN 61215section 8, clause h; if there are voids or corrosion in any cell, defective area should not exceed 10% of that cells total area. Which in this case it does. Thus this also would cause this module to fail to meet qualification requirements.

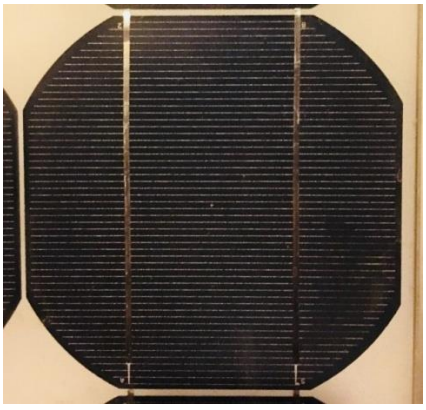

Figure 8. Defective Cell

3. CONCLUSIONS

A degraded panel which was deemed unfit to meet the standards (by visual inspection) was subjected to testing in this study. During the experiment the irradiance was lower and wind speed was higher. Thus an average cell temperature lower then NOCT value should be possible.

Nevertheless, the damaged cell was the reason behind elevated cell temperatures. The main reason for the defect was the EVA (ethylene vinyl acetate), that is a layer which lies under the upper part of the cell. EVA layer helps the cell to resist impacts but if there is a problem with this layer; it is easier for the cell to be oxidized. The damaged part of the cell cannot produce electricity thus it acts as a load, increasing the temperature of itself and the string of the cells it is in; which decreases the performance. Higher temperatures in solar modules decreases open circuit voltage, causing the panel to enter the breakdown region earlier, which results in an earlier current drop. Thus, due to this aberration we were able to observe the breakdown region without a solar simulator as the panel should be designed to not to enter this region under normal outdoor conditions.

Ultimately, the visual inspection, as it was imposed by the standards predicted an unsatisfactory outcome. All of the experimentation done subsequently approves validity of TS EN 61215.

REFERENCES

[1] Z.Er, and I.B.Turna. Future Expectation of The PVs Role in Compensating Energy Demand, Acta Physica Polonica Series A. April 2016. DOI: 10.12693/APhysPolA.129.865

[2] Z.Er, "Utilization of the Collector Rainbow System in Istanbul", Acta Physica Polonica A, Vol. 128, No 2B, (August 2015), page B300-302

[3] Z.Er, "A Study of Importance of Solar Calculations for Two Colored Rainbow System in Istanbul", Acta Physica Polonica A, Vol. 128, No 2B, (August 2015), page B477-B478

[4] TS EN 61215-1:2017-03

[5] TS EN 61215:2006-01

[http1] https://cebr.com/reports/standards-contribute-8-2-billion-to-uk-economy/ (Access date: 08.06.2017)

[http2] https://www.cenelec.eu/aboutcenelec/whoweare/globalpartners/iec.html (Access date: 08.06.2017)

[http3]https://www.cenelec.eu/aboutcenelec/whoweare/europeanstandardsorganizations/index.html (Access date: 08.06.2017)

[http4] https://www.tse.org.tr/tr/icerikdetay/149/3484/usm.aspx (Access date: 08.06.2017)

[http5] http://www.iec.ch/dyn/www/f?p=103:5:0 (Access date: 08.06.2017)

[http6] https://www.iso.org/members.html (Access date: 08.06.2017)

[http7] https://standards.cen.eu/dyn/www/f?p=CENWEB:5 (Access date: 08.06.2017)

[http8] https://www.cenelec.eu/dyn/www/f?p=WEB:5 (Access date: 08.06.2017)

Avrupa Bilim ve Teknoloji Dergisi
Özel Sayı, S. 16-21, Aralık 2017

Konferans Bildirisi

www.ejosat.com ISSN:2148-2683

European Journal of Science and Technology
Special Issue, pp. 16-21, December 2017

Conference Paper

Experimental Investigation on Fatigue Life of Cord-Rubber Composites

Onur Aykut Kapucu[1], Hasan Kasım[2], Yücel Can[3], Murat Yazıcı[4*]

[1] Uludağ University, Engineering Faculty, Automotive Engineering Department, Bursa, Turkey, onayka89@gmail.com
[2] Uludağ University, Engineering Faculty, Automotive Engineering Department, Bursa, Turkey, hskasim@gmail.com
[3]R&D Center Renault Automotive Company, Bursa, Turkey, yucel.can@renault.com
[4]Uludağ University, Engineering Faculty, Automotive Engineering Department, Bursa, Turkey, myazici@uludag.edu.tr

Abstract

Air springs are used in automobile suspensions and perform under highly dynamic loading conditions. An essential component of an air spring mechanism is the rubber tube. The rubber tube produced from layered cord rubber composites. It is constructed as two-layer cord fabric reinforced rubber composites. The matrix crack, debonding and failure of the cord are the most observed damage modes of cord-rubber composites. The presented study investigated fatigue life behavior and damage mechanisms of the PA 6.6 Cord fabric/Natural rubber composites. Curing conditions of rubber such as pressure (7.5,12.5, 15 MPa), temperature (140,160 and 180 °C) and time (5,8 and 10 min) were taken as research parameters. Moreover, two type of PA 6.6 cord fiber and three different fiber orientation angle (40,42 and 45°) were studied as material parameters. All experiments performed by using De-Mattia cyclic fatigue test equipment under 5 Hz frequency. The experimental study designed by Taguchi method using L18 orthogonal series. The results show that 12.5 to 15 MPa curing pressure, 8-10 min curing time and 160 °C are optimum values for cord rubber layered composites to obtain high fatigue life. The fiber type of the cord fabric and fiber orientation angle between 40 to 45° does not affect the fatigue life of the cord-rubber composites. The post-mortem analysis performed to clarify damage mechanisms.

Keywords: Cord rubber composites, fatigue, natural rubber, damage.

[*] Corresponding author, Uludağ University, Eng. Faculty, Automotive Eng. Department, Bursa, Turkey, myazici@uludag.edu.tr, 90(224)2942630

1. Introduction

Rubber is a kind of valuable polymer material, which has the unique properties of other materials. Rubber material can withstand enormous strain but does not produce permanent deformation or damage and has the advantage that conventional engineering materials cannot match, which makes it has excellent application in many occasions (Zhang and Zhao 2015). Although these impressive properties of the rubber, their strength does not enough to self-use in many possible areas such as air springs, tires, and belts. To improve the strength properties of the rubber, different type of cord fiber reinforcements have been used, and cord/rubber composites developed. Several types of the cords have been used in tires as reinforcement, such as rayon, nylon 6 and 66, and polyester (Jamshidi et al. 2006). Fatigue life of the composite initially based on elastomeric matrix material and rubber/cord fiber interface. Both properties depend on vulcanization pressure, temperature, time process parameters and cord fiber twisting type and cord fiber surface preparations (Li et al. 2017). Although, cord fabrics improving the strength of rubber, the fatigue life of the rubber can be decreased by initiation of the cracks in the cord fiber/rubber interface and fiber end-tips (Valantin et al. 2015) In case of many parameters effects of the composite material's strength and fatigue life (Ozsoy et al 2016, Eksi and Genel 2017). Taguchi experimental design method is widely used to save experimental time and analyze effects of each parameter (Ozsoy et al. 2017).

In this study, fatigue life of the cord/rubber composites were studied under different process parameters. The research parameters of the cord/rubber composites were specified within the air-spring production parameters which all in the accepted tolerances by the air spring manufacturers. These were vulcanization time, vulcanization pressure and temperature, fabric orientation angle and cord fiber twist type. Taguchi experimental design was used to describe the experimental program.

2. Materials and Method

2.1 Materials

Natural rubber based composite matrix and cord fiber-based fabric were used in the manufacturing of rubber/cord composite specimens. Natural rubber based compound calendered as lining material. PEGA automotive Company supplies all the materials used in the experiments. Rubber coated cord fabric and lining rubber were used to form the reinforcing structure. The rubber coated cord consists of special rubber mixture and cord fabric. Lining rubber is prepared by calendering according to air spring standards. The thickness is 1.4 mm ± 0.05 and elongation at break % 450, and the strength is 21 MPA. The production line can be seen in Figure 1.

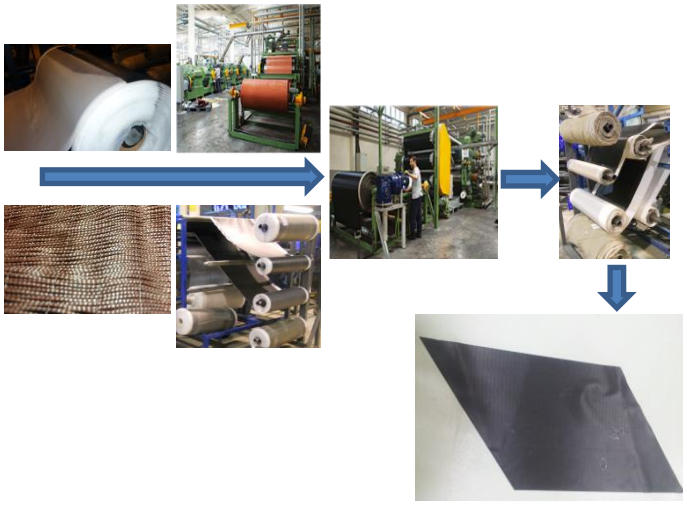

Exp No:	Cord Fabric Type	Fiber Orien. Angle (°)	Vulc. Time (min.)	Vulc. Temperature °C)	Vulc. Pressure (Bar)
1	1	40	5	140	125
2	1	40	8	160	150
3	1	40	10	180	75
4	1	42	5	140	150
5	1	42	8	160	75
6	1	42	10	180	125
7	1	45	5	160	125
8	1	45	8	180	150
9	1	45	10	140	75
10	2	40	5	180	75
11	2	40	8	140	125
12	2	40	10	160	150
13	2	42	5	160	75
14	2	42	8	180	125
15	2	42	10	140	150
16	2	45	5	180	150
17	2	45	8	140	75
17	2	45	10	160	125

Figure 1. Rubber/Cord fabric composite materials production line.

Two types cord fabrics were used based on Nylon 6.6. The fabrics were produced by Kordsa Co./Turkey. The fabrics were used in the production of the Air springs as reinforcement materials. They have the superior tensile strength and offering for weight reduction, longer life, easy processability, improved safety and higher load capacity. They called in this paper as Type1 (1400x2-120 Number of total fiber 1740) and type2 (940x2-150 dtex, Number of total fiber 2030). The mechanical and physical properties of these fabrics were presented in Table 1

2.2 Design of Experiments

To achieve the fatigue determination of the natural rubber/cord fabric composite structure, the most effective parameters were selected. Because of long experimental time need for fatigue experiments, decided to use Taguchi DOE technique. Temperature, Vulcanization Time, Cord Fabric Type, Cord Reinforcing Angle and Vulcanization Pressure were selected as

significant parameters to understand the effect of air-spring manufacturing tolerances. The parameters and their levels were given in Table 2. Using Taguchi Design of Experiment technique, L18 orthogonal series were applied. The Minitab ® software was used to a selection of efficient experiments. In Table 3, Taguchi DOE calculation results for the experimental program.

Table 1. Mechanical and physical properties of the cord fabrics.

Table 2. Decided parameters and levels in the study

Parameters	Levels
Vulcanization Temperature (ºC)	140, 160 and 180
Vulcanization Time (min.)	5,8 and 10
Cord Fabric Type	Type1 and Type 2
Cord Fabric Orientation Angle (°)	40, 42 and 45
Pressure (Bar)	75, 125 and 150

Table 3. Taguchi experimental design.

2.3 Material Production and Specimen Preparation

Specimens were prepared according to the calculated experimental program. The rubbers were prepared by cutting to the desired size. Cord fabrics were cut at different angles determined by their type. After the material preparation processes, all production activities were performed in the laboratory environment. In Figure 2 cutting rubber coated cord fabrics respecting orientation angle of composite specimens were presented.

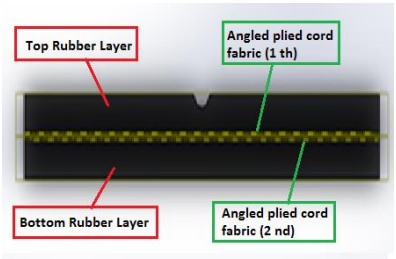

Figure 2. Cutting rubber coated cord fabrics according to orientation angle and placement of cord fabric between lining rubber material in the fatigue specimen.

Rubber coated fabrics were cut respecting described reinforcing orientation angles (40◦, 42◦ and 45◦) and standard Specimen size (25x 150 mm), lining rubber also cut specimen size and they set in the compression mold as decided layer configurations. Layer configurations and production flow were represented in Figure 3. Layered sheets were compressed and vulcanized under described process parameters such as pressure, time and temperatures.

Cord Yarn Properties	Type 1	Type 2
Yarn Count (dtex)	1400	940
Breaking Strength (Kg)	13.46	8.82
Tenacity (cN/tex)	93.3	91.7
Elongation (at 4.5 kg) %	8.1	9.2
Elongation at break (%)	18.2	17.5
Shrinkage (at 177ºC, 2 min.) (%)	6.6	7.4
Cord Fabric Properties		
Construction	1400x1x2	940x1x2
Breaking Strength Average (Kgf)	22.5	14.5
M adhesion (kg/10 mm)	15	10
Cord Thickness (mm)	0.65±0.05	0.54±0.04
Ply Twist, Z (tpm)	390±15	470±15
Cable Twist, S (tpm)	390±15	470±15

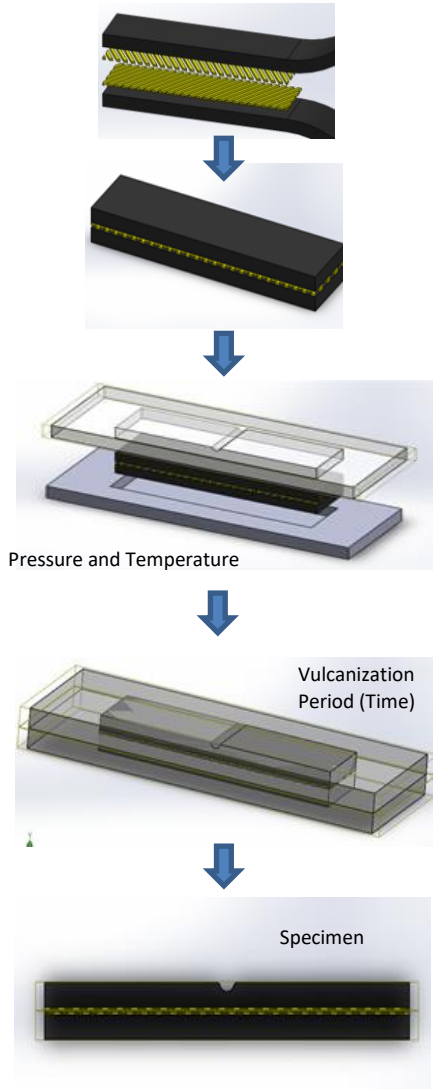

Figure 3. Specimen preparation flow schema.

The test specimens was obtained by vulcanizing prepared layered cord/rubber composites using a hot press at different temperatures, minutes and pressures. After the vulcanization process, rubber parts were taken out from the mold and rested for 16 hours at room temperature. Samples prepared according to De Mattia test device and ASTM D430-06 standard. Specimen dimensions and production mold and press were presented in Figure 4.

Figure 4. a) De-Mattia Specimen dimensions (ASTM D430-06) b) Mold c) Hot Press

2.4 Experimental Setup

The De Mattia fatigue test device is used at 5 Hz to initiate the formation of cracks by repeated flexing of cord/rubber composite specimens, prepared according to standards. The cord/rubber composite samples are clamped in the jaws of the De Mattia fatigue device as shown in Figure 5. The upper and lower jaws are fixed, and the middle part is movable. The middle part moves up and down to detect the crack initiation in the rubber. At the same time, 22 specimens can be loaded in the fatigue device. Each specimen was labeled from 1 to 18 and fatigue device was stopped each 50 000 cycle and specimens condition and crack initiation were observed and recorded.

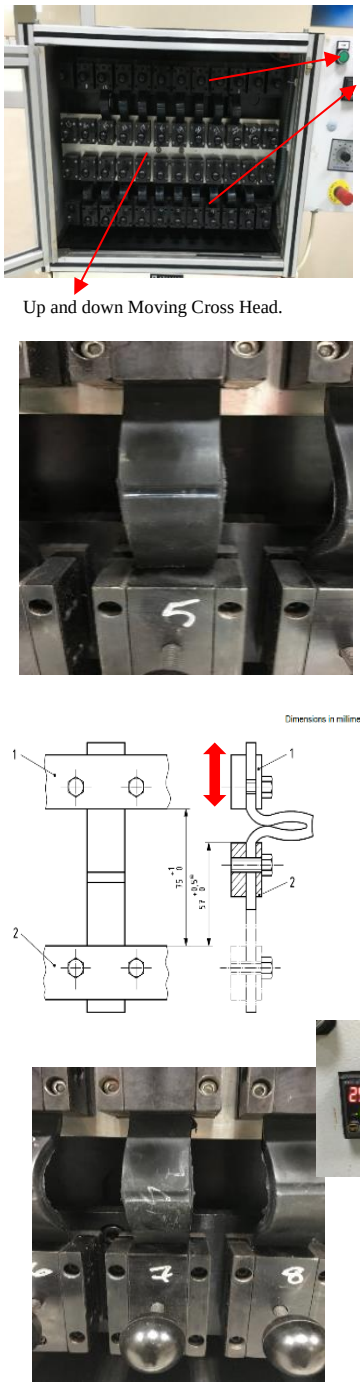

Figure 5. De Mattia fatigue test device and placement of specimens.

3. Results and Discussion

The fatigue life table of our samples results was obtained as given in Table 4. According to Taguchi analysis (Figure 7), Cord fabric type (Number 2) is more efficient than other parameters. It was observed that the temperature would be insufficient less than 160 ºC. Curing time as 8 min. is effective value for the fatigue life. Cord fiber orientation angles did not affect directly for selected orientation angles.

Table 4. Fatigue life results

Specimen Number	Cord Fiber Type	Fiber Orientation Angle (°)	Vulc. Time (min.)	Vulc. Temperature (ºC)	Vulc. Press. (Bar)	Fatigue Life Cycle
1	1	40	5	140	125	250000
4	1	42	5	140	150	260000
9	1	45	10	140	75	262250

The other 15 specimens were not shown any damage, fail or crack initiation up to infinite life (1x107). An example of the damaged specimen surfaces was given in Figure 6.

Figure 6. Damaged surfaces and crack initiation and propagation in a failed sample.

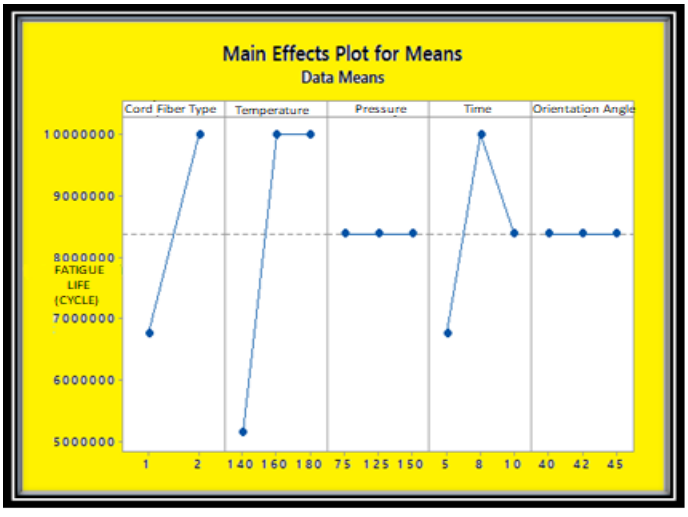

Figure 7. Taguchi analysis of parameters effect on fatigue life.

According to Taguchi analysis (Figure 7), Cord fabric type (Number 2) is more efficient than other parameters. It was observed that the temperature would be insufficient less than 160 ºC. Curing time as 8 min. is effective value for the fatigue life.

Cord fiber orientation angles did not affect directly for selected orientation angles.

4. Conclusions

In the presented study, fatigue life of the cord/rubber layered composites were investigated according to selected design and process parameters by experimentally, and the results can be concluded as given below:

- Cord fabric type is more efficient than other parameters.
- Under 140 °C temperature usage is not suitable for vulcanization.
- Vulcanization time as 8 min. is an optimum value for the fatigue life.
- Cord fiber orientation angles do not effect if they are around 45°.
- The cracks initiated in part, towards the inner edges due to bending because the surface of the material is not a flat surface relative to the outer surface.
- Inner side friction and contact between the two surface of is increased the surface temperature and increased the stress accumulation against to the notch tip.

References

Zhang X., Zhao G. 2015. Overview of Experimental Studies on Strength Problem of Rubber Material. 5th International Conference on Advanced Engineering Materials and Technology (AEMT 2015), 22-23 August, Guangzhou-China.

Jamshidi M., Afshar F., Shamayeli B. 2006. Evaluation of Cord/Rubber Adhesion by a New Fatigue Test Method. Journal of Applied Polymer Science 101, 2488–2494

Li X., Wei Y., Feng Q. and Luo R.K. 2017. Mechanical Behavior of Nylon 66 Tire Cord under Monotonic and Cyclic Extension: Experiments and Constitutive Modeling. Fibers and Polymers 18, 542-548.

Valantin C., Lacroix F., Deffarges M.P., Morcel J., Hocine N.A. 2015. Interfacial Damage on Fatigue-Loaded Textile–Rubber Composites. Journal of Applied Polymer Science. 132(4), 41346.

Ozsoy N., Ozsoy M., Mimaroglu A. 2016. Mechanical Properties of Chopped Carbon Fiber Reinforced Epoxy Composites, Acta Physica Polonica A 130, 297-299.

Eksi S. and Genel K. 2017. Comparison of Mechanical Properties of Unidirectional and Woven Carbon, Glass and Aramid Fiber Reinforced Epoxy Composites, Acta Physica Polonica A 132, 879-882.

Ozsoy N., Ozsoy M. and Mimaroglu A. Taguchi Approach to Tribological Behaviour of Chopped Carbon Fiber-Reinforced Epoxy Composite Materials. Acta Physica Polonica A 132, 846-848.

Avrupa Bilim ve Teknoloji Dergisi
Özel Sayı, S. 22-25, Aralık 2017

Konferans Bildirisi

www.ejosat.com ISSN:2148-2683

European Journal of Science and Technology
Special Issue, pp. 22-25, December 2017

Conference Paper

Study on Factors Affecting CO_2 Recovery of Fractured Pressure-sensitive Reservoirs

Yueli Feng[1], Yuetian Liu[1*], Jie Dong[1], Jian Chen[1], Jianshu Huang[1]

[1] State key Laboratory of Petroleum Resources and Engineering, China University of Petroleum, Beijing 102249, China, 68337999@qq.com

Abstract

The different deformation degree of fractures caused by the intrinsic strong pressure-sensitive property of the ultra-low permeability reservoirs would change the channeling law of CO_2 in fractures, then affect the oil displacement efficiency. Thus, revealing the seepage characteristics of CO2 in fractured reservoirs is the groundwork to improve the oil displacement efficiency of CO_2. The directional pressure-sensitive property of fractures was simulated by a physical model. The simulation of physical experiment with multi-physics coupling was carried out by theoretical derivation and finite element analysis software COMSOL Multiphysics. The stronger heterogeneity of reservoirs , makes CO_2 much easier to rush. Increasing injection pressure , can increase the proportion of CO_2 in low permeability area. As the pressure-sensitive property between high and low permeability layer is different, increasing the effective stress would induce stronger heterogeneity. Therefore, in order to control the effect of pressure-sensitive property on production，the formation pressure should be controlled reasonably in development process. In this study, the factors, especially the fracture development directions, which show significant influence on the oil recovery of CO_2 flooding in fractured and pressure-sensitive reservoirs, were studied with physical experiments and numerical experiments. The results obtained in the study can provide a more reliable theoretical basis for CO_2 flooding design and profile control technology.

Keywords: CO_2 flooding, pressure-sensitive, fracture direction.

[*] Corresponding author : State key Laboratory of Petroleum Resources and Engineering, China University of Petroleum, Yuetian Liu, Beijing 102249, China.

1. Introduction

There are many indoor methods for testing permeability. As early as the last century 50's, there are many foreign scholars put forward the appropriate test methods and experimental devices. Philippe Renard (2001) through the theoretical calculation and indoor test comparative analysis of the main factors affecting the test error are anisotropic principal value, direction of the permeability, and the sample length to diameter ratio. Green Korn (1964) proposed a similar test method, but still did not solve the calculation problem of anisotropic permeability tensor. Yves Bernabé (1992) obtained the full tensor permeability of the sample by changing the injection conditions which lead to different boundary conditions. After that the corresponding inverse problem had been solved. Bieber (1996) used point tracer water injection and X-ray tomography to directly observe the flow patterns within the sample. If the flow form is spherical, the medium is isotropic. If that is ellipsoid, it is anisotropic. However, most of the fracture permeability tensor tests and theoretical calculations are only applicable to anisotropic media, can't accurately measure and calculate the total tensor of anisotropy permeability. Therefore, it is still a difficult problem to obtain the fracture permeability value when the direction of permeability principal value have angle with the displacement pressure gradient. Due to CO_2 and the oil have large difference in the mobility, it is easy to lead to gas finger or gas cone caused the production decline. When the fracture in different directions and the reservoir has a pressure-sensitive effect, the law of production decline will be more complicated. Therefore, it is of great practical significance to study the influence of fracture direction on the flow pattern of pressure-sensitive reservoir.

2. A Theoretical Model for Calculating Fracture Aperture

The fractures of low permeability reservoirs are more developed, the matrix is used as the reservoir reserve space of oil, and the fractures are the flow channels of oil flow. The properties of fractures play an important role in oil production in low permeability oilfields. Therefore, the correct calculation of the aperture of the fracture is a very important work. As shown in Figs.1 to 4, the fractured core is obtained by applying the Brazilian splitting principle to the horizontal seam, and the fracture surface remains uncontaminated. The permeability of the matrix portion of the fracture core is equal to that of the homogeneous core. The gas permeability in the matrix core is (Equation 1):

$$k_m = \frac{2\mu q_m p_0 L}{A(p_1^2 - p_2^2)} \tag{1}$$

The gas permeability in the fractured core is (Equation 2):

$$k_{avg} = \frac{2\mu q_{avg} p_0 L}{A(p_1^2 - p_2^2)} \tag{2}$$

The permeability of a single fracture is (Equation 3):

$$k_f = 8.44\times10^9 w^2 \tag{3}$$

In a fractured core, the core flow rate is equal to the sum of the flow in a single fracture and the flow of the matrix(Equation 4),

$$q_{avg} = q_f + q_m \tag{4}$$

To sum up (Equation 5):

$$8.44\times10^9 w^3 l - k_{avg} A + k_m (A - wl) = 0 \tag{5}$$

The fracture aperture is obtained by the Equation 5, so that the flow rate of the fluid in the matrix and the fracture are (Equation 6):

$$q_m = \frac{6k_m A(p_1^2 - p_2^2)}{10\mu p_0 L}; \quad q_f = 5.064\times10^8 \cdot \frac{w^3 l(p_1^2 - p_2^2)}{\mu p_0 L} \tag{6}$$

Where k_m = matrix permeability, $10^{-3}\mu m^2$. k_f = fracture permeability, $10^{-3}\mu m^2$.q_m , q_f = flow rate in the matrix and fracture, respectively, cm^3/min. p_1, p_2 = absolute pressure of the core inlet and outlet, respectively, MPa. w = fracture aperture, cm. p0 = atmospheric pressure, MPa. l = fracture length, cm.

Figure 1. Matrix Core Seepage Diagram.

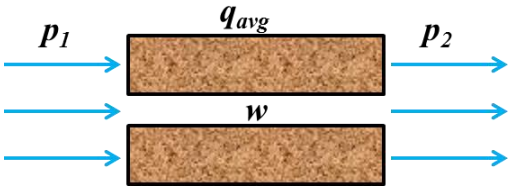

Figure 2. Fracture Core Seepage Diagram.

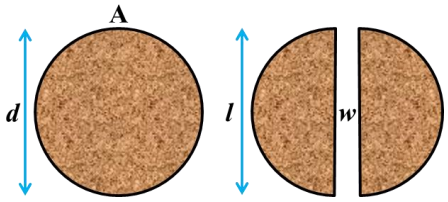

Figure 3. Cross Section of Matrix And Fracture.

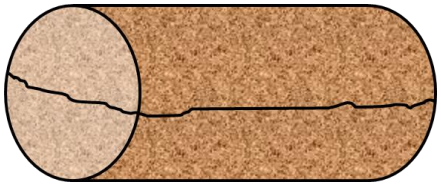

Figure 4. Fractured Core Diagram.

3. Physical Simulation

3.1 Effect of pressure on fracture permeability

All parameters are same as the theoretical model. In order to intuitively observe the dynamic change process of the fracture opening when the fluid pressure changed, the red dye agent is added to the distilled water and the plexiglass tank is used as the experimental model container (Fig.5).

3.2 Effect of pressure on fracture permeability

As shown in Figure.6: When the pressure gradient (pressure difference) is kept constant, as the pressure on the media increases, the overall fracture permeability increases.

Figure.7 is for the relationships between pressure difference and flow rate at the average pressure of 12kPa. As the pressure gradient or injection pressure increases, the flow begins to increase first, and the peak appears in the middle and then begins to decrease. It can be seen that in order to obtain the maximum productivity benefit in the actual oilfield development, it is not the bigger the better on the pressure difference, but existence an optimal value, which is very instructive for the reasonable development of the actual reservoir.

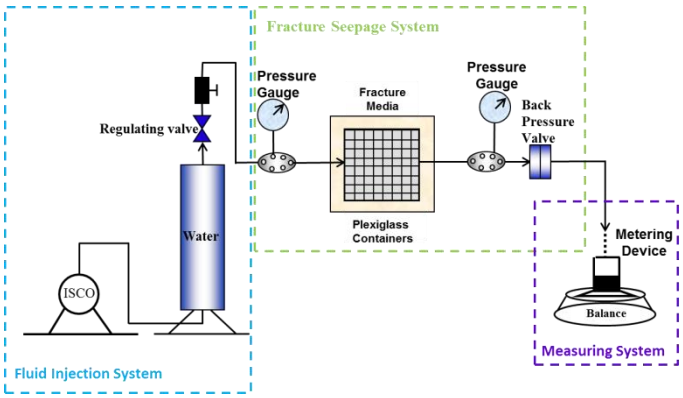

Figure 5. Experimental Device Diagram.

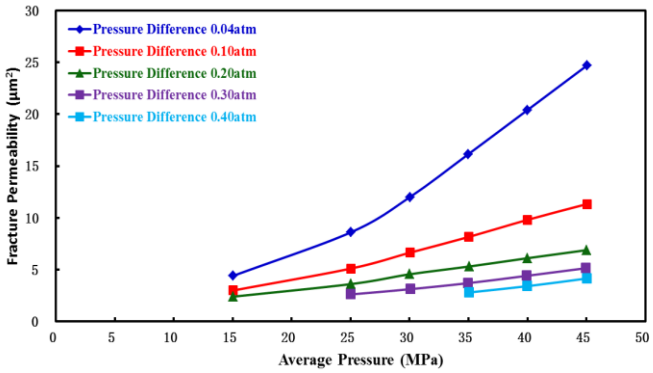

Figure 6. Fracture Permeability With Average Pressure.

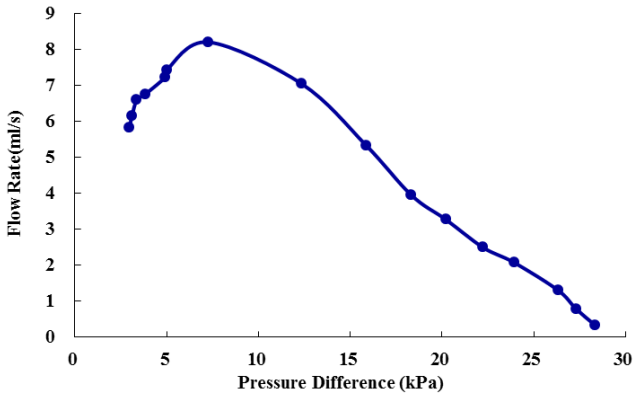

Figure 7. Relationships Between Pressure Difference and Flow Rate at the Average Pressure of 12kPa.

4. Experimental Simulation

The experiment procedure was also simulated by COMSOL Multiphysics. Parameters of the model are the same as the experimental model. Due the development direction of the fractures are different, the reservoir area with preferential pressure spread direction in the development is different (Fig. 8).

As shown in Fig. 9, the pressure is preferentially propagated along the direction of the fracture. As the production process progresses, the pressure gradually affects the matrix around the fracture, and the use degree of matrix is gradually increased. The development direction of the fractures is different, and the reservoir area with preferential pressure spread direction is different. Corresponding to the actual reservoir, different regions with different reserves abundance, the initial production capacity of the production wells will be very different. And ultimately reach a steady state. When the models both have reached a steady state, the total pressure spread area is not same between them. The place where the pressure could not reach, that is difficult to recovery oil and gas even if the reserves are high. Therefore, the angle between the direction of the fracture and the direction of the pressure gradient will affect the final recovery of the reservoir.

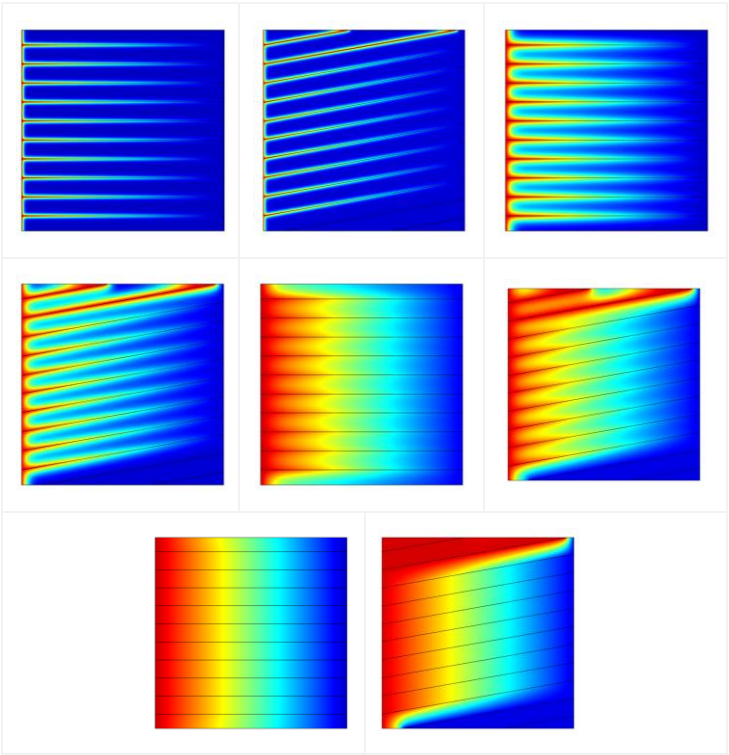

Figure 8. Pressure Propagation Path.

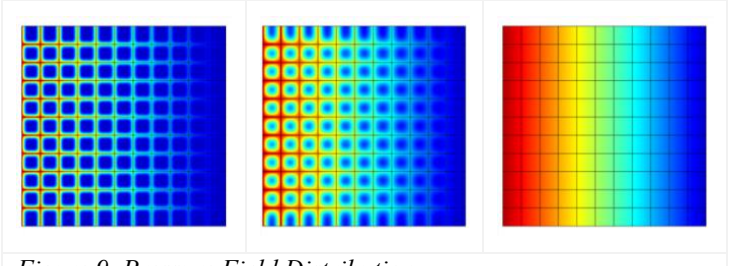

Figure 9. Pressure Field Distribution.

5. Conclusion

(1) In the low permeability heterogeneous reservoir, with the increase of the effective pressure, the permeability loss in low permeability layer is higher than that of in the high permeability layer. Low permeability fractured reservoir have strong pressure sensitivity, which is caused by the closure of fractures and the deformation of matrix. When the effective pressure is low, the closure of the fracture aperture causes the permeability decrease sharply. With the increase of the effective pressure, the fracture aperture decreases. When the fracture aperture is closed to a certain level, the matrix permeability also began to decrease. And the lower the matrix permeability is, the stronger the pressure sensitivity of the reservoir.

(2) The gas channeling in the low permeability fractured press sensitive reservoir is related to the fracture property. With the effective pressure increase, the fracture in different directions will occur varying degrees of closure , resulting in the gas transfer from the fracture to the matrix , thereby the use of oil in the matrix will increase. When the effective pressure is too high, it will lead to loss of permeability of the matrix, thereby reducing the production capacity of matrix. When the matrix permeability is low, the fracture core can obtain a high gas flooding efficiency with the effective pressure kept at a high level.

Acknowledgements

The paper is sponsored by National Natural Science Foundation Project No. 51374222, National Major Project No. 2017ZX05032004-002, and The National Key Basic Research & Development Program No. 2015CB2509005.

References

Philippe Renard, Alain Genty, Fritz Stauffer. 2001. Laboratory determination of the full permeability tensor. Journal of geophysical research, vol.106, pages 26,442-452. *DOI: 10.1029 / 2001 JB000243.*

Green Korn R A, Johnson C R. 1964. Directional permeability of heterogeneous anisotropic porous media. SPE J, 1964, 4 (2): 115-122. *DOI: 10.2118/788-PA.*

Bernabé, Y. 1992. On the Measurement of Permeability in Anisotropic Rocks. International Geophysics, Volume 51, Pages 147–167. *DOI: 10.1016/S0074-6142(08)62821-1.*

Bieber, R. L., P. Rasolofosaon, B. Zinszner, et al. 1996. Measurement and overall characterization of permeability anisotropy by tracer injection. Rev. Inst. Fr. Pet., 1996, 51(3): 332-347. *DOI: 10.2516/ogst:1996028.*

Comsol , 2015. Multiphysics Model Library, Earth Science Module, Version 5.0.

Mi, L., Jiang, H., Li, J., 2014a. The impact of diffusion type on multiscale discrete fracture model numerical simulation for shale gas. J. Nat. Gas Sci. Eng. 20, 74e81. *DOI: 10.1016/j.jngse. 2014.06.013.*

Mi, L., Jiang, H., Li, J., Li, T., Tian, Y., 2014b. The investigation of fracture aperture effect on shale gas transport using discrete fracture model. J. Nat. Gas Sci. Eng.21, 631e635. *DOI: 10.1016/j.jngse.2014.09.029.*

Chao Zhou, Xiaodong Wu, Hui Li, et al. 2015. Influence of In-situ Stress Distribution on Selection of Fracturing Fluid Backflow Technology(ICCESEN 2015), 14-19 October, 2015 Antalya-Turkey. *DOI: 10.12693/APhysPolA.130.347.*

M.E. Başak, F. Kaçar. 2015. Ultra-Low Voltage VDCC Design by Using DTMOS(ICCESEN 2015), 14-19 October, 2015 Antalya-Turkey. *DOI: 10.12693/APhysPolA.130.223.*

S. Gedik, A.F. Baytaş. 2014. Shielding of Gamma Radiation by Using Porous Materials (ICCESEN 2014), 25-29 October, 2014 Antalya-Turkey. *DOI: 10.12693/APhysPolA.128.B-174.*

Avrupa Bilim ve Teknoloji Dergisi
Özel Sayı, S. 26-29, Aralık 2017

Konferans Bildirisi

www.ejosat.com ISSN:2148-2683

European Journal of Science and Technology
Special Issue, pp. 26-29, December 2017

Conference Paper

Dynamical Analysis of the Multispan Beams with Method of Multiple Scales

B. Gültekin Sınır[1]*, D. Duygu Dönmez Demir[2], Leyla Usta[3]

[1] Corresponding author : Manisa Celal Bayar University, Faculty of Engineering, Department of Civil Engineering, 45140, Manisa, Turkey, gultekin.sinir@cbu.edu.tr
[2] Manisa Celal Bayar University, Faculty of Arts & Sciences, Department of Mathematics, 45047, Manisa, Turkey, duygu.donmez@cbu.edu.tr

Abstract

Multi-span beams are statically indeterminate structures in general. They have many applications in civil engineering, mechanism, navigation engineering and so on. For example, multi-span bridges have been widely used in highway and railway. It is of great importance to study the dynamic characteristic of the multi-span beams for engineering design and scientific research. Many engineers and scientists have contributed to the solution of the problem with their innovations, and still the subject draws considerable attention from researchers by now. In this study, we investigate primary resonance case of multi-span beam subject to axial load. Firstly, the mathematical model of the problem is derived by using extended Hamilton principle. This model has geometric nonlinearity. Here, two system of partial differential equations are obtained for axial direction and transverse direction. The numbers of equations and boundary conditions depends on span number. After coupling equations in transverse and axial directions, the system of nonlinear integro-differential equations are obtained and solved using the method of multiple time scales.

Keywords: Method of multiple scales, nonlinear vibration, multi-span beam, primary resonance.

* Corresponding author : Celal Bayar University, Faculty of Engineering, Department of Civil Engineering, Manisa, Turkey, gultekin.sinir@cbu.edu.tr, phone: +90 2362012316

1. Introduction

There are many studies related to multi-span beam structures in the literature. Multi-supported (multi-span) beams can be applied to some different engineering areas. For example, Henchi et. al. [1] consider dynamic response of multi-span beams as bridges. The beams are under a convoy of moving loads. In another interesting study, the transverse vibrations of an axially accelerating Euler–Bernoulli beam with multiple simple supports are examined [2]. Kesimli et. al. [3] analyse nonlinear vibrations of an axially accelerating multi-supported spring and determine both stable and unstable areas. In some studies, multi span beams is considered as pipes conveying fluid [4]. They present the Timoshenko beam model instead of the Euler Bernoulli beam.

In this study, the solution of the nonlinear mathematical model of the multi-span Euler-Bernoulli beam is presented. As a solution technique, the method of multiple scales is preferred. Applying the method of multiple scales and separating the equations at each power of small parameter, linear differential equations are obtained at each order of small parameter instead of the system of integro-nonlinear differential equation. The principal primary resonances case is analyzed and the stability boundaries and regions are investigated. The obtained results are shown by graphs.

2. Solution Using Method of Multiple Scales

Adding a visco-elastic damping term into the equation of motion in Ref. [5], one obtains

$$\ddot{w}_m + \bar{\mu}\dot{w}_m + \frac{\partial^4 w_m}{\partial x_1^4} - \frac{\partial^2 w_m}{\partial x_1^2}\left[\sum_{m=1}^{M}\int_{x_{m-1}}^{x_m}\left(\frac{\partial w_m}{\partial x_1}\right)^2 d\hat{x}_1\right] - \lambda^2\frac{\partial^2 \ddot{w}_m}{\partial x_1^2} + P\frac{\partial^2 w_m}{\partial x_1^2} = \bar{F}_m\cos\Omega T_0 \tag{1}$$

where $m,\ \lambda, P$ and $\bar{F}$ denote different support locations, the fineness coefficient, the axial compressive force and external excitation with amplitude, respectively. In this study, we consider the equation of motion for two span. The method of multiple scales is directly applied to the governing equation to find the general solution of Eq. (1). The perturbation expansion for $w_m(x,t)$ is assumed

$$w_m(x,T_0,T_2;\varepsilon) = \varepsilon w_{m1}(x,T_0,T_2;\varepsilon) + \varepsilon^3 w_{m3}(x,T_0,T_2;\varepsilon) + \mathrm{K}\ ;\ m=1,2 \tag{2}$$

where ε is a small parameter artificially inserted into the equations; $T_0 = t$ is usual fast time scale, $T_1 = \varepsilon t$ is slow time scale. We consider only the primary resonance case and hence, the forcing and damping terms are ordered so that they counter the effect of nonlinear terms: that is

$$\bar{\mu} = \varepsilon^2\mu \qquad\qquad \bar{F}_m = \varepsilon^3 F_m \tag{3}$$

$D_n = \partial/\partial T_n$, its derivatives have been expressed in time. Substituting Eqs. (3) into Eq. (1) and separating at each order of ε, one obtains

$$O(\varepsilon^1): D_0^2 w_{m1} - D_0^2\lambda^2 w''_{m1} + P'' w_{m1} + w^{iv}_{m1} = 0 \tag{4}$$

$$O(\varepsilon^3): D_0^2 w_{m3} - D_0^2\lambda^2 w''_{m3} + P'' w_{m3} + w^{iv}_{m3} = -2D_0D_1 w_{m2} - \mu D_0 w_{m1} + 2\lambda^2 D_0 D_1 w''_{m2} - \left(D_1^2 + 2D_0D_2\right)w_{m1} + \frac{1}{2\lambda^2}w''_{m1}\left[\sum_{m=1}^{2}\int_{x_{m-1}}^{x_m} w'^2_{m1}\,dx_1\right] + F_m\cos\Omega T_0 \tag{5}$$

The problem at orders ε is linear. The generating solution at order ε are assumed as

$$w_{m1} = \left(A_m(T_2)e^{i\omega_m T_0} + \bar{A}_m(T_2)e^{-i\omega_m T_0}\right)X_m(x_1);\quad m=1,2 \tag{6}$$

where A_m and $\bar{A}_m$ are complex amplitudes and their conjugates, respectively. Substituting w_{m1} solution into this relation, we obtain

$$O(\varepsilon^3): D_0^2 w_{m3} - D_0^2\lambda^2 w''_{m3} + P'' w_{m3} + w^{iv}_{m3} = -\mu i\omega_m X_m(x_1)\left(A_m(T_2)e^{i\omega_m T_0} - \bar{A}_m(T_2)e^{-i\omega_m T_0}\right) - 2i\omega_m X_m(x_1)\left(D_2A_m(T_2)e^{i\omega_m T_0} - D_2\bar{A}_m(T_2)e^{-i\omega_m T_0}\right) + F_m\cos\Omega T_0 + \frac{b}{2\lambda^2}\left(A_m(T_2)e^{i\omega_m T_0} + \bar{A}_m(T_2)e^{-i\omega_m T_0}\right)X''_m(x_1) \tag{7}$$

where

$$b = \sum_{m=1}^{2}\int_{x_{m-1}}^{x_m}\left[\left(A_m(T_2)e^{i\omega_m T_0} + \bar{A}_m(T_2)e^{-i\omega_m T_0}\right)X'_m(x_1)\right]^2 dx_1 \tag{8}$$

We consider the primary resonance case. Besides, we assume that the external excitation frequency approximately the natural frequencies of the system, that is $\Omega \approx \omega_m + \varepsilon^2\sigma$ where σ and ω_m denote the detuning parameter and the natural frequency. The detuning parameter represents the nearness of the external excitation frequency to the natural frequency of the system. Applying the normalization as

$$\sum_{m=1}^{2}\int_{x_{m-1}}^{x_m} X_m^2\,dx_1 = 1, \qquad F = \sum_{m=1}^{2}\int_{x_{m-1}}^{x_m} F_m X_m\,dx_1 \tag{9}$$

eliminating secular terms, then, the resulting equation is obtained as

$$D_0^2 w_{m3} - D_0^2\lambda^2 w''_{m3} + P'' w_{m3} + w^{iv}_{m3} = 2i\omega_m\left(\lambda^2 X''_m(x_1) - X_m(x_1)\right)D_2A_m(T_2) + F_m e^{i\sigma T_2} - \mu i\omega_m X_m(x_1)A_m(T_2) + \frac{b}{2\lambda^2}X''_m(x_1) \tag{10}$$

Applying the solvability condition into Eq. (10), one obtains

$$2i\omega_m\left(\lambda^2 - 1\right)D_2A_m - \mu i\omega_m A_m + \frac{b}{2\lambda^2}A_m^2\bar{A}_m + F_m e^{i\sigma T_2} = 0 \tag{11}$$

It is convenient to write the polar form in the following instead of A_m

$$A_m = \frac{1}{2}a_m(T_2)e^{i\beta_m(T_2)} \tag{12}$$

where a_m and β_m are real functions of T_2. The solution is obtained by substituting the polar form of A_m into the Eq. (11) and separating the resulting equation into imaginary and real parts as

$$\omega_m a_m\left(1-\lambda^2\right)\left(\sigma-\gamma_m'\right)-\frac{ba_m^3}{16\lambda^2}=F_m\cos\gamma_m \tag{13}$$

$$-\omega_m\left(\lambda^2-1\right)a_m'+\frac{1}{2}\mu\omega_m a_m=F_m\sin\gamma_m \tag{14}$$

where $\gamma_m=\sigma T_2-\beta_m$. For steady state case $\gamma_m'=a_m'=0$, with the same mathematical procedures, the stability boundaries are found as

$$\sigma_{1,2}=\frac{1}{a_m\omega_m\left(1-\lambda^2\right)}\left(\frac{ba_m^3}{16\lambda^2}\pm\sqrt{F_m^2-\left(\frac{1}{2}\mu\omega_m a_m\right)^2}\right) \tag{15}$$

3. Numerical Results

In this section, some numerical results are presented for stability boundaries of primary resonances. The nonlinear frequencies for all cases are shown in Fig. 1-3. The region between two lines is unstable region in Fig. 1-3. The dashed lines are unstable boundaries. The solid lines are stability boundaries. When η increases, the frequencies are lower in Fig1. The effect of the values X_m on the stability region is too limited. The nonlinear terms are more effective for smaller slenderness ratio in Fig 2. The frequency–response curves shown for different F values in Fig.3. For larger F values, the unstable region is getting larger (In all figures, the horizontal axis represents σ and the vertical axis denotes a_m).

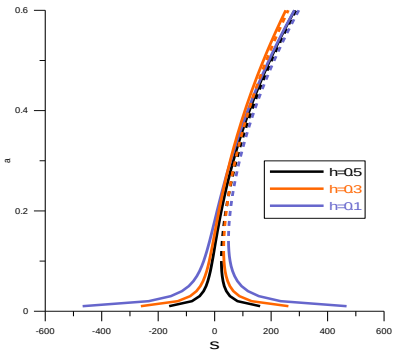

Figure 1. Frequency–response curves

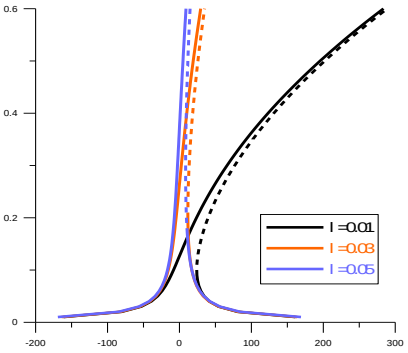

Figure 2. Frequency–response curves for different slenderness ratio curves.

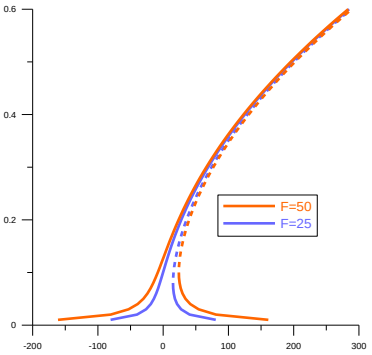

Figure 3. Frequency–response curves for different external excitation with amplitude.

4. Conclusions

The nonlinear mathematical model of the beam having two number of the span is introduced. As a solution technique, the method of multiple scale is used. The primary resonance case of the beam under harmonic external excitation is analysed. The effect of support location on the stability boundaries is presented. The effect of the location of internal support is getting higher for smaller slenderness ratio.

References

[1] Henchi K., Fafard M., Dhatt G., Talbot M. 1997. Dynamic behaviour of multi-span beams under moving loads 199, 33-50.

[2] Bağdatlı S.M., Özkaya E., Öz H.R. 2013. Dynamics of axially accelerating beams with multiple supports 74, 237–255.

[3] Kesimli A., Özkaya E., Bağdatlı S. M. 2015. Nonlinear vibrations of spring-supported axially moving string 81, 1523–1534.

[4] Bao-hui L., Hang-shan G., Hong-bo Z., Yong-shou L., Zhu-feng Y., 2011. Free vibration analysis of multi-span pipe conveying fluid with dynamic stiffness method, 241, 666–671.

[5] Dönmez Demir D., Sınır B.G., Usta L. 2016. Determining Critical Load in the Multi-span Beams with the Nonlinear Model, ICNPAA2016 World Congress11th International Conference on Mathematical Problems in Engineering, Aerospace and Sciences, La Rochelle, France.

Avrupa Bilim ve Teknoloji Dergisi
Özel Sayı, S.30-33, Aralık 2017

Konferans Bildirisi

www.ejosat.com ISSN:2148-2683

European Journal of Science and Technology
Special Issue, pp.30-33, December 2017

Conference Paper

Physical Leakage Analysis in Water Distribution Networks By Daily Consumption Curve

Recep Kılıç[1]*, Hüseyin Cinal[2]

[1]Corresponding author : Sakarya University, Vocational School of Sakarya, Adapazarı, Sakarya, Turkey, recepkilic@sakarya.edu.tr
[2]Sakarya Water And Sewerage Administration, Adapazarı, Sakarya, Turkey, huseyin.cinal@sakarya-saski.gov.tr

(First received 25 August 2013 and in final form 20 December 2013)

Abstract

The curve of daily water consumption in drinking water networks provides a lot of information on the physical status of the network. The existing physical leakage rate can be estimated by analyzing the network water consumption curve. Hence, precautions can be taken in order to prevent the physical leakages and water losses. In this study, the minimum night flow (MNF) that occurs in the determined measurement areas (DMA) in the current drinking water network was examined, and it was attempted to determine the required amount of consumption and water loss by determining the amount of leakage. Pressure management was started to be used in the distribution system, and the effect of pressure management on the water consumption in DMAs was examined. Operation and rehabilitation methods were suggested by determining the amount of physical leakage in the network.

Keywords: Physical Leakage, Water Demand, Water Distribution Network.

* Corresponding author : Sakarya University, Vocational School of Sakarya, Adapazarı, Sakarya, Turkey, recepkilic@sakarya.edu.tr, phone: +90 533 470 40 38

1. Introduction

Introduction

In many countries of the world there is an increasing evidence of inadequate water distribution systems, due to the deterioration of ageing infrastructure (especially pipes and pumps), the rapid growth of urbanization, and the statutory and contractual quality standards that have to be offered to consumers. In particular, regulatory bodies and water utilities are concerned about the importance of accurately assessing and controlling water losses, which may have a strong impact also on energetic costs (Nicolini et al., 2014).

The availability of drinking water has represented a key factor in the development of more advanced countries, and of the developing ones. Therefore efficiency and reliability of hydraulic networks are requirements sought by water networks administrators. Due to inefficient aqueduct systems every year more than 48 billions of cubic meters of water are lost all around the world, that correspond to an economic loss of more than 14 billions US-dollars. In the only United States of America, the American Water Works Association (AWWA) estimates that during the 2002 up to 10 billions kWh of electric energy were used to pump water that was lost in the leakages. The identification and localisation of water leakages is a challenging task due to the topographical complexity of the water systems to be analysed, that can be constituted by a large amount of users, ramifications of the pipes, and water tanks (Debiasi et al., 2014).

A number of methods exist for identifying leakage. The most established method is sectorization. This involves the permanent closure of isolation valves in the water distribution network to create discrete zones, commonly called district metered areas (DMA). The closed isolation valves are therefore commonly called boundary valves (BV). A flow meter is then installed at each DMA inlet and outlet. By measuring the flow during times of low customer demand (such as at night), an estimation for leakage can be made, and DMAs prioritized for repair (Wright et al., 2015).

The leakages quantification is done through a water balance on a system-wide basis in a restricted District Metering Area (DMA). Monitoring of leakages allows the engineers to quantify the water flow into the DMA thus discriminating when abnormal water consumptions can be associated to water losses. Flows and pressures are measured on different points on the DMAs usually constituted by up to 3,000 properties. During the data analysis only the information collected at night (between 02:00 AM and 04:00 AM) are considered because in this moment of the day it is registered the minimum flow (MNF), therefore the pressures and the effects of leakages on the water network are maximum (Debiasi et al., 2014).

1.1 Background Leakage

Water distribution system (WDS) losses may be classified as due to background losses (e.g., from joints, fittings, and small cracks), reported bursts, and unreported bursts. Bursts are intended as major water outflow events that are usually reported to water utilities and repaired since they are likely to produce major service disruptions. For this reason burst are commonly considered as accidents whose impact on WDS can be limited by improving active leakage control and the efficiency of detection and repair actions. Vice versa, background leakages are intended as outflows running from small cracks, holes, deteriorated joints or fittings, occurring along pipes. As diffused water outflows, background leakages do not result into evident and quick pressure drops through the network, thus they are not reported and run for longer time, producing relevant impact in terms of WDS water lost volumes. For this reason background leakages can be reduced by planning medium-long term interventions for asset rehabilitation and pressure management (Laucelli and Meniconi, 2015).

According to Torricelli's theorem, the rate of leakage Q1 is proportional to the square root of the pressure head H in a pipe.

$$Q_1 = C_1 A_1 \sqrt{2gH} \quad (1)$$

where

Cl is the discharge coefficient

Al is leak area

g is the acceleration due to gravity

h is the total head at the point of leak

Several researchers have conducted tests on orifice in pipes and the hydraulics is now very well understood. The rate of leakage is in fact proportional to the square root of the head at that particular leak point irrespective of the pipe material and size of hole, thereby confirming the relationship:

Q1αH0.5 (2)

However, leaks are not always of orifice type and therefore other shapes like circumferential and longitudinal cracks were investigated. A more general form of the leak equation which is proposed is:

$$Q_1 = CH^N \quad (3)$$

where

C is the leakage coefficient

N is the leakage exponent

Rewriting the leak flow equation 1 according to FAVAD:

$$Q_1 = C_d A_1 \sqrt{2g} (A_0 H^{0,5} + mH^{1,5}) \quad (4)$$

where

A_0 is the initial leak area

m is the slope of the head-area curve (Latchoomun et al., 2015)

1.2 Leakage Estimation Using Minimum Night Flow and Leakage Exponent

Latchoomun et al. (2015) used the Minimum Night Flow measurements in order to calculate the real losses of a DMA and computed leakage exponent N1. They showed that the MNF method and the calibration process yield similar results in terms of leakage estimation.

The Daily Real loss Volume DRLV is given by

$$DRLV = F_{nd}\, xQ_{mn} \tag{5}$$

where

Q_{mn} is the average minimum nightly leak flow rate (m3/h)

F_{nd} is the night day factor

Since the leak volume varies with demand pattern, the minimum night flow is multiplied by Fnd

$$F_{nd} = \sum_{i=0}^{24} \left(\frac{P_i}{P_{3-4}}\right)^{N1} \tag{6}$$

where

P = the average pressure at the point of observation in the DMA for every hour i

P3-4 is the average pressure during minimum night consumption between 3 to 4 AM

N1 being the leak exponent obtained from the MNF.

The overall leakage exponent of the DMA is obtained as 1.645 by using equation 7 [4].

$$\frac{Q_1}{Q_0} = \left(\frac{P_1}{P_0}\right)^{N_1} \tag{7}$$

where

Q_1 is the final flow,

Q_0 is the initial flow,

P_1 is the final pressure head

P_0 is the initial pressure head.

2. Methodology

In this study, the daily water consumption was measured by dividing the drinking water network into DMAs. A pressure reducing valve was used in order to adjust the pressure according to consumer needs. The water flow was measured instantly using an electromagnetic flow meter, and the pressure and flow were recorded. The change of the leakages was examined by taking the pressure under control.

2.1 Description of System

Serdivan drinking water network is situated in the center of Sakarya city, and it was partially improved and not replaced after the earthquake that occurred on 17 August 1999. Therefore, it is a network, in which the number of breakdowns each year is high and the leakages that result from non-surface failures, and thus the water loss is high.

The DMA in which the study was carried out is a region called “Serdivan 1”. Figure 1 shows the general overview of the DMA and is formed by HDPE and PVC-type pipes. The total length of the network is 9935 m. The subscriber connection lines consist of iron pipes (old connections) and HDPE. The pipe diameters in the system are 25-32 mm for subscriber connections, and 110, 125 and 180 mm in distribution lines. Table 1 presents the general information on DMA. DMA expresses the general structure of the network. Thus, the electromagnetic flow meter and PRV (pressure reducing valve) were mounted at the inlet and taken under monitoring (Figure 1).

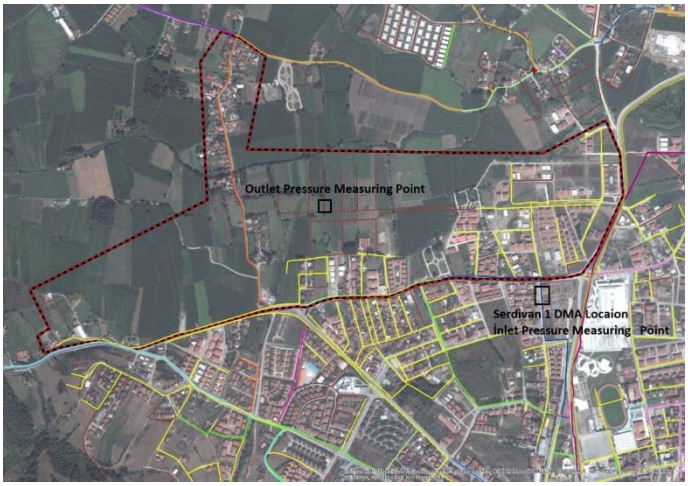

Figure 1. DMA of Serdivan 1 layout.

Table 2. Description of Serdivan 1 DMA.

Descriptions	**2014**	**(%)**
Total length of system (m)	9925	
Population served	4278	
Number of consumer	1337	
System daily average input volume (m^3)	700	100
Daily Average authorized consumption (m^3)	455	65
Daily water loss (m^3)	245	35

2.2 Case Study

The flow, inlet pressure and outlet pressure at the DMA inlet were measured and recorded. The current situation was determined by making an observation in this case for a certain period. The minimum required pressure in the network is 20 m. However, it was determined that the pressure inside the DMA is more than necessary. The flow and pressure values measured at the DMA inlet on 20.04.2014 are shown in Figure 2. The pressure increases when the flow decreases, and the pressure reaches the maximum level in the MNF.

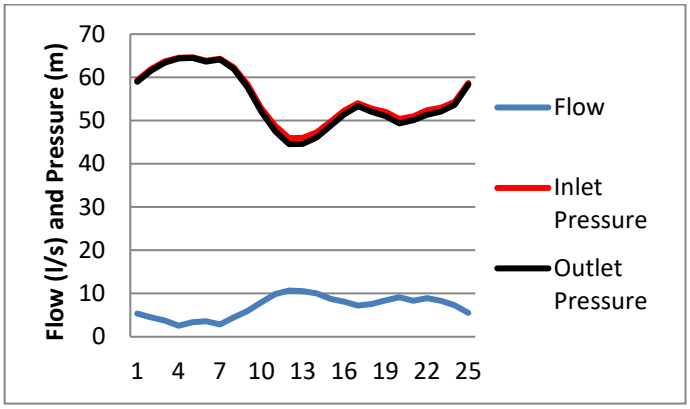

Figure 2. Flow and pressure.

The pressure was adjusted by using PRV so that the target value would be 35 m in such a way that there would be no decrease in the service quality of the users. Pressure was adjusted by using PRV. No decrease occurred in the user service quality after adjusting the pressure and the values measured in Figure 3 are observed. The outlet pressure remains constant independent of the inlet pressure and flow.

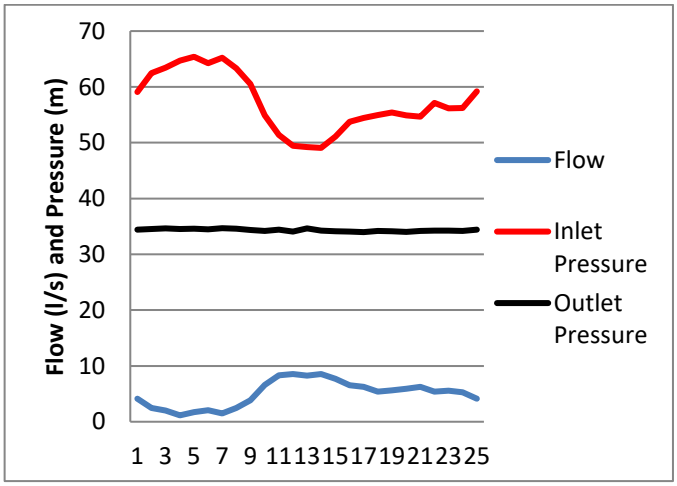

Figure 3. Flow and pressure chart.

3. Results

The computed average night day factor Fnd for normal flow using equation 6 is 19.50 h/day and the observed average MNF at the DMA entrance from data logger is 2.55 l/s or 9.18 m3/h. Therefore the DRLV according to equation 5 must be 7.46 m3/h or 2.07 l/s. 2.071/s of the measured 2.55 l/s MNF is DRLV, and only 0.48 l/s is night consumption. The average consumption in the DMA is 904.4 m3/d, in other words, 10.47 l/s on 20.04.2014 when the measurement was made. In this case, the water loss caused by the leakages in the network on 20.04.2014 is 20%.

The same equations did not give correct results for the practices made after the PRV. However, more consistent values were achieved when the calculations were made by taking the first inlet pressure as a reference after reducing the pressure, regardless of the PRV outlet pressures.

A decrease in the amount of water given to the DMA was determined after taking the pressure under control by using the PRV on 27.04.2014. After reducing the pressure, the daily consumption was measured as 621.8 m3/d, 7.20 l/s, on average, and MNF as 1.51 l/s. After reducing the pressure, the DRLV value was determined to be 0.97 l/s. It was determined that the amount of leakage in the network decreased to 13% with the reduction of the pressure.

4. Conclusion

Leakages in drinking water distribution networks can be determined by using many methods. However, a number of physical leakages in the infrastructure can be determined by determining only the daily consumption curve, and especially the minimum night flow (MNF) in the DMAs created when the technical capacities of local administrations are also taken into consideration. The breakdowns that are believed to exist in the DMA can be determined according to the amount of leakage determined. In this study, the water losses that result only from leakages were determined by identifying the MNF in the DMA. Hence, the development of activities for this objective can be helped by determining the target value that should be achieved by identifying the water consumption that must occur in each region. It will help the decision on replacing partial networks in the places where the MNF is very high.

References

Nicolini M., Giacomello C., Scarsini M., Mion M. 2014. Numerical modelling and leakage reduction in the water distribution system of, Procedia Engineering 70, 1241-1250. DOI: 10.1016/j.proeng.2014.02.137

Debiasi S., Giorgio Bort C.M., Bosoni A., Bertola P., Righetti M. 2014. Influence of hourly water consumption in model calibration for leakage detection in a WDS, Procedia Engineering 70, 467-476. DOI: 10.1016/j.proeng.2014.02.052

Wright R., Parpas P., Stoianov I. 2015. Experimental investigation of resilience and pressure management in water distribution networks, Procedia Engineering 119, 643-652. DOI: 10.1016/j.proeng.2015.08.917

Laucelli D., Meniconi S. 2015. Water distribution analysis accounting for different background leakage models, Procedia Engineering 119, 680-689. DOI: 10.1016/j.proeng.2015.08.921

Latchoomun L., Ah King R.T.F., Busawon K. 2015. A new approach to model development of Water distribution networks with high leakage and burst rates, Procedia Engineering 119, 690-699. DOI: 10.1016/j.proeng.2015.08.922

Avrupa Bilim ve Teknoloji Dergisi
Özel Sayı, S.34-37, Aralık 2017

Konferans Bildirisi

www.ejosat.com ISSN:2148-2683

European Journal of Science and Technology
Special Issue, pp. 34-37, December 2017

Conference Paper

Restructuring of University Laboratories within the Scope of Occupational Health and Safety

Kamil Musa Ordu[1*], Gülçin Çivi Bilir[2]

[1] Corresponding author: Istanbul Technical University, Workplace Health and Safety Unit, Maslak, 34469, Istanbul, Turkey,
[2] Istanbul Technical University, Workplace Health and Safety Unit, Maslak, 34469, Istanbul, Turkey,

*Email: orduk@itu.edu.tr

Abstract

Laboratory safety is major of importance to occupational health and safety, which manages, and responds to all issues and concerns surrounding physical, biological, ergonomic, electrical, chemical, and other standard operating procedures.

In this work, laboratory design and equipment, which are arranged according to precautions that are taken against to all hazards regarding to work environment or personal expose at the work environments in laboratories that are already exist or will be established in universities, are discussed according to legislation and regulations of Occupational Health and Safety Law No. 6331. In addition, some examples of Occupational Health and Safety applications of leading university laboratories in the world are given.

Keywords: Laboratory safety, hazard, occupational health and safety law.

1. Introduction

It is quite important to build up the culture of occupational health and safety, which becomes a discipline that has increasing importance day by day in our country as well as world, in laboratories, which are already exist or will be established in universities, and supply sustainability of this culture.

Asumeng et al. (2015) categorized the hazards as biological, physical, ergonomic, chemical, psychological and defined management of these hazards. İleri (2014) studied the hazards in mining, construction, metal industry, textile industry, agriculture industry, and asbestos ship dismantling, repair and maintenance motor vehicle industry, shipyards, etc.

On the other hand, laboratories are considered dangerous environments as a place of work and may carry many risk factors that can cause occupational accidents. In this manner, it is very important that laboratory users should follow the regulations and safety rules in order to eliminate or minimize the risks for laboratory users working with biological, physical, chemical and radioactive substances, and electrical accident associated with low/high voltage. A variety of hazards exists in university laboratories. To manage these hazards, and in response to a heightened concern for safety in the workplace, university has to preserve safety and health of the lab users and provide enable the work secure in laboratory spaces according to the current law and regulations.

2. Laboratory Hazards

Laboratory spaces in university area considered high-risk environment when compared to other areas like offices, amplifier classes and cultural center etc. Laboratory hazards may result health effects in short or long terms. All persons working in a university laboratory may be exposed to under these hazards, which can be categorized as

- Physical Hazards (vibration, noise, insufficient air condition, excessive heat, humidity, and air movements, insufficient or excessive lighting, high electromagnetic fields, gases under pressure such as compressed gases, liquefied gases, refrigerated liquefied gases, dissolved gases, etc.),
- Biological Hazards (bacteria and viruses, insect bites, fungi/mold, blood and other body fluids, working with animals, poisoning plants, etc.),
- Ergonomic Hazards (improperly adjusted workstations and chairs, frequent lifting, repeating the same movements over and over can be taken as ergonomic hazards, etc.),
- Electrical Hazards (deficiency in periodic controls, grounding system problems in electric circuits, damaged and repaired faulty hand tools, insulated floor, high voltage in the study with required rules, interference of unauthorized persons, etc.) and,
- Chemical Hazards (toxic gases, organic vapors of liquids, gases of the molten metal, acids and bases due to combustion, inert powder, fibrojenik powder, powders of toxic, carcinogenic, allergenic dusts, hazardous waste, flammable materials like solvents, explosive chemicals, etc.).

Many scientific or technological research, experiments, and measurements may be performed in university laboratories. Thus, the use of physical, biological, ergonomic, electrical, chemical methods including their technical applications contains a number of risks defined above.

In this manner, the laboratory design and planning has played an important role to destroy or minimize the risks, which may occur in laboratory space.

3. Laboratory Design and Planning

The safety culture in a university encompasses a health and safe environment achieved through everyone understands of his or her responsibilities, rights, and university safety policies. As a part of safety culture; safety assessments for university laboratories should be covered laws, policies, planning, applications, evaluation and measurement. It is important to know how to plan laboratory design in universities. In this framework, according to legislations related to Occupational Health and Safety Law No. 6331 design and planning can be taken into account as follows (6331 sayılı İş Sağlığı ve Güvenliği Kanunu, 2012).

3.1 Walls, doors, floors and ceilings

Designers must select materials cleanable, alterable and appropriate for maintenance. Walls and corner protection should be provided where equipment or user traffic occur regularly. Laboratory doors should open in the direction of exit and close itself. In addition, doors provided with vision panels should have from the outside by a key and push bar from the inside. The floor should be covered up resistant, cleanable, seamless and non-slip material. Ceiling panels and modules should be taken into account by considering usage requirements and the necessary lab class. Insulation in walls and the ceiling reduces acoustical problems. Since the ceiling covering materials must be cleanable, acoustical design for ceiling cannot be destroy the noise fully (Binaların Yangından Korunması Hakkında Yönetmelik, 2007).

3.2 Air quality, ventilation

Particulate emissions and other air pollutants should be considered in laboratories design and operations so as to minimize such emissions and promote the health of the laboratory users. All laboratories shall have mechanical ventilation and parts using 100% outside air and exhaust to the outside. The Local ventilation systems are to designed to remove the contaminants generated by an experiment or device outside of the building involving laboratory. Heating, ventilation and air-conditioning (HVAC) systems should be consider during laboratory design for temperature, humidity, and air quality.

3.3 Lighting and electrical systems

The appropriate design of lighting systems is especially important in university laboratories in terms of significance of work carried out in laboratories and the long work hours spent by users. According to the Turkish lighting standard numbered

TS EN 12464-1: 2013, day lighting should be maximized and lighting should be even across the room with a maintained light level capable of 500 lux on the work area. A combination of lighting zones, dimmable fixtures, and controlled daylight and occupancy sensors with adjustable sensitivity in the room is ideal.

Laboratories should have a sufficient number of electrical outlets and informed from the users to eliminate the need of extension cords and multi-plug adapters. Electric outlets should be coordinated with the electrical characteristics of the laboratory equipment. Emergency power distribution should be considered as required to serve the equipment and loads as a minimum such as domestic water system, environmental rooms, critical equipment, refrigerator, freezers, cold rooms, critical laboratory equipment and their required support systems, one circuit per lab module for discretionary convenience receptacle, fume hoods and their exhaust and makeup air systems, 33% of lighting in laboratories, procedure rooms, and equipment areas, equipment and communications technology power distribution systems, entire animal facilities. Storage should be at least 1 m from electrical panels, mechanical rooms, air ducts, heaters, light fixtures in Laboratories. In emergency cases, it may be necessary to access these panels quickly.

3.4 Chemical storage rooms and waste minimization

There are many potential chemical hazards in laboratories involving chemical materials. Laboratories design should be designed to satisfy with the appropriate precautions. Planning should be involved storage rooms such that, the quantities that may be stored, handled and used in a laboratory unit, chemicals for use in a laboratory unit may be stored in a dedicated storage room. Such rooms may enhance the efficiency of laboratory operations and should be considered if space considerations allow. Consult with EH&S (Environmental Health and Safety) for specific code requirements. Construction and demolition debris and material shall be recycled or reused at a rate consistent with the overall projects country goals (Kimyasal Maddelerle Çalışmalarda Sağlık ve Güvenlik Önlemleri Hakkında Yönetmelik, 2013). Chemical storage rooms should be designed in which an appropriate smoke and fire sensor, flood sensor and automatic fire extinguisher must exist. The fire extinguisher systems should be selected as FM-200, dry powder or CO_2 type, depending on the hazard classification of the usage area.

3.5 Overhead emergency shower, eye washer, fire extinguishers and life safety system

An overhead emergency shower and eye washer equipment should be provided the user with both a full body penetration and located in laboratories where there is the potential for a hazardous material splash to the body. The equipment should also be designed such that the flow of fluids is non-injurious under the varying water pressures.

Fire extinguishers should be placed in external cabinets, which are identifiable, by proper signage. Initial cabinet placement should be located near (within 10 m.) of main entrance doors. Maximum travel distance to any extinguisher must be within 25m. It is necessary to select an extinguisher appropriate to the type of fire likely to occur in that section so that an efficient intervention can be carried out (Binaların Yangından Korunması Hakkında Yönetmelik, 2007). Additionally, an integrated fire alarm, smoke detection and sprinkler alarm system should be provided in laboratories. The system should be a fully addressable distributed processing topology providing alarm and all detectors should be addressable and self-testing.

There are many examples of good applications among the world universities designed according to concept given above.

4. Some Examples of Laboratory Safety in The World Universities

In University of Toledo; for any news construction or renovation of laboratory areas consider health, safety and regulator compliances issues early in the design stage of the project. The outlines some of these issues can be classified as layout, furniture's and fixtures, storage laboratory ventilation, emergency equipment, materials handling, project checklist (University of Toledo, 2016). On the other hand, Columbia University laboratories are designed to comply with applicable federal state and local laws and regulation to facilitate compliance and reporting requirements not limited to the latest edition with respect to OSHA (Occupational Health and Safety Administration) LEED (Leadership in Energy Environmental Design) for labs (Columbia University, 2011). Moreover, In Stanford University, the primary objective in laboratory design is to provide a safe environment for workers laboratory to conduct their work. A secondary objective is to allow for the maximum flexibility for safe research use undergraduate teaching laboratories require other specific design considerations. Therefore, all health and safety hazards must be anticipated and carefully evaluate that protective measures can be incorporated into the design (Stanford University, 2004). In addition, Princeton University goals providing an efficient laboratory safety program assistance to groups planning laboratory renovations, new laboratories and new laboratory buildings. University building standards developed to ensure safe, efficient and sustainable building practices are observed during all new construction and major building renovations (Princeton University, 2016).

5. Conclusions and Recommendations

Research and student laboratories present many challenges. In the day-to-day bustle of conducting research experiments, worker health and safety can be easily overlooked. However, with proper guidance, a trained eye, and practice in noticing the mundane, we can find and correct many common mistakes and prevent illness or injury. Each laboratory that is already exist or will be established in universities, should be structured according to their special intended purpose through detections and suggestions of all person who work in relevant field. In addition, laboratory design should be created by making a prediction work for all risks that may occur. An emergency action plan should be generated by determining accidents and emergencies, and regulations in this plan should be performed.

References

Asumeng M., Asamani L., Afful J. and Agyemang C. 2015, Occupational Safety and Health Issues in Ghana: Strategies For Improving Employee Safety And Health At Workplace,

International Journal of Business and Management Review Vol.3, No.9, pp.60-79.
İleri Ü. 2014, İş Sağlığı ve Güvenliği Önlemleri İle Sosyo-Ekonomik Sonuçları, Efil Yayınevi, Çankaya/Ankara.
6331 Sayılı İş Sağlığı ve Güvenliği Kanunu 2012, Resmi Gazete S.28339.
Binaların Yangından Korunması Hakkında Yönetmelik 2007, Resmi Gazete S. 26735.
Kimyasal Maddelerle Çalışmalarda Sağlık Ve Güvenlik Önlemleri Hakkında Yönetmelik 2013, Resmi Gazete S. 28733.
University of Toledo 2016, Safety and Health Department Laboratory Design Guidelines, http:// www.utoledo.edu / depts/safety/docs/lab_safety/Laboratory%20Design%20Guidelines.pdf (accessed 13 March 2017).
Columbia University 2011, Guidelines for Laboratory Design, http://www.cumc.columbia.edu/facilities-management / sites / default/files/columbia_university_lab_design_guideline.pdf (accessed 13 March 2017).
Stanford University 2004, The Department of Environmental Health and Safety (EH&S), https://ehs.stanford.edu/topic/lab-safety (accessed 13 March 2017).
Princeton University 2016, Environmental Health and Safety Department, https://ehs.princeton.edu/laboratory-and-research-safety (accessed 13 March 2017)

Avrupa Bilim ve Teknoloji Dergisi
Özel Sayı, S. 38-44, Aralık 2017

Konferans Bildirisi

www.ejosat.com ISSN:2148-2683

European Journal of Science and Technology
Special Issue, pp. 38-44, December 2017

Conference Paper

Experimental Investigation of Heat Transfer and Friction Characteristics in L-Footed Spiral Fin-Tube Banks

Erhan KIRTEPE[1*], Necdet ÖZBALTA[2]

[1] Corresponding author: Ege University, Faculty of Engineering, Department of Mechanical Engineering, Bornova, 35100, İzmir, Turkey, erhan.kirtepe@gmail.com
[2] Ege University, Faculty of Engineering, Department of Mechanical Engineering, Bornova, 35100, İzmir, Turkey, necdet.ozbalta1@gmail.com

Abstract

In this experimental study, air side heat transfer and flow characteristics of L-footed spiral fin-and-tube heat exchanger have been analyzed. There were four rows of tubes in the air flow direction and four tubes per row in the heat exchanger. The hot water was flowed through the tubes while the ambient air was flowed cross flow over the tubes. The results were presented as plots of friction factor f and Colburn j factor against Reynolds number. The air-side heat transfer coefficient and pressure drop were also presented against frontal air velocity. Additionally, The correlations for j and f factors were also obtained from the experimental data.

Keywords: L-footed spiral fin, Heat exchanger, Extended surface, Heat transfer

L-Ayaklı Spiral Kanatlı-Boru Demetlerinde Isı Transfer ve Sürtünme Karakteristiklerinin Deneysel İncelenmesi

Öz

Bu deneysel çalışmada, L-ayaklı spiral kanatlı boru tipi bir ısı değiştiricinin hava tarafındaki ısı transferi ve akış özellikleri analiz incelenmiştir. Isı değiştiricide hava akışı yönünde dört sıra boru ve her sıradada dört adet boru vardır. Çevre hava borular üzerinden çapraz olarak geçerilirken, sıcak su ise boruların içerisinden geçirilmiştir. Sonuçlar, Reynolds sayısına karşı sürtünme faktörü f ve Colburn j faktörünün grafikleri olarak sunulmuştur. Hava tarafındaki ısı taşınım katsayısı ve basınç düşüşünün de hava hızına karşı değişimi gösterilmiştir. Bunlara ek olarak, j ve f faktörlerinin korelasyonları da deneysel verilerden elde edilmiştir.

Anahtar kelimeler: L-ayaklı spiral kanat, Isı değiştirici, Genişletilmiş yüzey, Isı transferi

*Corresponding author : Ege University, Faculty of Engineering, Department of Mechanical Engineering, Bornova, 35100, İzmir, Turkey, erhan.kirtepe@gmail.com, phone: +90 232 311 10 10

1. Introduction

Heat exchangers are widely used in many engineering applications. In heat exchangers, when one of the fluids is a gas which is passed in cross flow over tubes, liquid is passed through the tubes. The dominant thermal resistance in an air cooled heat transfer between the hot and cold fluids is usually seen on the air side. Consequently, usage of finned surface on the air side has been a wide application in terms of improving the total thermal performance of the system. Nuntaphan et al. (2005a and 2005b) have analyzed the air-side performance of crimped spiral fin-and-tube heat exchangers with cross-flow for wet and dry surface conditions. Pongsoi et al. (2011 and 2012a) have experimentally analyzed effect of fin pitches and the air-side performance of the crimped spiral fin-and-tube heat exchangers. Kwaguchi et al. (2006a and 2006b) have analyzed the heat transfer and pressure drop characteristics for forced convection in spiral finned tube bundles and in serrated finned tube bundles. Tang et al. (2009) have experimentally researched the air-side heat transfer and friction characteristics of the heat exchanger in which five different types of fins were used. Pongsoi et al. (2012b and 2013) have analyzed the air-side performance of the L-footed spiral fin-and-tube heat exchanger with multipass parallel and counter cross-flow. Fa Jiang et al. (2012) have experimentally analyzed the heat transfer and flowing resistance characteristics of the cross-flow over spiral fin-and-tube heat exchangers for different fin height, pitch. Ma et al. (2012) have analyzed the influence of the fin density on the thermal hydraulic performance of serrated finned tube heat exchanger. The air-side performance in serrated welded spiral fin tube heat exchangers was experimentally researched for Z-flow type and high Reynolds (Kiatpachai et al., 2015).

2. Experimental Set-Up

Schematic representation of the experimental setup used in the study is shown in Figure 1 (Kırtepe, 2014).

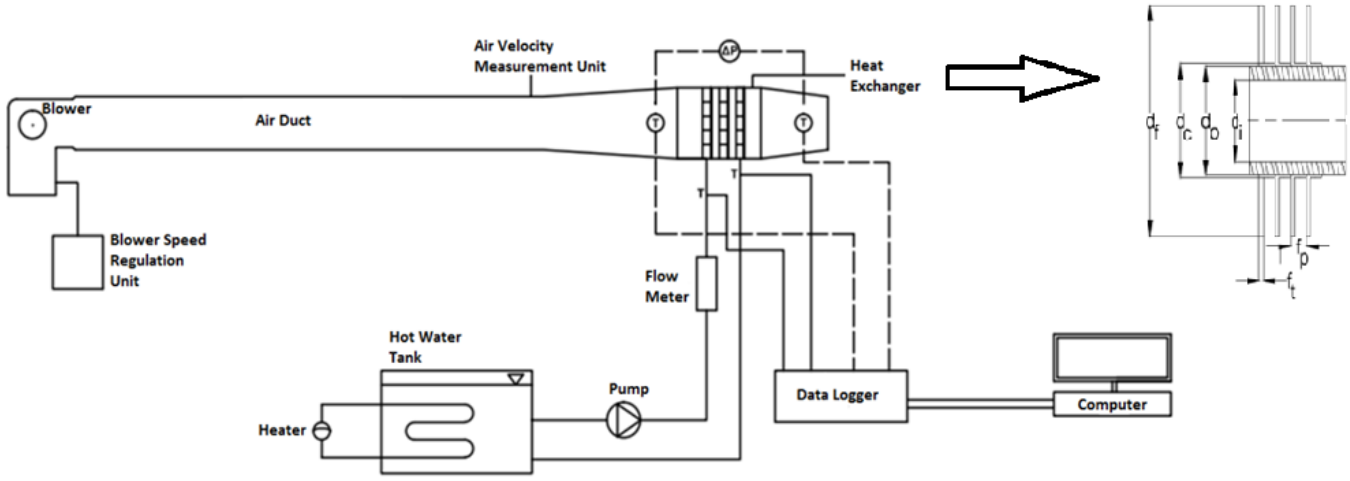

Figure 1. Schematic drawing of the experimental set-up

The experimental set-up consisted of heat exchanger, air duct, blower, blower speed regulation unit, hot water tank, water pump, temperature control system (Proportional Integral Derivative), velocity and temperature measuring devices and data collection unit. The tubes in the heat exchanger were placed as four lines each as shifted rows in both parallel and perpendicular directions to the air flow (Figure 2). The heat exchanger dimensions were 262.5 mm x 400 mm x 262 mm. Tubes were in staggered arrangement in the heat exchanger.

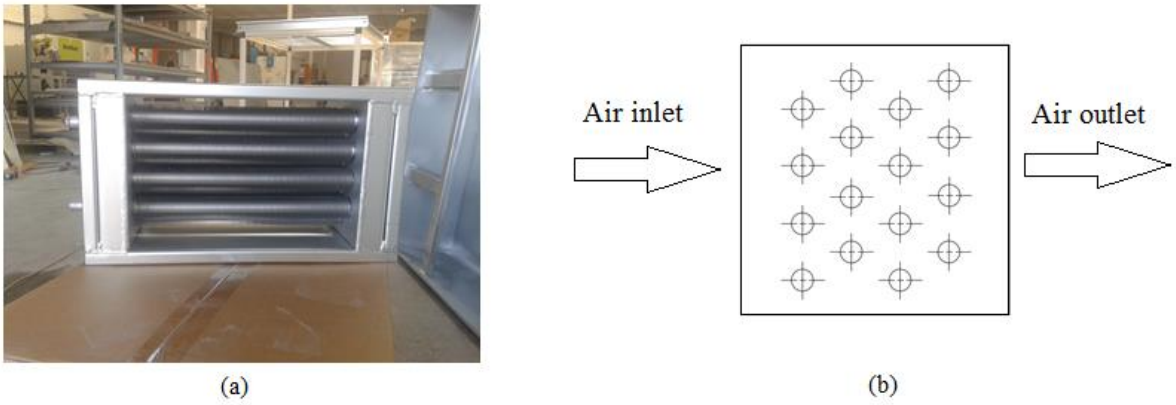

Figure 2. Heat exchanger a) Photo b) Schematic drawing

Table 1. Structure parameters of spiral finned tube

Inner diameter of tube (d_i)	16.1 mm
Outer diameter of tube (d_o)	21.3 mm
Outer diameter of fin collar (d_c)	22.3 mm
Outer diameter of fin (d_f)	45.3 mm
Fin thickness (f_t)	0.5 mm
Fin pitch (f_p)	3.3 mm
Spacing between the tubes which are at cross direction of the tube bundle	55 mm
Diagonal distance between the tubes in the tube bundle	55 mm
Spacing between the tubes which are at axial direction of the tube bundle	47.63 mm

In the experiments, the frontal air velocity of the ambient air passing in cross-flow over the tubes was kept in six different values (0.52, 1.56, 2.56, 3.60, 4.50, 5,44 m/s) while the inlet temperature of the water passing through the pipes was kept in four different values (40, 50, 60, 70 °C) and the flow rate of the water was fixed to 3.83 X 10^{-5} m^3/s.

The frontal air velocity was measured at a point in the heat exchanger before the fluid enters the tube banks. For measuring the frontal air velocity, telescopic air velocity measuring sensor with the operating range between 0 and 10 m/s and between -20 and 70 °C temperature was used. Accuracy of the sensor in terms of temperature and velocity was ±0.5 °C and ±0.03 m/s, respectively. For measuring the pressure drop, differential pressure meter with operating range between 0 and 500 Pascal and with accuracy of ±%2 was used. For measuring the water flow rate, an electromagnetic flow meter with operating range between 0 °C and 80 °C and with accuracy of ±%0.002 was used. J Type thermocouple with operating range between -200 and +800 °C and with accuracy of ±0.5 °C was used for measuring the air temperature. PT-100 with accuracy of ±0.01 °C was used for measuring the water temperature.

3. Material and Method

In this study, *P-NTU* method was used to find out the air side performance of L-footed spiral fin and tube heat exchanger with cross flow.

3.1Temperature Effectiveness – Number of Transfer Units (P-NTU) Method

The heat transfer rate from the hot fluid to the cold fluid in this method is defined below.

$$Q = P_1(\dot{m}c_p)_1\Delta T_{max} = P_2(\dot{m}c_p)_2\Delta T_{max} \quad (1)$$

where P indicates the temperature effectiveness. 1 and 2 indexes on the other hand indicate the fluids (regardless of being hot or cold) (Shah and Sekulic, 2003).

The temperature effectiveness (P_1 and P_2) for every fluid is:

$$P_1 = \frac{T_{1,o}-T_{1,i}}{T_{2,i}-T_{1,i}} = \frac{T_{1,o}-T_{1,i}}{\Delta T_{max}} \quad \text{and} \quad P_2 = \frac{T_{2,i}-T_{2,o}}{T_{2,i}-T_{1,i}} = \frac{T_{2,i}-T_{2,o}}{\Delta T_{max}} \quad (2)$$

The numbers of transfer units (NTU_1 and NTU_2) are:

$$NTU_1 = \frac{UA}{(\dot{m}_1C_{p1})} = \frac{UA}{C_1} \quad \text{and} \quad NTU_2 = \frac{UA}{(\dot{m}_2C_{p2})} = \frac{UA}{C_2} \quad (3)$$

The heat capacity rate ratio (R_1 and R_2) is defined as:

$$R_1 = \frac{\dot{m}_1C_{p1}}{\dot{m}_2C_{p2}} = \frac{C_1}{C_2} \text{ and } \quad R_2 = \frac{\dot{m}_2C_{p2}}{\dot{m}_1C_{p1}} = \frac{C_2}{C_1} \quad (4)$$

The temperature effectiveness, P, is a function of *NTU*, *R* and flow arrangement. In the crossflow heat exchanger in which fluid 1 is mixed while fluid 2 is unmixed, the temperature effectiveness (P_1) and the number of transfer unit (NTU_1) of the fluid 1 are given below (Shah and Sekulic, 2003).

$$P_1 = 1 - exp\left[-\frac{1-\exp(-R_1NTU_1)}{R_1}\right] \quad (5)$$

$$NTU_1 = \frac{1}{R_1}\ln\left[\frac{1}{1+R_1\ln(1-P_1)}\right] \quad (6)$$

3.2 Calculation of the Heat Transfer Coefficient

The heat transfer rates are calculated for both air-side and water-side as follows:

$$Q_a = \dot{m}_a c_{P,a}\Delta T_a \quad \text{and} \quad Q_w = \dot{m}_w c_{P,w}\Delta T_w \quad (7)$$

The total rate of heat transfer used in performance calculations is the average of the heat transfer rate of air-side and water-side. Air-side heat transfer coefficient h_i is found with the below mentioned equation through the usage of equations 2, 3, 5 and 6.

$$\frac{1}{U_oA_o} = \frac{1}{h_iA_i} + \frac{\ln(d_o/d_i)}{2\pi k_tL} + \frac{\ln(d_c/d_o)}{2\pi k_fL} + \frac{1}{\eta_o h_o A_o} \quad (8)$$

The water-side heat transfer coefficient h_o is calculated with the formula suggested by Sieder and Tate (Kraus et al., 2001)

$$h_i = \frac{k_s}{d_i}1{,}86\left(\frac{Re_iPr_sd_i}{L}\right)^{1/3}\left(\frac{\mu}{\mu_y}\right)^{0{,}14} \quad (9)$$

The overall surface efficiency is:

$$\eta_o = 1 - \frac{A_f}{A_o}(1-\eta) \quad (10)$$

where $A_o = A_b + A_f$ and A_o indicates the total surface area of the finned tube whereas A_b= unfinned heat transfer area and A_f= finned heat transfer area. Unfinned and finned heat transfer areas are obtained with the below presented equation (Pongsoi et al., 2012b):

$$A_b = N_TN_L\left[\pi d_cL - \left(\sqrt{f_p^2 + (\pi d_c)^2}\right) \times f_t\left(\frac{L}{f_p}\right)\right] \quad (11)$$

$$A_f = N_TN_L\left(\frac{L}{f_p}\right)\left[0.5\pi d_f^2 - 0.5\pi d_c^2 + \pi d_f f_t\right] \quad (12)$$

Fin efficiency was found with the formula suggested by Gardner (Pongsoi et al., 2012b; Kraus et al., 2001).

$$\eta = \frac{2\psi}{\phi(1+\psi)}\frac{I_1(\phi R_f)K_1(\phi R_o) - I_1(\phi R_o)K_1(\phi R_f)}{I_0(\phi R_o)K_1(\phi R_f) + I_1(\phi R_f)K_0(\phi R_o)} \quad (13)$$

where, ϕ parameter is defined below:

$$\phi = \left(r_f - r_o\right)^{3/2}\left(\frac{2h_o}{k_fA_p}\right)^{1/2} \quad (14)$$

where A_p is the profile area of fin:

$$A_p = f_t(r_f - r_o) \quad (15)$$

$R_f = 1/(1-\psi)$, $R_o = \psi/(1-\psi)$ functions are defined with the usage of ratio of the diameters $\psi = d_o/d_f$.

The air-side heat transfer coefficient (h_o) was calculated with the above mentioned equations.

The air-side heat transfer characteristics of the L-footed spiral fin-and-tube heat exchanger were explained on the basis of Colburn-j factor (Nuntaphan et al., 2005a; Kiatpachai et al., 2015; Wang et al., 1996).

$$j = St\,Pr^{2/3} = \frac{h_o}{\rho_a V_{a,max} c_{P_a}}Pr^{2/3} \quad (16)$$

Flow characteristics given in Fanning friction factor are obtained from the equation suggested by Kays and London. In this equation, inlet and outlet pressure losses are considered as well

(Nuntaphan et al., 2005a; Kiatpachai et al., 2015; Wang et al., 1996).

$$f = \frac{A_{min}}{A_o}\left(\frac{\rho_m}{\rho_i}\right)\left[\frac{2\ \Delta P\ \rho_i}{G_c^2} - (1 + \sigma^2)\left(\frac{\rho_i}{\rho_o} - 1\right)\right] \quad (17)$$

where, σ is the ratio of minimum free flow area to the frontal area, A_{min} is the minimum free flow area, A_o is the total heat transfer area and G_c is the mass velocity.

$$G_c\ (kg/sm^2) = \frac{\dot{m}\ (kg/s)}{A_c\ (m^2)} = \frac{\rho U_\infty A_{fr}}{A_c} \quad (18)$$

where, $\dot{m}$ is the mass flow rate (kg/s), U_∞ is the frontal air velocity (m/s), A_{fr} is the frontal area (m^2). U_∞ was measured, G_c was calculated.

Because of the variation of the air side temperature is low, so inlet and outlet effects are ignored, namely when considered as $\rho_i=\rho_o$ and $\rho_m=(\rho_i+\rho_o)/2$, Fanning friction factor can be obtained as presented below:

$$f = \frac{A_{min}\rho_m}{A_o}\left[\frac{2\Delta P}{G_c{}^2}\right] \quad (19)$$

4. Results and Discussion

Figure 3 shows the variation of the air side heat transfer coefficient with the frontal air velocity for the different water inlet temperatures. Figure 4 shows the variation of the pressured drop with the frontal air velocity. The air-side heat transfer coefficient rapidly increases with the frontal air velocity. It is observed that water inlet temperature does not have a significantly effect on the air-side heat transfer coefficient. As the frontal air velocity increases, the pressure drop occurring at the air-side of the heat exchanger also increases.

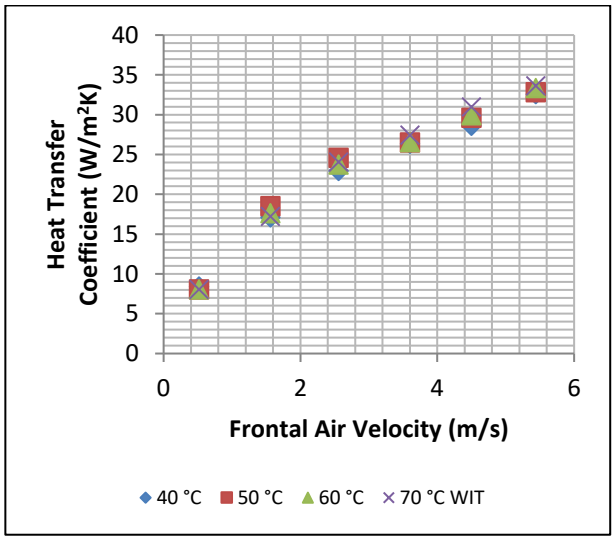

Figure 3. Variation of the air side heat transfer coefficient with the frontal air velocity for different water inlet temperatures (WIT)

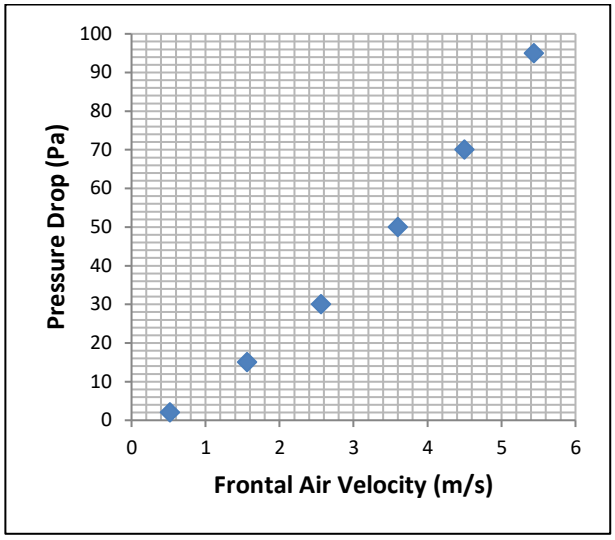

Figure 4. Variation of the pressure drop with the frontal air velocity

The basic surface characteristics of the heat exchangers are generally presented in a dimensionless form as Colburn *j* factor and Fanning friction factor *f*. In Figure 5, changes in Colburn *j* factor and Fanning friction factor *f* with the Reynolds number based on the outer diameter of fin collar can be seen. As the Reynolds number increases, both Colburn *j* factor and Fanning friction factor *f* decrease.

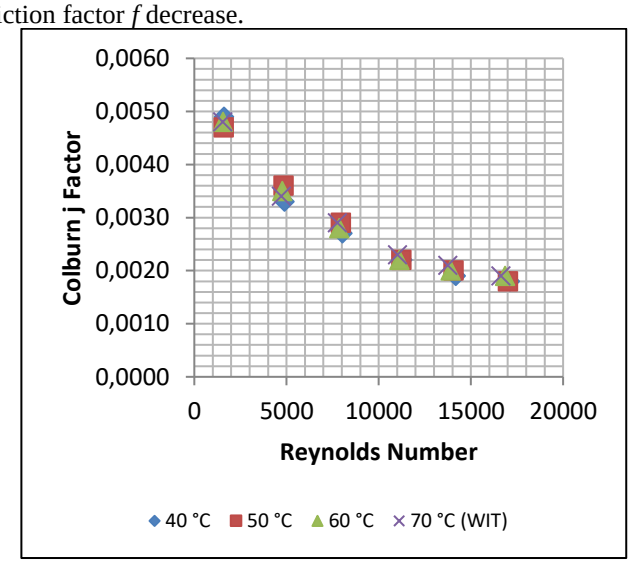

Figure 5a. Variation of Colburn *j* factor with Reynolds number for different water inlet temperatures

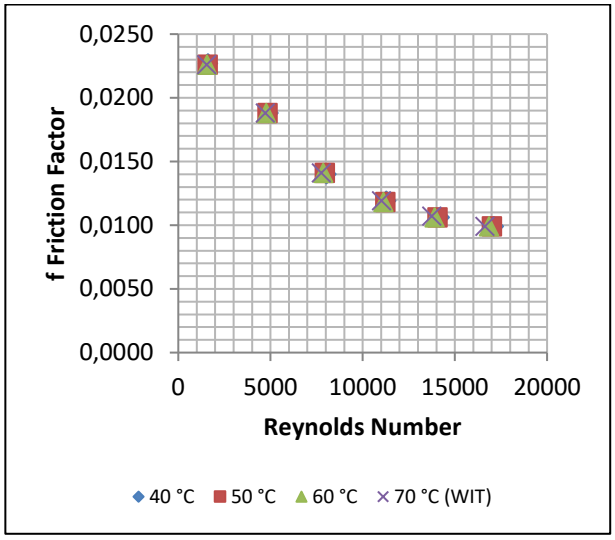

Figure 5b. Variation of *f* Fanning friction factor with Reynolds number for different water inlet temperatures

Colburn *j* factor and Fanning friction factor *f* were obtained with the usage of experimental data and depending upon air-side Reynolds Number as $j = aRe^{b}$ve $f = mRe^{n}$ form. Here; *a*, *b*, *m* and *n* were obtained from the experimental data. Formulas suggested for heat transfer performance and friction performance are presented below:

$j = 0.08287Re^{-0,3838}$ ve $f = 0.2684Re^{-0,3307}$ (20)

$$MeanDeviation = \frac{1}{n}\left(\sum_{1}^{n}\frac{\left|\varphi_{corr} - \varphi_{\exp}\right|}{\varphi_{\exp}}\right)\times 100\% \quad (21)$$

The correlation coefficient was one of the primary criterion for selecting the best equation. In addition to the correlation coefficient, the various statistical parameters such as; mean bias error (MBE), root mean square error (RMSE) were used to determine the quality of the fit.

$$CC = \frac{\sum_{i=1}^{N}(y_i-\bar{y})(x_i-\bar{x})}{\sqrt{[\sum_{i=1}^{N}(y_i-\bar{y})^2][\sum_{i=1}^{N}(x_i-\bar{x})^2]}} \quad (22)$$

Ideally CC should be 1.

$$MBE = \sum_{i=1}^{N}(y_i - x_i)/N \quad (23)$$

Ideally a zero value of MBE should be obtained.

$$RMSE = \sqrt{\sum_{i=1}^{N}(y_i - x_i)^2/N} \quad (24)$$

Ideally a zero value of RMSE should be obtained.

For a model to be good estimator, the mean values of all the errors terms MBE, RMSE should be small. In this study, the statistical tests results were computed as CC=0.965, MBE=2.9x10^{-5}, RMSE= 1.22x10^{-3} for friction factor, CC=0.986, MBE=4.51x10^{-6}, RMSE= 1.73x10^{-4} for Colburn factor.

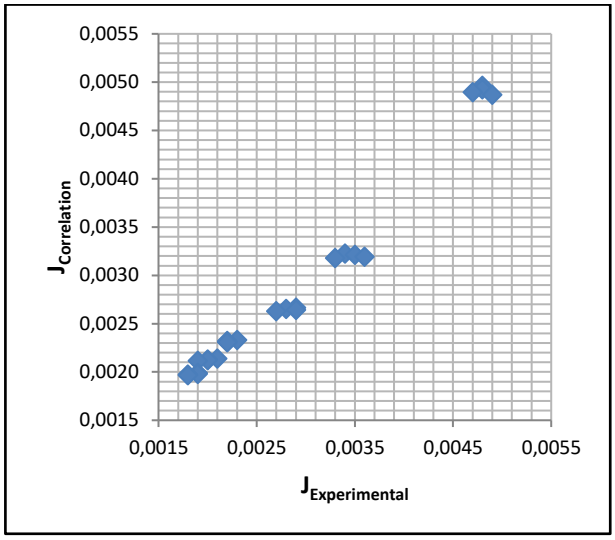

(a)

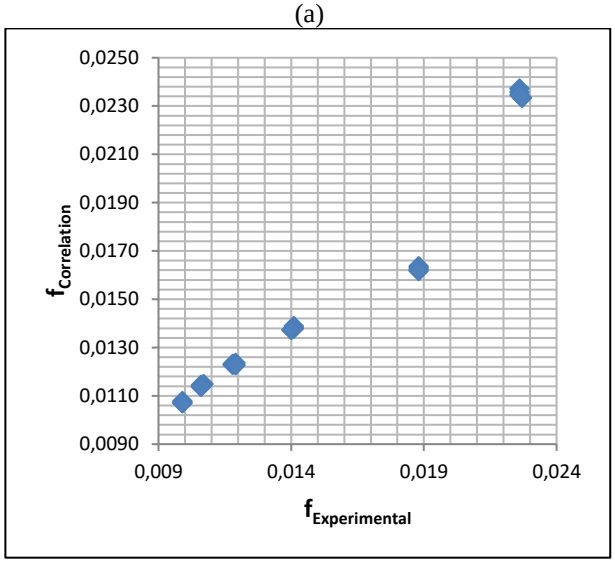

(b)

Figure 6. Comparison of the proposed correlations with the experimental data a) Colburn factor b) Fanning friction factor

In Figure 6, the comparison between the proposed correlations with the experimental data is seen. Mean deviation values of the proposed correlations for Colburn *j* factor and Fanning friction factor *f* were found as 5.58% and 6.53%, respectively. Comparison between the proposed correlations for Colburn *j* factor and Fanning friction factor *f* in the literature and the formula developed through the usage of experimental data can be seen in Figure 7. The formula suggested for both Colburn *j* factor and Fanning friction factor *f* at high Reynolds Numbers and the proposed correlations for other fin types present similar changes. It was found that serrated welded spiral fin-tube banks gave a higher Colburn *j* factor and *f*-friction factor than other fin types. But, it will cause higher pressure drop.

It was found that serrated welded spiral fin gave a higher (77.9%) Colburn *j* factor than the L-footed spiral fin, but the L-footed spiral fin gave a lower (90.5%) *f*-friction factor than the serrated welded spiral fin.

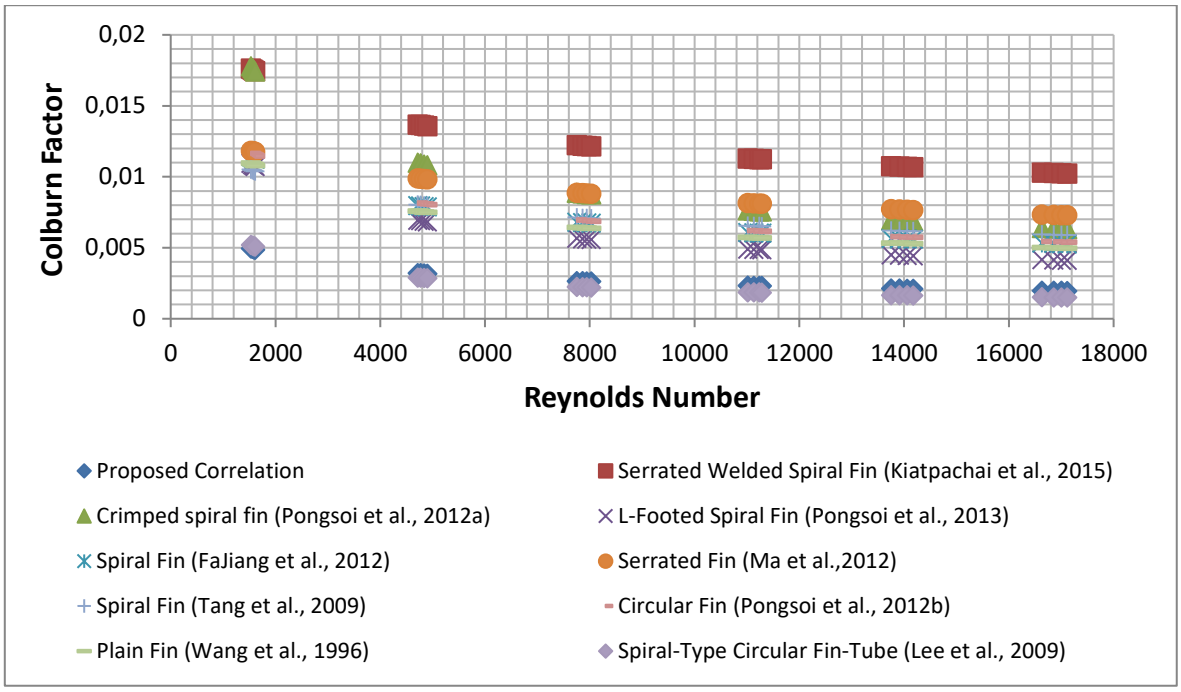

(a)

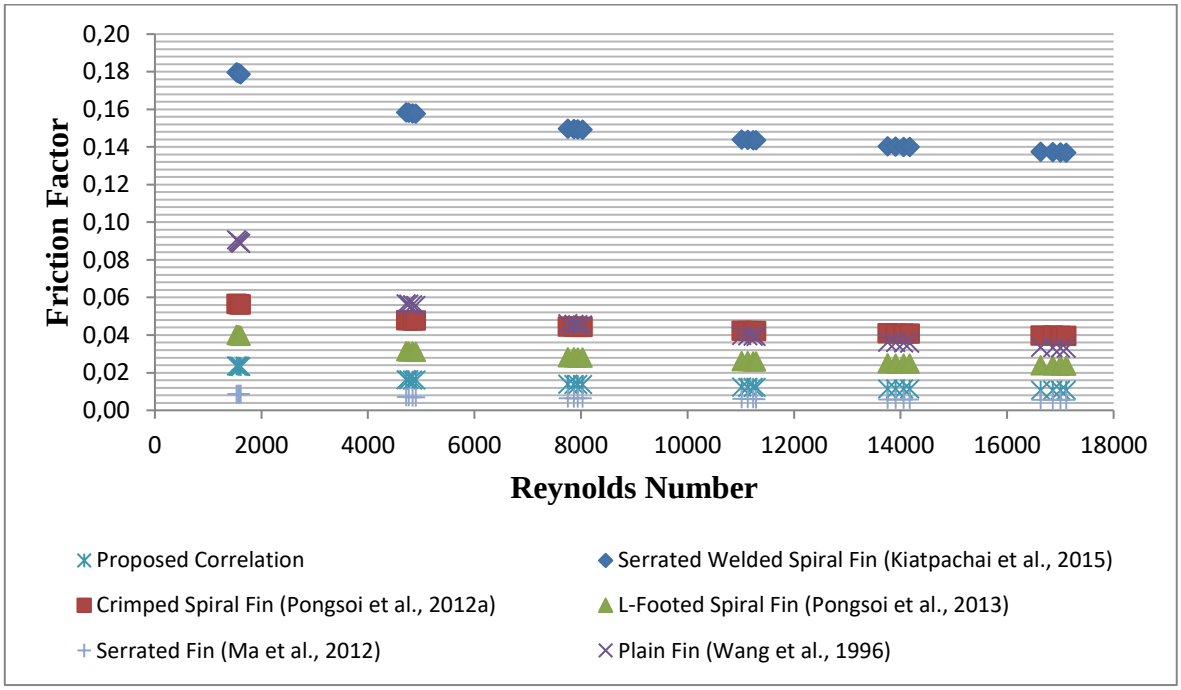

(b)

Figure 7. Comparison of the proposed correlations with the correlations of several fin types a) Colburn factor b) Fanning friction factor

5.Conclusions

In this study, the heat transfer and flow characteristics of the air-side of the L-foot spiral fin-and-tube heat exchanger were analyzed at high Reynolds Number (1500-17500) determined according to the outside diameter of the fin collar. Through the experimental data, mean deviation values of the formulas derived for Colburn *j* factor and Fanning friction factor *f* were found as 5.58% and 6.53%, respectively.

References

FaJiang H., WeiWu C., Ping Y. 2012. Experimental investigation of heat transfer and flowing resistance for air flow cross over spiral finned tube heat exchanger. Energy Procedia 17, 741-749.

Kawaguchi K., Okui K., Asai T., Hasegawa Y. 2006a. The Heat Transfer and Pressure Drop Characteristics of the Finned Tube Banks in Forced Convection (Effects of Fin Height on Heat Transfer Characteristics). Heat Transfer-Asian Research 35, 194-208.

Kawaguchi K., Okui K., Asai T., Hasegawa Y. 2006b. The Heat Transfer and Pressure Drop Characteristics of Finned Tube Banks in Forced Convection (Effects of Fin Height on Pressure Drop Characteristics). Heat Transfer-Asian Research 35, 179-193.

Kırtepe E. 2014. Kanatli Dairesel Borularda Isı Transfer Etkinliğinin İncelenmesi. Ege Üniversitesi, Fen Bilimleri Enstitüsü, 111p, (In Turkish).

Kiatpachai P., Pikulkajorn S., Wongwises S. 2015. Air-side performance of serrated welded spiral fin-and-tube heat exchangers. International Journal of Heat and Mass Transfer 89, 724-732.

Kraus A.D., Aziz A., Welty J. 2001. Extended Surface Heat Transfer. John Wiley & Sons, New York.

Lee M., Taehyung K., Kim Y. 2009. Air-side heat transfer characteristics of spiral-type circular fin-tube heat exchangers. International Journal of Refrigeration 33, 313-320.

Ma Y., Yuan Y., Liu Y., Hu X., Huang Y. 2012. Experimental investigation of heat transfer and pressure drop in serrated finned tube banks with staggered layouts. Applied Thermal Engineering 37, 314-323.

Nuntaphan A., Kiatsiriroat T., Wang C.C. 2005a. Air side performance at low Reynolds number of cross-flow heat exchanger using crimped spiral fins. International Communications in Heat and Mass Transfer 32, 151-165.

Nuntaphan A., Kiatsiriroat T., Wang C.C. 2005b. Heat transfer and friction characteristics of crimped spiral finned heat exchangers with dehumidification. Applied Thermal Engineering 25, 327-340.

Pongsoi P., Pikulkajorn S., Wang C.C., Wongwises S. 2011. Effect of fin pitches on the air-side performance of crimped spiral fin-and-tube heat exchangers with a multipass parallel and counter cross-flow configuration. International Journal of Heat and Mass Transfer 54, 2234-2240.

Pongsoi P., Pikulkajorn S., Wang C.C., Wongwises S. 2012a. Effect of number of tube rows on the air-side performance of crimped spiral fin-and-tube heat exchanger with a multipass parallel and counter cross-flow configuration. International Journal of Heat and Mass Transfer 55, 1403-1411.

Pongsoi P., Pikulkajorn S., Wongwises S. 2012b. Experimental study on the air-side performance of a multipass parallel and counter cross-flow L-footed spiral fin-and-tube heat exchanger. Heat Transfer Engineering 33, 1251-1263.

Pongsoi P., Promoppatum P., Pikulkajorn S., Wongwises S. 2013. Effect of fin pitches on the air-side performance of L-footed spiral fin-and-tube heat exchangers. International Journal of Heat and Mass Transfer 59, 75-82.

Shah R.K., and Sekulic D.P. 2003. Fundamentals of Heat Exchanger Design. John Wiley & Sons, Canada.

Tang L.H., Zeng M., Wang Q.W. 2009. Experimental and numerical investigation on air-side performance of fin-and-tube heat exchangers with various fin patterns. Experimental Thermal and Fluid Science 33, 818-827.

Wang C.C., Chang Y.J., Hsieh Y.C., Lin Y.T. 1996. Sensible Heat and Friction Characteristics of Plate Fin and-Tube Heat Exchangers Having Plane Fins. International Journal of Refrigeration 19, 223–230.

Avrupa Bilim ve Teknoloji Dergisi
Özel Sayı, S. 45-47, Aralık 2017

Konferans Bildirisi

www.ejosat.com ISSN:2148-2683

European Journal of Science and Technology
Special Issue, pp. 45-47, December 2017

Conference Paper

Pv Powered Electronic Circuits Designed to Decrease Road Accidents

Ahmet SENPINAR

College of Technical Sciences, Department of Electronics Technology, Firat University,Elazig, Turkey, asenpinar@gmail.com

Abstract

One way of the utilizing solar energy is to use pv panel which generates electricity energy as expose to the solar radiation on it. Pv panels are utilized[1] in many areas such as lighting and stand-alone systems, the grid connected systems, pv power plants, satellite, space, communications..etc. Especially in today's green areas and parks, they are used for lighting and irrigation. The usage of pv panels on the roads is a different usage aim of renewable energy sources. Some of them in highways are as follows: the lighting on motorways, traffic signaling, routing sheets, bridges and viaducts lighting, the needed energy of petrol stations, the charger unit of hybrid vehicles, and the determination of car numbers on the road. An electronic circuit design can be placed onto the highways. With the help of electronic sensors in electronics circuit placed on the road is to aim for reducing traffic accidents. It was particularly sharp bend and the angle where very tight, sending a place of warning signal in the lane against the emergence or ramp into the corner with the help of designing electronic circuits on the road if you have a vehicle coming in the opposite direction to help the driver. As a result, it prevents damage to that or give incorrect overtaking a vehicle enters the opposite direction.

Keywords: Renewable energy, road accidents, sensors.

* Corresponding author : College of Technical Sciences, Firat University, Elazig, Turkey, asenpinar@gmail.com, phone: +90 424 237 00 00

1. Introduction

Solar energy has the advantages of being renewable, continuous and environmentally-friendly. Solar panels have a wide panel of use in buildings, factories, roads, car parks, grid dependent and independent pv (photovoltaic) systems, pv stations, satellites, communications systems and hotels, among others (Chambouleyron, 1996, EIE, 2016, Green et al., 2001, Kuwano, 1998). Solar panels are also used at the present time for illuminating green spaces and parks as well as small scale irrigation projects. They can also help to meet the energy needs of resort hotels over summer months by helping with outdoor and ambient lighting. Pv panels are also used to meet the electricity needs of remote settlements. There are many accidents on different roads due to different reasons (Hobbs et al., 1996, Ansari et al., 2000, Elvik et al., 2004, Valent et al., 2002, Kumar et al., 2008, Entezami et al., 2015, WHO, 2015, Taravatmanesh et al., 2015). Some of the accidents on highways consist of faulty overtaking process. Most road accidents result in injuries and fatalities. In the present study, the aim was to design a prototype electronic circuit powered by a pv panel in order to alert drivers about oncoming reckless overtaking in undivided highways (single carriageways) and prevent accidents.

2. System Design

For the electronic circuit designed to reduce accidents on roads is utilizing from solar energy. One of the using methods of solar energy as electricity is to use pv cells generating electrical energy as a result of the solar radiation incident on it. Current generated by pv cell is proportional with effect of solar radiation on cell. The amount of power obtained from pv cell is low because the amount of current and voltage obtained from only a single pv cell is also low. Therefore, in order to obtain the adequate output power, pv cells are connected in series to form a pv module. If higher voltages or currents than are available from a single module are required, modules must be connected into panels (Messenger, 2000, Beckman and Duffie, 1991). A novel and advantageous use of solar panels involves highways. Panels are used today for traffic signaling, road signs, illuminating bridges and viaducts, hybrid vehicle charge units, supplying electrical energy in petrol stations, and illuminating highways and their surrounds (Xing et al., 2005, Hsieh, 2004, Sazanov et al., 2009). The electronic circuit designed for this study has 5 basic parts: the pv panel, sensors, battery and charge unit, alert lamp and electronic control circuit. If Ac load is needed, an additional inverter may also be used.

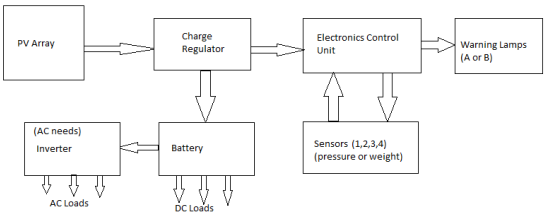

Figure 1. The block schema of the designed pv system

The block diagram of the designed pv powered electronic circuit is shown in Figure 1. The operating principle of the electronic circuit is based on electronic signals received from sensors installed in highways. The circuit aims to decrease accidents resulting from reckless overtaking in sharp bends and ramps particularly in undivided highways, where the range of visibility is strictly limited. The electronic control unit energizes the warning lamp according to the information received from the sensors. In these sections of highways, reckless and careless drivers may cause life-threatening risks for oncoming traffic day and night. In such cases, drivers are alerted to the danger with a lamp on the electronic circuit and are given an opportunity to stop, and potentially dangerous accidents are prevented.

3. Experimental Study and Results

The pv powered electronic system designed for the study is an automatic one that depends on sensors. Two sensors are needed if the circuit is to be used in one single direction in undivided highways, and 4 are needed if it is to be used in both directions. To begin with, the pv panel is connected to the battery over the charge unit. This enables the pv panel to both operate the electronic system and charge the battery during daytime. Later, at night, the battery meets the power need of the electronic system. The circuit works in the following way:

(a)

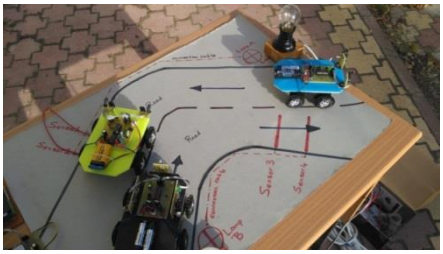

(b)

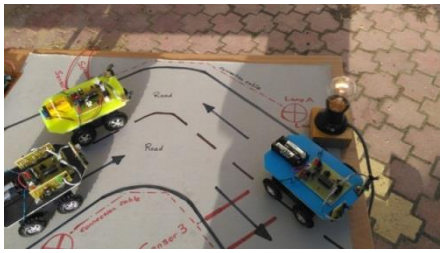

(c)

Figure 2. (a-c). Overview of the experimental system and the first direction of cars

The vehicles in Figure 2 are driving in an undivided highway under normal conditions. The yellow car starts to overtake the black car inappropriately, which sends a signal to the electronic control circuit via sensors. The electronic circuit energizes lamp A, which is installed further forward from the yellow car. Consequently, the driver of the oncoming blue car in its right lane sees lamp A and stops in time to prevent a collision. Thus, a potential accident resulting from reckless overtaking on an undivided highway may be prevented. Similarly, in the opposite direction, the yellow car in Figure 3.(a-b) may try to overtake the blue car inappropriately. The sensors send an alert signal to the

electronic control circuit, which then energizes lamp B for the driver of the black car in its right lane. Upon seeing that lamp B has come on, the driver can stop and prevent a collision.

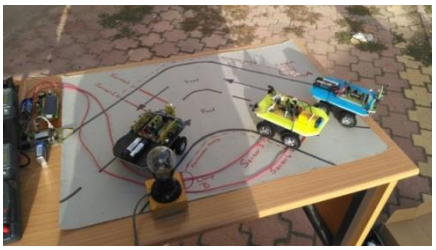

(a)

(b)

Figure 3. (a-b) The opposite direction of cars

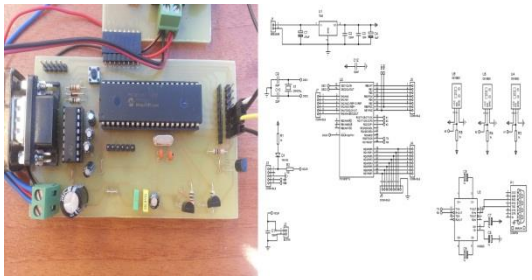

Figure 4. The electronics circuit

The electronics control circuit (Figure 4) designed here is powered by a pv panel. The energy consumption needed for this circuit and its sensors is approximately between 5-10 watts. If led light technology is used for the alert lamps, the energy need is then between 3-5 watts. In this case, the total power needed is approximately 10-15 watts. As the system developed here as a prototype in laboratory conditions is simple, small and powerful, it is also economical. In the trial run, the energy needed for the system was supplied by the 42-watt panel available in the laboratory.

4. Conclusion

The negative environmental effects of conventional energy sources make renewable energy a more important solution each passing day. Using renewable energy on highways may reduce the number of accidents resulting in injuries and casualties. In other words, with a simple, feasible and inexpensive pv powered electronic circuit in prototype, accidents resulting from reckless overtaking may be largely prevented. It is estimated that such a system would significantly reduce the number of accidents in undivided highways and bring moral and material support to both drivers and the country. Overall, the laboratory results of the designed electronic system were satisfactory.

References

Ansari, S., Akhdar, F., Mandoorah, M., & Moutaery, K. 2000. Causes and effects of road traffic accidents in Saudi Arabia. Public health, 114(1), 37-39.

Beckman, William A., Duffie, John A. 1991. Solar Engineering of Thermal Processes, 2nd ed., A Wiley-Interscience Publication, Canada, John Wiley and Sons, Inc.

Chambouleyron,I. Photovoltaics in the developing World. 1996. Elsevier, Energy, Vol.21, No.5, 385-394. DOI:10.1016/0360-5442(95)00118-2.

Elvik, R., Christensen, P., & Amundsen, A. 2004. Speed and road accidents. An evaluation of the Power Model. TØI report, 740.

Entezami, N., Hashemi-Nazari, S. S., Soori, H., Khosravi, A., & Ghadirzadeh, M. R. 2015. Epidemiology of fatal road traffic accidents in Northern provinces of Iran during 2009 to 2010. Safety Promotion and Injury Prevention, 3(1), 1-8.

General Directorate of Electrical Power Resources Survey and Development Administration (EIE). 2016. Turkey (http://www.eie.gov.tr/turkce/YEK/gunes/eiegunes.html).

Green, J.M., Wilson, M., Cawood, W. 2001. Maphephethe rural electrification (photovoltaic) programme: the constraints on the adoption of solar home systems, Development Southern Africa, Vol:18, No.1, 19-30. DOI: 10.1080/03768350123295.

Hobbs, M., Mayou, R., Harrison, B., & Worlock, P. 1996. A randomised controlled trial of psychological debriefing for victims of road traffic accidents. Bmj, 313(7070), 1438-1439.

Hsieh, T. T. 2004. Using sensor networks for highway and traffic applications. IEEE Potentials, 23(2), 13-16.

Kumar, A., Lalwani, S., Agrawal, D., Rautji, R., & Dogra, T. D. 2008. Fatal road traffic accidents and their relationship with head injuries: An epidemiological survey of five years. The Indian Journal of Neurotrauma, 5(2), 63-67.

Kuwano Yukinori. 1998. Progress of photovoltaic system for houses and buildings in Japan, Elsevier, Renewable Energy 15, 535-540. DOI: 10.1016/S0960-1481(98)00220-1.

Messenger, Roger, Ventre, Jerry. 2000. Photovoltaic Systems Engineering, Florida, Crc Pres Llc.

Sazonov, E., Li, H., Curry, D., & Pillay, P. 2009. Self-powered sensors for monitoring of highway bridges. IEEE Sensors Journal, 9(11), 1422-1429.

Taravatmanesh, S., Hashemi-Nazari, S. S., Ghadirzadeh, M. R., & Taravatmanesh, L. 2015. Epidemiology of fatal traffic injuries in the Sistan and Baluchistan province in 2011. Safety Promotion and Injury Prevention, 3(3), 161-168.

Valent, F., Schiava, F., Savonitto, C., Gallo, T., Brusaferro, S., & Barbone, F. 2002. Risk factors for fatal road traffic accidents in Udine, Italy. Accident Analysis & Prevention, 34(1), 71-84.

World Health Organization (WHO). 2015. Global status report on road safety 2015. World Health Organization.

Xing, K., Ding, M., Cheng, X., & Rotenstreich, S. 2005. Safety warning based on highway sensor networks. In Wireless Communications and Networking Conference, 2005 IEEE (Vol. 4, pp. 2355-2361). IEEE.

Avrupa Bilim ve Teknoloji Dergisi
Özel Sayı, S. 48-51, Aralık 2017

Konferans Bildirisi

www.ejosat.com ISSN:2148-2683

European Journal of Science and Technology
Special Issue, pp. 48-51, December 2017

Conference Paper

Investigation of Mechanical Properties of Butt Joint Form in CMT-Brazed Joints of DP1000 Steel Plates Using Different Current Intensity[#]

İbrahim Acar[1*], Veli Şıkşık[1], Faruk Varol[1] , Salim Aslanlar[2]

[1] Vocational School of Karasu, Sakarya University, Karasu, Sakarya, Turkey
[2] Department of Metallurgical and Materials Engineering, Sakarya University, Sakarya, Turkey
Email: ibrahimacar@sakarya.edu.tr

(First received 30 November 2016 and accepted in 30 April 2017)
[#] Presented in "3rd International Conference on Computational and Experimental Science and Engineering (ICCESEN-2016)"

Abstract

In this study, DP 1000 (Dual Phase) steel plates having 1.2 mm thickness were joined by copper-based (CuAl8) wire in CMT-brazing (Cold Metal Transfer) technique. Specimens were prepared in joining forms as butt joint. CMT-Brazing operations were done with nine different CMT-Brazing current intensity of 40, 45, 50, 55, 60, 65, 70, 75 and 80 A. CuAl8 wire composed largely of copper serves as the filler metal were used. Having accomplished the CMT-brazing operations; tensile properties of joints were detected, and micro and macro-structures of joints were investigated in order to see the joinability of DP 1000 steel by CMT-brazing technique.

Keywords: DP1000 Steel, CMT-Brazing, Cold Metal Transfer

1. Introduction

The biggest factor in increasing usage of dual-phase steel DP in the automotive industry can be shown as favorable combinations of high strength and good ductility(Lee, 2015). DP steels, consisting of hard martensite islands in a continuous soft ferrite matrix (Jia, 2016). These two phases are high strength martensite and ferrite provide good elongation. So lightness, high strength and good formability properties of the automotive industry are provided by DP steels (Wang, 2016). In addition, methods of joining DP sheets are also important. There is a lot of work on this subject. Farabi (2011) DP600 and DP980, Wang (2016) DP1000 and Ma (2014), Xu (2012) DP980 sheets by laser welding, investigating their microstructure and mechanical properties. Ozsarac and Aslanlar studied the resistance spot welding of galvanized steels in automotive applications. In present paper, CMT process of DP1000 steels emphasis on the microstructure and strengthening behavior and mechanisms of the joint.

2. Experimental Studies

2.1 Materials

DP1000 steel plates was used in this study. In the tests DP1000 steel plates were 1.2 mm thickness. Steel plates were cut 200x200x1.2 mm. The sheets were positioned end to end to allow gaps between them 0.5 mm, and were subjected to joining by CMT-brazing process. The filler metal was a solid wire with a diameter of 1 mm, classified as AWS ER CuAl8, which is a copper-based, torch angle of 90°. Argon was used as the shielding gas at a flow rate of 12 L/min.

2.2 Methods and procedure

The surface of the samples was cleaned by acetone before CMT-brazing operations. The current values for CMT-brazing operation were determined as 40, 45, 50, 55, 60, 65, 70, 75 and 80 A in butt joint. Nine sets of welding parameters of different heat inputs were selected, as shown in Table 1. The heat input, HI is calculated using the Eq. (1) and (2) below.

$$HI_{linear} = \frac{(60 \times UI)\eta}{V} \quad (1)$$

$$HI_{normalized} = \frac{HI_{linear}}{e} \quad (2)$$

Where η_{CMT}: 0.7 is the arc efficiency factor, e: thickness (mm) U and I are the mean values for the arc voltage, respectively for the current intensity and V (cm/min.) is the CMT-brazing speed. CMT-brazing process parameters such as current intensity, voltage, wire feed speed, shielding gas at a flow rate of 12 L/min, brazing travel speed and brazing gap were presented in Table 1. All CMT-brazing tests were performed automatically on a machine with a robot.

3. Experimental Results And Discussion

3.1 Tensile tests

The experiments showed that most of tensile test specimens fractured from the base metal DP1000 steel. 55, 60, 65, 70, 75 and 80 A currents showed that the strength of the joint zone was higher than that of the DP1000 steel zone and the CuAl8 filler zone. It was obvious that the joint zone was strengthened. Moreover DP 1000 steel sheet, having 1.2 mm thickness, got punctured above 85 A. In Table.1 40, 45, 50 A, insufficient wetting occurred as a result of low heat input. Having examined the strength values in Table 1, it was observed that strength increased with the increase of current intensity.

3.2 Microhardness tests

Figure 1 shows the measured microhardness value of the joints for different CMT-brazing current intensity. It was seen that microhardness value was highest at HAZ and the HAZ hardness was higher than that of the copper filler and base material.

3.3 Macro and microstructures

Appearances of Macro and microstructures of the brazing seams for different current intensity are shown in Figure 2. The molten metal wetted the steel better when 80 A current intensity was used, comparing the samples brazed in 75, 80 A at lower heat input to samples brazed in 40, 45, 50, 55, 60, 65, 70 A. It was observed that the number of dendrites increased on the surface of the joint zone. These dendrites' action caused micro iron particles to melt and migrate, and to become distributed throughout the filler metal zone.

4. Conclusion

This work has presented an investigation on the effects of strength of current intensity. The conclusions from this study are given as follows;

- MIG-brazing method provided lower heat input in comparison with other fusion methods.
- The experiments showed that most of tensile test specimens fractured from the base metal DP1000 galvanized steel. In 40, 45, 50 A, insufficient wetting occurred as a result of low heat input. Moreover DP 1000 steel sheet, having 1.2 mm thickness, got punctured above 85 A.
- It was observed that strength decreased with the increase of current intensity. The best strength arose in 80 A current intensity.

Table 1. *experimental results for different current intensity*

Current intensity [A]	Tensile strength [MPa]	Heat input [j/cm]
40	10	676
45	403	767
50	470	860
55	655	962
60	680	1059
65	699	1165
70	705	1265
75	748	1378
80	752	1481

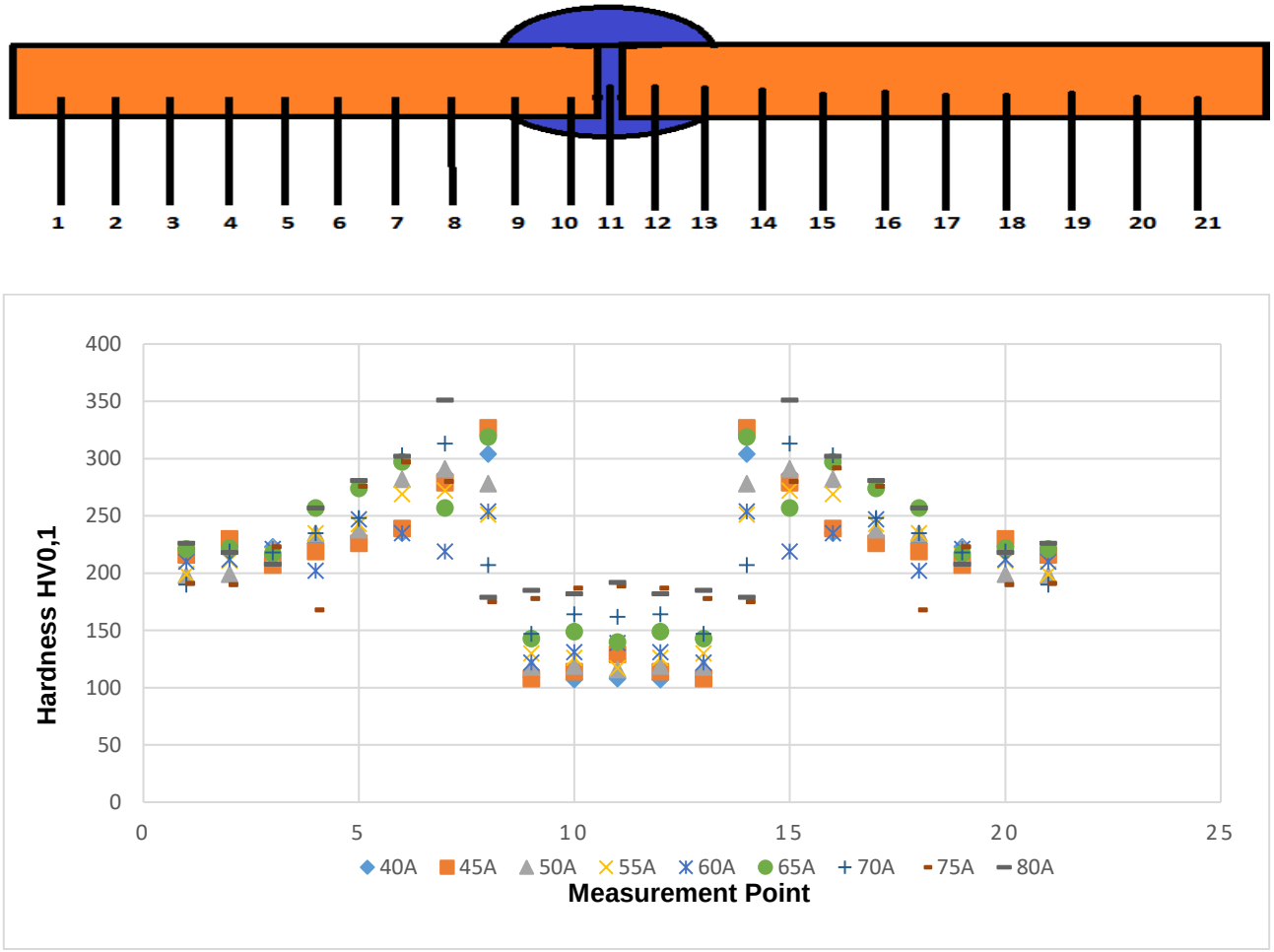

Figure 1. Hardness profile in Heat Affected Zone (HAZ) in DP1000

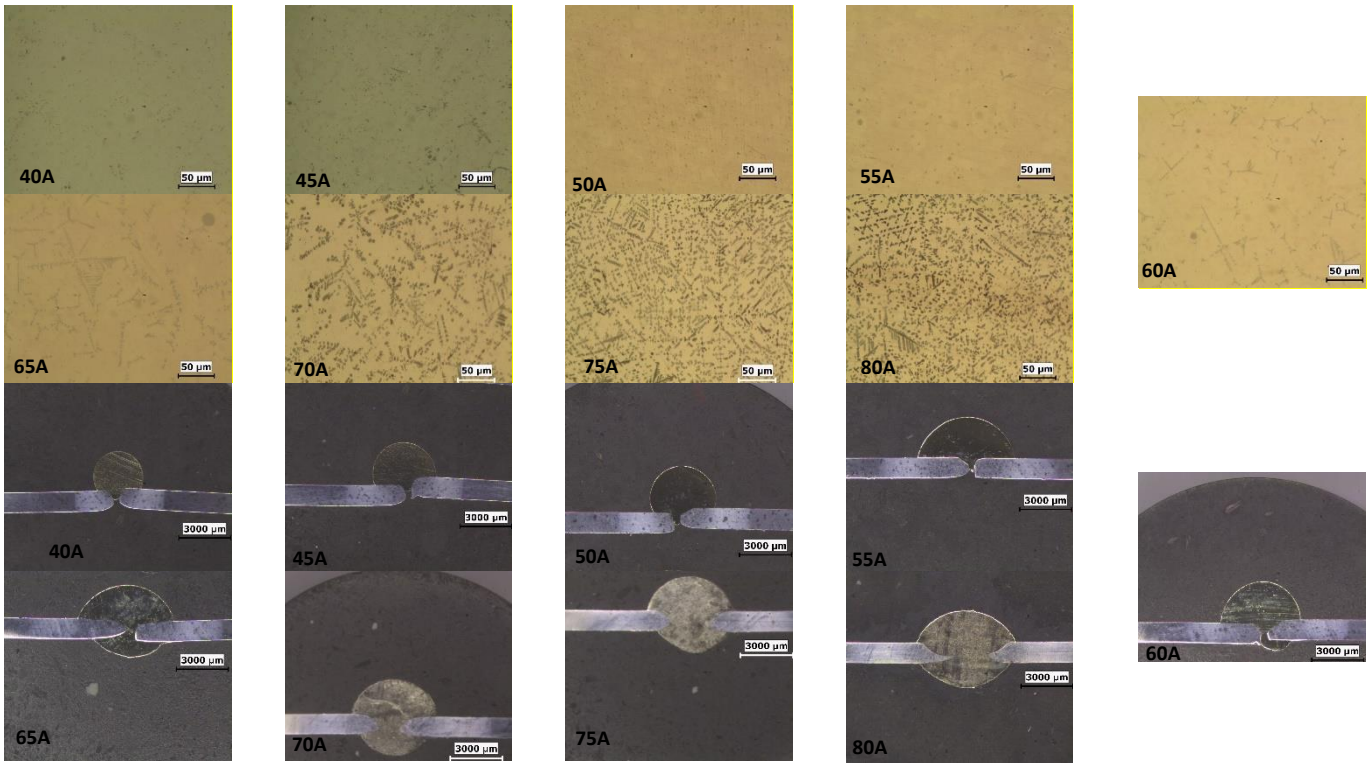

Figure 2. Macro and micro appearanceof the brazing seams for different current intensity

References

Aslanlar S., 2006. The Effect of Nucleus Size on Mechanical Properties in Electrical Resistance Spot Welding of Sheets Used in Automotive Industry. Mater. Des. 27, 125-131.

Farabi N., Chen D.L., Zhou Y., 2011. Microstructure and Mechanical Properties of Laser Welded Dissimilar DP600/DP980 Dual-Phase Steel Joints. J. Alloys Compd. 509,982-989.

Jia Q., Guo W., Li W., Zhu Y., Peng P., Zou G., 2016. Microstructure and Tensile Behavior of Fiber Laser-Welded Blanks of DP600 and DP980 Steels. J. Mater. Process. T. 236, 73-83.

Lee H., Kim C., Song J. 2015. An Evaluation of Global and Local Tensile Properties of Friction-Stir Welded DP980 dual-Phase Steel Joints Using a Digital Image Correlation Method. Materials 8, 8424-8436.

Ma J., Kong F., Liu W., Carlson B., Kovacevic R., 2014. Study on the Strength and Failure Modes of Laser Welded Galvanized DP980 Steel Lap Joints. J. Mater. Process. T. 214, 1696-1709.

Ozsarac U., 2012. Investigation of Mechanical Properties of Galvanized Automotive Sheets Joined by Resistance Spot Welding. J. Mater. Eng. Perform. 21, 748-755.

Xu W., Westerbaan D., Nayak S.S., Chen D.L., Goodwin F., Biro E., Zhou Y., 2012. Microstructure and Fatigue Performance of Single and Multiple Linear Fiber Lase Welded DP980 Dual-Phase Steel. Mat. Science and Eng. 553, 51-58.

Wang J., Yang L., Sun M., Liu T., Li H., 2016. A Study of the Softening Mechanisms of Laser-Welded DP1000 Steel. Materials and Design 97, 118-125.

Wang J., Yang L., Sun M., Liu T., Li H., 2016. Effect of Energy Input on the Microstructure and Properties of Butt Joints in DP1000 Steel Laser Welding. Mater. Des. 90, 642-649.

Avrupa Bilim ve Teknoloji Dergisi
Özel Sayı, S. 52-56, Aralık 2017

Konferans Bildirisi

www.ejosat.com ISSN:2148-2683

European Journal of Science and Technology
Special Issue, pp. 52-56, December 2017

Conference Paper

Valorisation of Dune Sand and Wase Brick Filler in Elaboration of Cellular Concrete: Mechanical and Thermal Properties

Damene Zineb[1*], Goual Mohammed Sayah[1] and Saiti Issam[1]

[1] Civil Engineering Laboratory/Amar Telidji University, Laghouat, Algeria

*z.damene@lagh-univ.dz

Abstract

The aim of this work is both to enhance the dune sand in the production of lightweight concrete with local resources, but also enhances the performance of the sandcrete by incorporating fines mineral as fines from waste of brick. Different parameters were studied, in which the quantity of substitution of fines in the dune sand, the proportions substitutions of lime in the cement, the dosage of expansive agent. The result shows that it is possible to producing lightweight concrete suited to the hot and arid environment with an acceptable heat insulation and sufficient compressive strength. The greatest introduced porosity and lowest density are reached from composition without lime and with 0.5 % Al.

Keywords: Brick wastes, Cellular concrete, Dune Sand, Lime.

[*] Corresponding author : z.damene@gmail.com, phone: +213 667838056

1 INTRODUCTION

Southern Algeria is known for its sand dunes, which occupy 60% of the surface of Algeria. In view of enhancement of local resources, the idea of promoting the use of sand dunes in the manufacture of mortars and concretes is interesting. Indeed, many studies in various scientific topics that are focused on dune sand concrete **[1-5]**. Cellular concrete is generally composed of fine sand (powder silica sands), cement, lime, water and an expansive agent).

Some experimental and theoretical studies in the field of aerated concrete have shown some salient observation: (i) mechanical and thermal properties are influenced by method of curing, porosity and pore size **[4]**. (ii) Increase in the cement dosage increase the introduced porosity whereas an increase of the sand or lime dosages decreases the introduced porosity **[5]**. (iii) Insulation is more or less inversely proportional to density of concrete, **[6]**.(iv) Greater the proportion of aggregate, higher will be the density, replacement of sand with fly ash help in reducing the density with an increased strength**[7]**.

The following experimental work aimed to proves that the valorization of the dune sand of the Sahara of Algeria is completely relevant in production of cellular concrete, and that the substitution of fines of brick wastes in the sand dune increases the properties of this type of concrete. The principal of the study consist firstly to change the water cement ratio (W/C) from 0.35 to 0.65 in all the mixtures in order to investigate the effect of brick substituted in the sand dune on the properties of the sand concrete. The mixtures have proportion of 35% of binder and 65% of sand dune **[8]**. The percentage of fines substitutions of wastes of brick in the sand dune was varied from 5% to 25% in order to keep the optimum mixture who gives the high compressive strength (noted SCB). Secondly we add in the binder of the optimized sand concrete (SCB) different percentages of lime (as follow by weight of cement: 10 %, 15%, 20%, 25%, 30%, 40%, 50 %) with an expansive agent (aluminum powder) to create an air void in order to develop a cellular concrete (noted CCB) made with dune sand and waste of brick. In this case the water / cement ratio was adjusted to 75% for giving an easy casting in the moulds.

2 Description of materials

2.1 Dune sand

Dune sand used in the mixtures was taken from Laghouat (south of Algéria) with maximum size of 0.5mm.Table 1 presents physicals and chemicals properties of this dune sand. The grading curve was presented in figure 1.

2.2 Fines of Brick

The wastes of brick were taken from the construction sites and companies; they were crushed to Ø< 100 µm. Physicals properties and chemicals analyses of the fines of brick were presented in table 1. The grading curve was presented in (figure 1)

2.3 Cement

The cement used in this research was Portland cement CEM II 42.5 from ACC (Algerian Cement Company). Physicals properties and chemical composition were given in table 1.

2.4 Lime

The lime used to product the cellular concrete was an artificial Hydraulic Lime. Chemicals analyses and physicals properties were given in table 1.

2.5 Expansive agent

The expansive agent was SIGMA-ALDRICH aluminum powder with 99% aluminum and fineness of 75 µm.

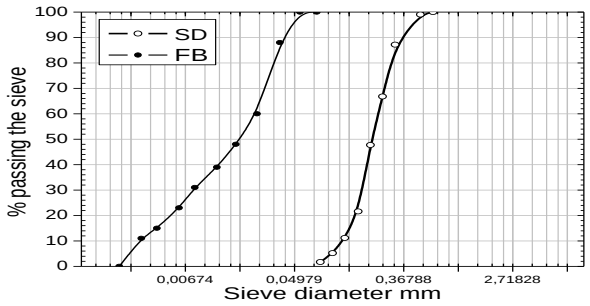

Figure 1. The grading curves of the aggregates.

Table 1. Physical characteristics and chemical composition of the materials

Material	Dune Sand	Fine of Brick	Cement	Lime
Physical propreties				
Apparent density (kg/m^3)	1423.6	2535.5	1030	700
Absolute density (kg/m^3)	2675	770	3100	2430
Equivalent modulus of Sand ES (%)	97	-	-	-
Blue of methylene value Vb	0.067	-	-	-
Fineness modulus / Blaine surface area (cm^2/g)	1.22	2847	3700	2985
Chemical composition				
SiO_2 (%)	95.87	63.62	17.49	< 2.5
SO_3 (%)	2.29	2.4	2.83	< 0.5
$CaCO_3$ (%)	2.5	-	-	< 10
CaO (%)	-	12	62.78	>73.3
Fe_2O_3 (%)	-	5.37	3.02	< 2
Al_2O_3 (%)	-	10.25	4.51	< 1.5
MgO (%)	-	-	2.15	< 0.5
K_2O (%)	-	-	0.64	-
Na_2O (%)	-	-	0.05	< 0.5
CO_2 (%)	-	-	-	< 5
LOI* (%)	-	-	8.10	-
Chlorure (%)	-	-	0.02	-

*LOI: Loss on ignition.

3 moulds and casting

First of all, the solid components were dryly mixed for 2 min. then the total of amount of water was added and mixed for 2 min (In the case of manufacturing cellular concrete, the expansive agent was added at the end with mixing for 1 more minute). All mixtures were cast in 4x4x16 cm^3 moulds for approximately 24 h, after which time they were removing from the mould and stored in 20°C water during 28 days. The expanded samples were sawing of the excess material just before demoulded.

4 Result and discussion

4.1 Optimized Sand-Brick Concrete

The results of compressive strength were used as the indicator of the activity of brick admixture in the dune sand. (Figure 2) shows that the mineral fine admixture has a positive influence in mechanical performance of mortar made with dune sand **[9-11]**. The optimum of strength 73.59 MPa was reached for mortar with 15% of fines of brick and with ratio W/C = 50%.

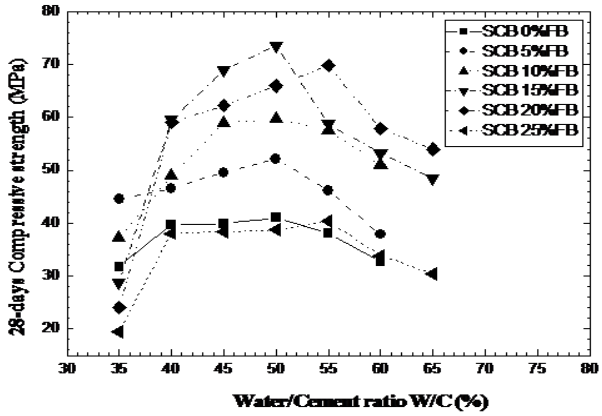

Figure 2. Effect of fine of brick on compressive strength

4.2 Cellular Concrete of sand-Brick (CCB)

For developing the cellular concrete (CCB) in this research we have added to the reference optimized mortar (SCB) different percentage of lime with two percentage of the Aluminum powder (0.2% and 0.5%) in order to show the effect of the lime and Aluminum on the properties of: apparent density, introduced porosity, compressive strength and thermal conductivity.

4.2.1 Influence of lime on the apparent density

The results showed in (figure 3) indicate an increase in the apparent density until 25% of dosage of lime after this percentage the density decrease, it is the same conclusion for the two ratios of Aluminum. The lowest density (1209.11 Kg/m^3) is reached from the concrete with binder made only of cement (0% lime). It means that the expansive agent acted only with the (Ca (OH) $_2$) formed during the hydration reaction of cement (In contact with water, tricalcium silicate (Ca_3SiO_5) and dicalcium silicate (Ca_2SiO_4) dissolve as ions that interact and form calcium silicate hydrates (CSH) and portlandite (Ca (OH) $_2$). This result is consistent with the literature **[5].**

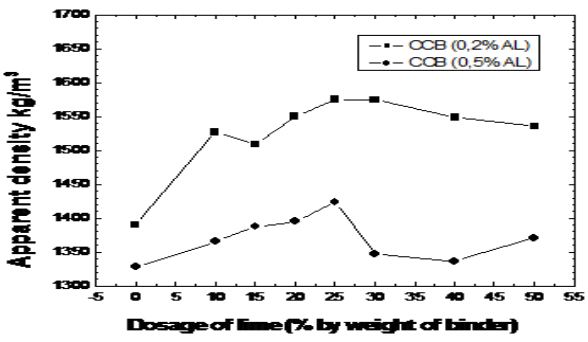

Figure 3. Effect of lime on the apparent density of CCB

4.2.2 Influence of lime on the introduced porosity

The introduced porosity was determined from the measurement of the dry apparent densities of the reference mortar and of the expanded samples by the expression:

$P_i = (p_r - p_e) / p_r$ (1)

Where P_i : is the introduced porosity

p_r : the dry apparent density of the reference mortar

p_e : the dry apparent density of the expanded sample

The results of introduced porosity versus the dosage of lime complete the above conclusion. Figure 4 indicates that the porosity decrease with the increase of percentage of lime till 25% of lime after this dosage the porosity increase. This decrease of porosity means that the reaction capacity of lime with the expansive agent is less important than that of cement **[5]**.

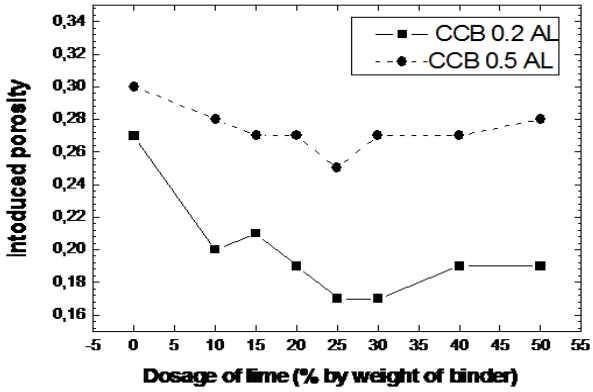

Figure 4. Effect of lime on the introduced porosity of CCB

4.2.3 Influence of lime on the compressive strength

Figure 5 show the influence of dosage of lime on the compressive strength. The increasing dosage of lime increase the compressive strength till 25%, after this optimum the compressive strength diminishes with increase of dosage of lime. The highest strengths which are obtained from composition with 25% of lime are 7.44 MPa with 0.5 % of Aluminum and 10.62 MPa with 0.2% of Aluminum.

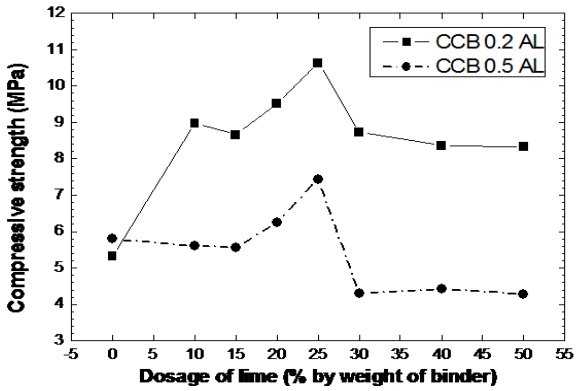

Figure 5. Effect of lime on the compressive strength of CCB

4.2.4 Influence of lime on the thermal conductivity

The thermal conductivity depends on density and on insulation characteristics of the ingredients of the material **[13, 14,** and **15].** The amount and fineness of pores influence also the thermal insulation **[4, 14]**. Figure 6 and 7 shows thermogrammes obtained using hot wire method. The thermal conductivity increases with the increase of lime till 25% of lime and decrease after this dosage; this result proves that this lime has not a role in the processes of alleviation. The lowest value of thermal conductivity (0.505 W/m°C) is given by composition CCB without inclusion of lime, and which has the greatest introduced porosity (Pi=0.3).

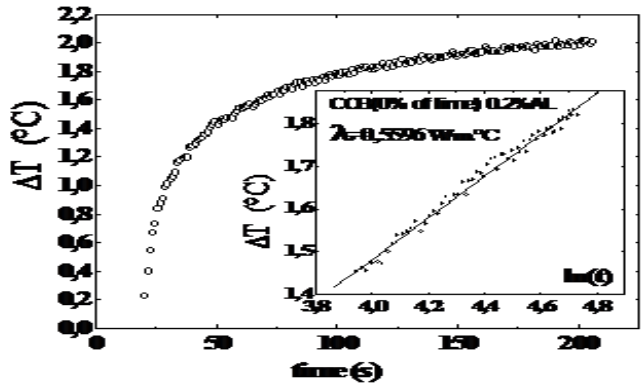

Figure 6. Thermal conductivity of CCB (0% of lime, 0,2% AL)

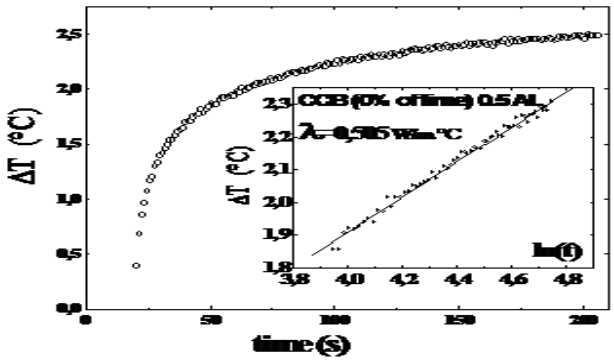

Figure 7. Thermal conductivity of CCB (0% of lime, 0,5 % AL)

4.2.5 Influence of expansive agent contain

In this study all the results (fig. 3-4-5) shows that the dosage of Aluminum possesses a great influence on the properties of the material developed. Compared with dosage of 0.2% of Aluminum, the dosage of 0.5% gives the lowest apparent density which is due to the greatest development of the porosity (30%); consequently, the increase of porosity leads to a decrease in the compressive strength.

5. CONCLUSION

The results of this experimental work to develop a novel material as cellular concrete using especially local ingredients like sand of dune which is plentiful in the Sahara of Algeria and wastes of brick, shows that it is possible to investigate in this type of concrete to producing lightweight concrete suited to the hot, arid environment of our region.

The developed material in this research is a non-autoclaved concrete, and we have reach a very acceptable value of characteristic (1209.11 Kg/m^{3}for apparent densities, 3.67 MPa for the compressive strength and 0.505 W/m°C for thermal conductivity) entering in the margin Classification of lightweight concrete **[15]**. Substitution of fine of brick in the sand of dune could play an important role in the increase of the mechanical performance of sand concrete.

References

[1] I. K. Cisse, M. Laquerbe. Mechanical characterization of filler sandcretes with rice husk ash additions : Study applied of Senegal. Cement and Concrete Research 30; 2000 ; 13-18.

[2] A. S. Al-Harthy, M. Abdelhalim, R. Taha, K. S. Aljabri. The properties of concrete made with fine dune sand. Construction and Building Material 21; 2007 ; 1803-1808.

[3] H. Wajahat, Mirza, Solman, I. Al- Noury. Utilisation of Saoudi sands for aerated concrete production. The International Journal of Cement and Composites and Lightweight Concrete. Volume 8, number 2; May 1986.

[4] N. Narayanan, K. Ramamurthy. Structure and properties of aerated concrete: a review. Cement & Concrete Composites 22 ; 2000 ; 321-329.

[5] R. Cabrillac, B. Fiorio, A. Liss Beaucour, H. Dumontet, S. Ortola. Experimental study of the mechanical anisotropy of aerated concretes and of the adjustment parameters of the introduced porosity. Construction and Building Materials 20 ; 2006 ; 286-295.

[6] Shrivastava OP. Lightweight concrete – a review. Indian Concrete Journal 51; 1977; 10-23.

[7] FC. McCormick. Rational proportioning of performed foam cellular concrete. ACI Material Journal 64 ; 1967 ; 104-109.

[8] C. Guegan, P. Legras, J.F. Mazzoleni, C. Colin, T. Breiner, N. Foussier. Mémento du béton cellulaire. Grouppe Eyrolle; 2005.

[9] P. Lawrance, M. Cyr, E. Ringot. Mineral admixtures in mortars effect of type, amount and fineness of fine constituents on compressive strength. Cement and Concrete Research 35; 2005 ; 1092-1105.

[10] M. Cyr, P. Lawrance, E. Ringot. Efficiency of mineral admixtures in mortars: quantification of the physical and chemical effects of fine admixtures in relation with compressive strength. Cement and Concrete Research 36; 2006 ; 264-277.

[11] U. Chinje Melo, N. Billong. Activité pouzzolanique des déchets de briques et tuiles cuites. African Journal of Science and Technology, Science and Engineering Serie ; Volume 5 ; numéro 1 ; pp 92- 100.

[12] KL. Watson, NB Eden, JR Farrant. Autoclaved aerated mateials from slate powder and portland cement. Precast concrete ; 1977 ; 81-85.

[13] TG. Richard. Low temperature behavior of cellular concrete. J Am Conc Inst ; 47 ; 1977 ; 173-178.

[14] RC. Valore. Insulation concrete. J Am Conc Inst ; 28 ; 1956 ; 509-532.

[15] JL. Kass, Allen D. Campbell. Functional classification of lightweight concrete. Matériaux et Construction ; Volume 5 ; N° 27 ; pp 171-172.

.

Avrupa Bilim ve Teknoloji Dergisi
Özel Sayı, S. 57-61, Aralık 2017

Konferans Bildirisi

www.ejosat.com ISSN:2148-2683

European Journal of Science and Technology
Special Issue, pp. 57-61, December 2017

Conference Paper

Simulation of local scour development downstream of broad-crested weir with inclined apron

ARKAN IBRAHIM[1], AZHEEN KARIM [2], Mustafa GÜNAL[3]

[1]Gaziantep University, School of Natural and Applied Science, Civil Engineering Department, Şehitkamil, 27310, Gaziantep, Turkey, arkan.hamza@koyauniversity.org
[2]Gaziantep University, School of Natural and Applied Science, Civil Engineering Department, Şehitkamil, 27310, Gaziantep, Turkey, azheen.karim1990@gmail.com
[3]Gaziantep University, School of Natural and Applied Science, Civil Engineering Department, Şehitkamil, 27310, Gaziantep, Turkey, gunal@gantep.edu.tr

Abstract

Broad crested weirs are hydraulic structures used to control the flow depth and discharge of channels. Structures constructed in rivers and channels are exposed to scour around their foundations as they cause turbulences in uniform flow and sediment transport as a result of increase in flow velocities at downstream. If the scour depth becomes substantial the stability of the foundations endangered with a resultant hazard to the structural failure. In this study the flow field variation and the equivalent depth of scour was simulated by means of three-dimensional numerical analysis using a sediment scour model of FLOW-3D program. The sediment scour model in FLOW-3D is able to simulate the scour hole development process, in this study four models of inclined apron of broad crested weirs [A, B, C, D] with different downstream reverse angles (0˚, 4.5˚, 8.7˚ ,13˚) respectively are tested under the same flow intensity and the same duration, based on experimental study from the literature that has been held for a duration of 6 hours to see if the same behavior will be concluded for scour reduction. Downstream of the first models act as ordinary weir while the other models act as an obstacle toward the flow, the water flows above the sloped downstream bed and dissipates some of its energy. There was a good agreement between experimental and FLOW-3D results. The results showed, that model C reduces local scour hole volume, the maximum scour depth in addition shift the scour holes away from the structure as compared to the other models. The idea is decreasing downstream height of broad crested weir while providing an obstacle in shape of sloped downstream bed toward the flowing water. This reduction gave the weir a new performance by making it as an energy dissipater. The present technique similarly reduces construction costs also improves the hydraulic performance of single step broad crested weirs.

Keywords: Sediment scour, scour reduction, erosion, FLOW-3D, broad crested weir.

1. Introduction

Weirs are defined as an obstacle in an open channel system which water flow over it and based on the geometry of the weir and head on the weir crest, it is used as an indirect technique for the flow rate measuring (King and Braver, 1963). One of the most common types of weirs are the broad-crested weir, the main issues related to such structures are scouring at the downstream of weir structures which are the leading causes of their failure. Numerous different methods were tested and applied to study and minimize the local scour. Ozmen-Cagatay and Kocaman (2011), for simulating a dam-break used FLOW-3D software where the applied turbulence model presented good agreement to experimental outcomes. Amin (2015) used physical model to evaluate and compute the influence of hydraulic structural measure (double lines water jets) on minimalizing the dimensions of scour-hole downstream of a Faiyum model of weir. His experimental outcomes confirmed the suitability and the usefulness of the proposed measure (floor water jets) in improving the flow hydraulic conditions and the local scour dimensions downstream Faiyum type weir. Helal (2013), studied the effect of installing a single line water jets to the floor of the hydraulic structures on reducing the scour hole sizes and determined that the system of floor water jets is effective in reducing the cost of energy dissipating stilling basin. Abdelhaleem (2013) experimentally studied the influence of semi-circular shapes of baffle block on local scouring downstream of a Faiyum kind weir. He reported that; the existence of baffle blocks, both upstream and downstream slopes of the scour hole formation increase but the downstream slope is steeper than the upstream, that specifies the important impact of baffle blocks on the scour hole dimensions. Dargahi (2003) conducted a laboratory investigation to study the scour profiles and the scour geometry likeness. No experimental indication was determined in support of the similarity assumption for time-based progress of the scouring development. For the geometry of scour hole prediction, he introduced power-law form equations, primarily in terms of affecting variables such as, depth of flow over the spillway crest and sediment particle size.

In this study, validation of FLOW-3D program is conducted in terms of the program capabilities for predicting scour developments downstream of broad crested weir. The validation is based on the simulation of the experimental study made by Abdulnaser et al (2015). The maximum scouring depths and volume of scour downstream weirs crest are compared with available experimental data. Additionally, the conclusion of the best model for scour reduction are investigated.

1 2. Model Setup

In this study FLOW-3D is used to simulate a numerical model based on an experimental study of (Abulnaser et al, 2015). FLOW-3D is a commercial package developed by Flow Science Inc. (Flow Science Inc., 2009) at Los Alamos Scientific Lab. The software practices some superior features for numerical solution of the Navier-Stokes equations for free surface flows (VOF-method) and meshing of complex geometries (FAVOR method). The sediment scour model in FLOW-3D treats sediment by way of two concentration fields (Brethour, 2003): the suspended sediment and the packed sediment. The suspended sediment advects and drifts with the fluid because of the effect of the local pressure gradient. Suspended sediment initiates from inflow boundaries or from erosion of packed sediment. The packed sediment does not advect, and characterizes sediment that is bound by adjacent sediment particles.

Figure 1 shows the experimental flume setup for an inclined apron of broad crested weirs. Water enters the flume with a discharge of 25 l/s. The water flows over a solid bed, 38.4 cm in length, before contacting a packed bed of sand 200 cm in length and 19.2 cm in depth. The median diameter of the sand grains is 1.8 mm. The channel is 80 cm in width, the scour profiles were measured down the centerline of the flume.

FLOW-3D mesh generator to handle the complex geometries uses the FAVORTM technique in an orthogonal mesh defined in Cartesian or cylindrical coordinates. Only the orthogonal mesh is permitted to simplify the development of meshing domain in FLOW-3D. The obstacles and baffles are embedded in the

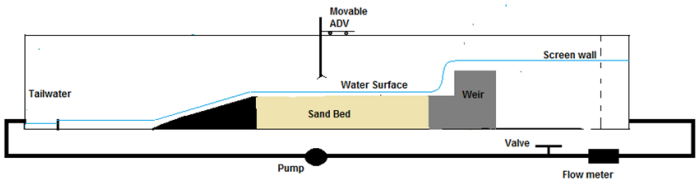

Figure 1. Schematic layout of the flume (Abdulnaser et al, 2015).

orthogonal mesh, which tolerates separate characterization of the mesh and geometry. Figure 2 shows the 3D computational domain that is 300 cm long starting the slit and 50 cm high including 19.2 cm of packed bed. There are 23634 mesh cells in total. In the simulation, the density of sand is 2.65 g/cm3.The weir downstream adverse slope arrangement in FLOW-3D was achieved by inserting a STL file format. In STL files formats solid object surfaces are approached by triangle systems. To convert the solid model into STL format AutoCAD program was used. One uniform mesh block was used for the domain discretization. A grid sensitivity analysis with respect to the computational time was performed. The grid was refined till the computational time increased unreasonably.

Boundary conditions for y minimum direction was considered to be “symmetry”, which indicates that identical flows happen on the other side of the boundary and hence there is no drag on this boundary. In the x direction, the boundary condition was “specified stagnation pressure”. With this algorithm, FLOW-3D is able to model various flow heights beginning at a stagnation pressure state. A continual volume flow rate was used as inflow boundary condition. Figure 2 represents boundary conditions on the x-y-z planes. In the simulation with single fluid, the critical Shields parameter was 0.05, both the entrainment and bed load transport coefficient values were 0.0018 and 8.0, respectively, the angle of repose was 45° and the critical packing fraction was 0.64. The turbulence was predicted using Renormalized group (RNG) model.

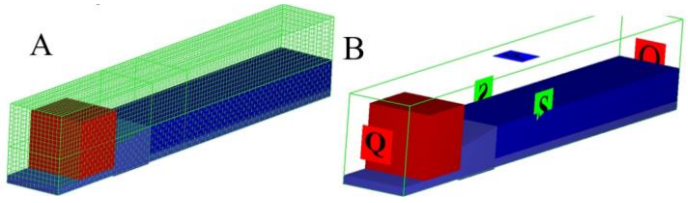

Figure 2. A- Computational domain and mesh setup to simulate scour in the flume, B- Configurations of boundary conditions.

3. Results and Discussion

3.1 Investigating effect of inverted slope on water surface profile and velocity downstream of weirs crest

In different models of weirs' crest, the changes of water surface profile of numerical results are investigated and compared with experimental data (Figure 3 and 4). Based on the results extracted from the diagram of water surface profile on weirs' crest, it can be predicted that there is a clear influence of the change in downstream slope on the water surface profile which results in the change of the hydraulic parameters of the system. In addition, leads to change in the rate of the scouring. Figures 3 and 4 shows the experimental and numerical results and from these plots it can be understood that there is a good agreement among the Flow-3D and experimental results. As its seen the water surface at model A is smooth and effect on larger distance at downstream of the weir but the water surface at model B and D are more turbulent because the effect of inverted slope on water falling at downstream of the weir, hence the horseshoe vortex is very strong for models B and D, but then again the effect of horseshoe vortex is reduced for model C as a result of large energy dissipation and effect of the downstream slope of the weir lead to decrease the energy of water. It is Obvious from Figure 4 that the maximum velocity was found on the sloped bed and then decreased immediately after the weir structure due to the energy dissipation on the sloped bed, as model C downstream slope caused energy dissipation more than other models which resulted in the high scour reduction**.**

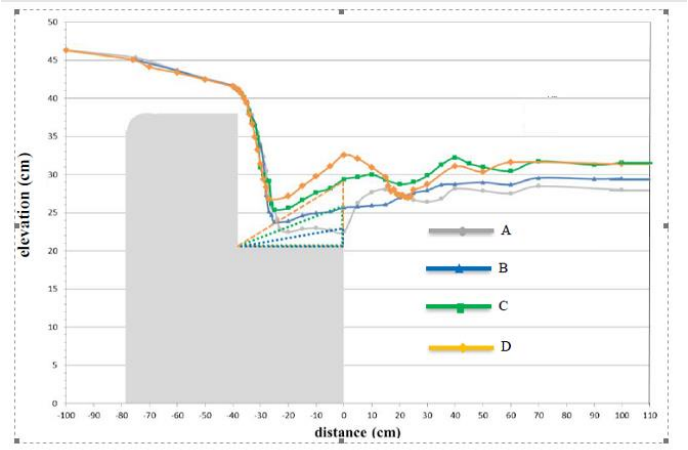

Figure 3. Experimental longitudinal water surface for each model Q = 25 **l/s**

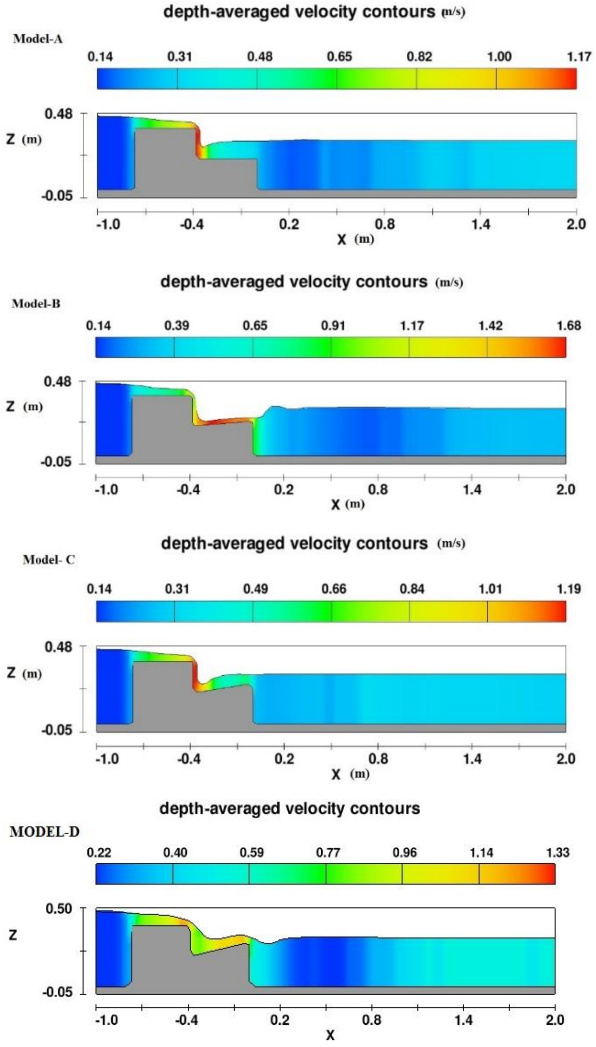

Figure 4. Comparison of longitudinal water surface profile and depth average velocity at the central axis on the weirs' crest in various models Q = 25 l/s

3.2 Investigating effect of inverted slope on scouring downstream of weirs crest

Figures 5 and 6 present the measured and the calculated scour profiles for all models, respectively. It is found the calculated shape and elevation of the sand bed compare well to those measured in the experiment. As measured, a scour hole is generated just behind the weir due to entrainment and bedload transport. Figure 6 shows the maximum scour hole depth from numerical results. Good agreement is observed between the measurement and the calculation. The maximum scour hole depth is only slightly underestimated**.**

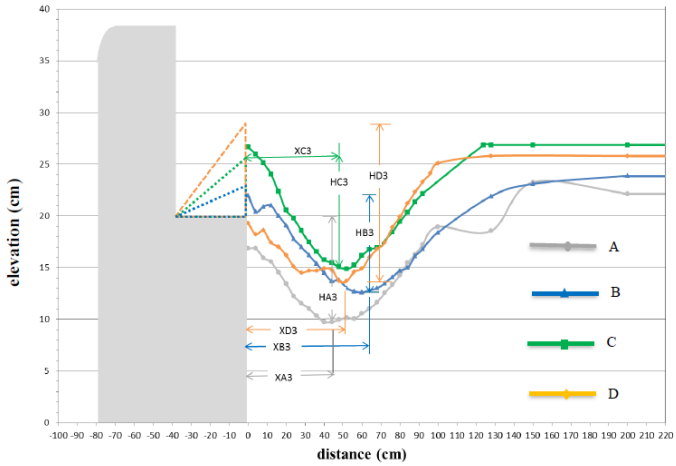

Figure 5. Experimental result of longitudinal scour holes and distances from the weir for each model Q = 25 l/s.

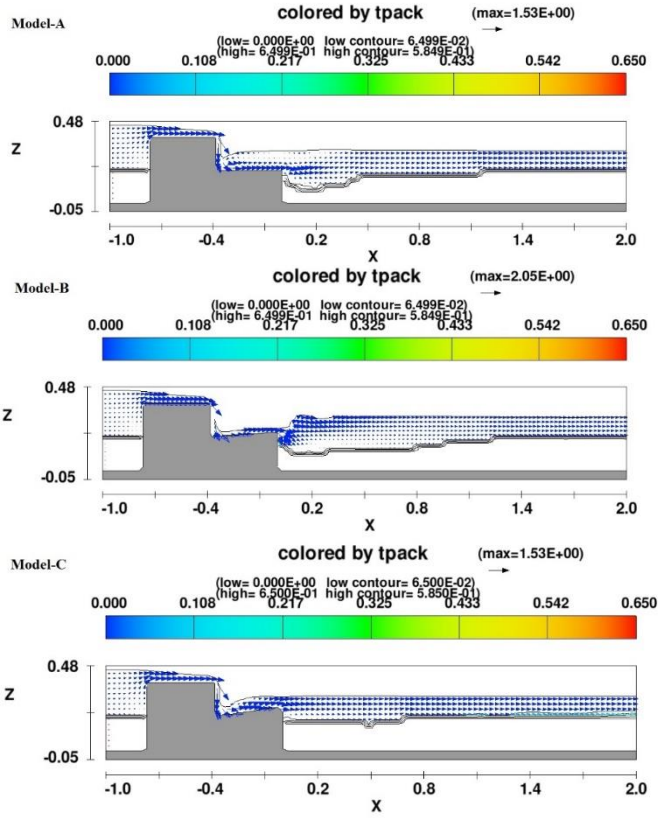

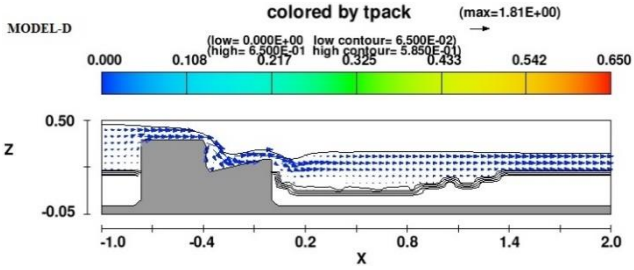

Figure 6. Calculated results of longitudinal scour holes and distances from the weir for each model and discharge (25 l/s), tpack (total packed sediment solid fraction).

As shown in Figures the maximum scour depth was initiated after the weir model D for the reason that the drop of water adjacent from the toe of the weir. This case increases the danger of failure of the weir. While model C reduces depth of scour and creating least scour in the downstream of the weir and pushes the drop of water away from the weir.

From Table 1 it is obvious that the model C reduces the scour depth and the volume of local scour as compared to the other models. This is because the slope of downstream of the weir resulted in the formation of weak horse shoe vortex. Results comparison for the same discharge of 25 l/s showed that in the experimental results model C reduced scour depth and scour hole volume about 24.2% and 44.8% respectively as compared to the models D. While from numerical results comparison showed that scour depth and scour hole volume was reduced about 37.5% and 50.1% respectively.

Table 1. Local scour dimensions for each model

Model	θ°	Q (l/s)	Volume of scour (cm^3)		Max. depth of scour H (cm)		Distance from weir X (cm)	
			Exp.	Num.	Exp.	Num.	Exp.	Num.
A	0	25	48583	47800	12.4	11.8	68	40
B	4.5	25	52680	42500	12.4	10.1	48	36
C	8.7	25	43784	33200	12.2	8.5	76	69
D	13	25	79316	66600	16.1	13.6	48	44

3.3 Investigating effect of inverted slope on flow pressure distribution downstream of weirs crest

In various models of weirs' crest, the outcome of flow pressure distribution changes on broad-crested weirs is studied. In Figure 7, flow pressure values simulated for central axis of channel in longitudinal direction and has been presented. It is useful to determine the way of pressure distribution to consciously apply energy equations and motion size in weirs. If in case of designing, pressure imposed on weir is more than atmosphere pressure, discharge is decreased and vice versa; also, it simultaneously causes to the creation of cavitation phenomenon. Therefore, it is highly important to investigate pressure distribution on weirs' crest. Accordingly, in the following,

precise process of pressure distribution and changes under the impact of weir's downstream slope are investigated. And the outcomes show that the higher the pressure occurred at the location of maximum socur of the models and model C reduced pressure at the downstream in a great manner and caused a high reduction in socur hole formation. Which indicates that Increasing inverse downstream slope with a spcific degree leads to the decrease of pressure value, which shows the energy dessipasion caused by ineverted downstream slope as it can been seen clearly from model C.

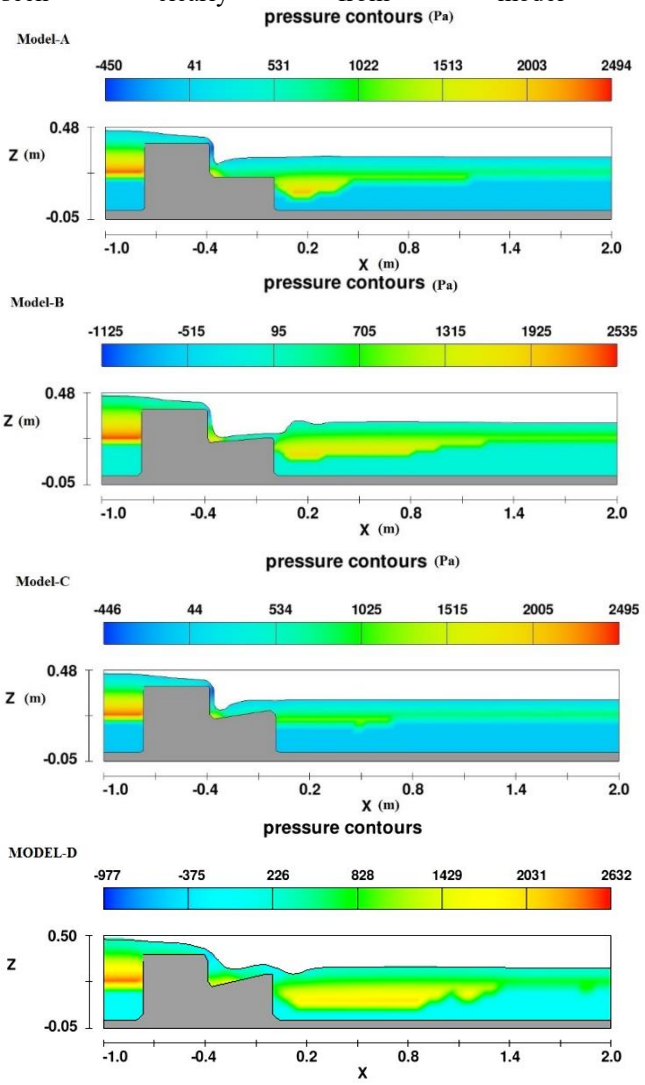

Figure 1. Flow pressure distribution changes on weirs' crest for different models.

4. Conclusions and recommendations

The present work was an effort to examine hydraulic characteristics and parameters that reduces scour due to the change of the downstream apron inclination of broad crested weir and checking numerical capabilities using computational fluid dynamics method. In this regard, FLOW-3D model was studied by changing gridding as well as changing different parameters of the model. For the result validation, FLOW-3D study was based on laboratory experiment models from literature experiments studied the application of a new shape of downstream apron of broad crested weirs. Changing the slope of downstream apron is not only effective for reducing local scour but it is also much more economic when it is related to traditional broad crested weir. The current study demonstrates that there is no need to countermeasure the scour depth by lining with rubbles and riprap to protect from failure since the distance of scour from weir was significant to avoid that, the new idea is only to change the inclination of downstream apron of the weir.

Acknowledgements

The authors are grateful to Ministry of Environment and Urbanism of Turkey for the air quality data. This work was part of the Turkish Scientific and Technical Research Council (TUBITAK) Project No: 111Y319. This study is a background of the online integrated air quality and meteorology modeling project funding by the TUBITAK and COST Action ES1004.

References

Abdulnaser A., Mustafa G., Hamid H. 2015. Investigating of Local Scour and Discharge Characteristics of Single Step Broad Crested Weir. (ICCESEN 2015), 14-19 October, 2015. Antalya-Turkey.

Abdelhaleem F.S.F. 2013. Effect of semi-circular baffle blocks on local scour downstream clear-overfall weirs. Ain Shams Eng J 4 (4) 675–684.

Amin A.M.A. 2015. Physical model study for mitigating local scour downstream of clear over-fall weirs, Ain Shams Eng J 6 (4) 1143-1150.

Brethour, J. 2003. Modeling Sediment Scour. Flow Science, Inc. Report FSI-03-TN62.

Dargahi B. 2003. Scour development downstream of a spillway. J Hydraul Res; 41(4):417–426.

Flow Science Inc. 2009. *Flow-3D v9.3*. New Mexico, USA.

King, H.W. and E.F. Braver 1963. Handbook of Hydraulics, 5th Edition, McGraw-Hill Book Company, New York.

Helal E.Y. 2013. Minimizing scour downstream of hydraulic structures using single line of floor water jets Ain Shams Eng J. 5(1) 17-28.

Ozmen-Cagatay H. and Kocaman S. 2011. Dam-break flow in the presence of obstacle: experiment and CFD simulation. Engineering Applications of Computational Fluid Mechanics 5(4) 541-552.

Avrupa Bilim ve Teknoloji Dergisi
Özel Sayı, S. 62-64, Aralık 2017

Konferans Bildirisi

www.ejosat.com ISSN:2148-2683

European Journal of Science and Technology
Special Issue, pp. 62-64, December 2017

Conference Paper

Parametric Study for Performance Evaluation of Concrete Filled Steel Composite Circular Members According to Design Codes

Moshtak Taleb ABDULMAGED[1], Mehmet Tolga GÖĞÜŞ[2]

[1] Gaziantep University, Civil Engineering Department, Gaziantep-TURKEY

[2] Gaziantep University, Civil Engineering Department, Gaziantep-TURKEY

(First received 31 May 2017 and in final form 14 December 2017)

Abstract

The Concrete Filled Steel Tubular (CFST) members offer many structural features and have been widely used in civil engineering structures. Available in many different shapes, but most important circular, rectangular and square, etc. The CFST structures offer numerous structural benefits, including high strength, favorable ductility, and highly absorbable to withstand external shocks. They have proven to be economically as well as providing for the rapid construction and thus additional cost savings. The circular CFST members included normal strength concrete filled circular structural sections. In this study the parameters; diameter (D), thickness (t), yield stress (f_y), and compressive strength of concrete (f_c') show their effects on the members and their comparison, according to calculation equations of the American (AISC360-16) and European (EC4-2004) codes for the design of which parameter effects performance of circular CFST members under axial compression and flexure.

Keywords: Circular CFST members, Axial strength, Flexure strength, Parametric study, Design codes.

1. Introduction

Concrete Filled Steel Tube (CFST) is a composite member which consists of a hollow steel pipe filled with concrete (Gore, et al.). The Circular Concrete Filled Steel Tubes (CCFST) section withstands applied load through the composite job of steel and concrete. The benefits of composite action between concrete and steel increase the strength of CCFST section. Thus, becoming popular in the last days and being used in structures such as bridges, buildings, electricity towers etc. In the past years, several studies have been done on CCFST members, these studies indicated that the CCFST sections possess strength, stiffness properties, and high ductility. These properties are considered to be important, especially for the multi-story buildings. Therefore, the behavior of buildings with CCFST sections needs to be studied (Han, et al. 2004). Concrete is one of the most important materials involved in the construction of civil engineering. Moreover, it is a favorite material because it is low-cost, durable and high-tech, easy to manufacture. In recent years, there have been some significant developments in the field of concrete technology (Bozkurt, et al. 2017, Davraz, et al. 2017). Steel is one of the most widely used materials in structural applications because of its high strength in endurance for external shocks, high rigidity, and average cost. With these attractive properties, Steels are the most commonly used materials in buildings, forming structures, etc. (Abakay, et al 2017, Acar et al. 2017). The current paper represents an attempt to investigate the effect of different parameters on the ultimate axial and flexural capacities of CCFST sections according to the AISC360-16 and EC4-2004. The investigated parameters considered in this study; (D) diameter, (t) thickness, yield stress (f_y), and compressive strength of concrete (f_c').

2. Design Code Factors and Limitations

In this study, the (D) and (t) were chosen from according to EN 10219 standard, Not to exceed the limits of the AISC360-16 and EC4-2004 codes. According to standard EN 10219, value domain $(D\ mm)$ = (21.3-339.7) and value domain $(t\ mm)$ = (2.0-12.7), are calculated with values f_y (235, 275, 355) MPa and f_c' (20, 30, 40, 50, 60) MPa, respectively, and so with the rest of the values. The length of column $(L\ mm)$ = 3000 is taken constant. Limitations for each code;

AISC CODE

Concrete Compressive Strength (MPa)	$21 \leq f_c' \leq 70$
Steel Yield Strength (MPa)	$f_y \leq 525$

EC4 CODE

Concrete Compressive Strength (MPa)	$20 \leq f_{ck} \leq 50$
Steel Yield Strength (MPa)	$235 \leq f_y \leq 460$

3. Generalized Linear Design Model

An alternative to the typical data conversion approach is followed by the standard lower squares analysis of the converted response is the use of the generalized linear model. A generalized linear model is basically a regression model (an experimental design model is also a regression model) which can be used for determination percent contributions of parameters (Montgomery, D. C. 2017).

4. Results and Conclusion

By applying the generalized linear model to the data set created using the excel sheet, 5445 analysis was performed on each code columns and beams. Table 1 shows the final influence of each parameter on the axial and flexural strength of the CCFST member according to AISC 360-16 and EC4-2004 code.

Table 1. Results and percent contributions for axial load and bending moment capacities according to AISC360-16 and EC4-2004

Factors	AISC 360-16		EC4-2004	
	% of Total		% of Total	
	$M_n\ (kN.m)$	$P_n\ (kN)$	$M_n(kN.m)$	$P_n\ (kN)$
$(D)\ mm$	66.53	82.98	64.73	40.74
$(t)\ mm$	26.25	10.40	27.47	31.69
f_c'/f_{ck} (MPa)	0.07	1.46	0.00	3.75
$f_y\ (MPa)$	1.31	0.40	1.58	16.45

There are many important parameters that affect the capacity of CCFST members, such as the geometric characteristics $(D)$and (t)that has a large effect on the resistance of the section. By observing the results in Table 1, $(D)$and (t) has a significant effect on CCFST members as opposed to less influential factors $(f_c', f_{ck}\ and\ f_y)$ Columns and beams diameter and thickness are different contributions on capacity calculations of design codes. These conflicts are established on the accounting confinement of concrete. Pre-designed CCFST beams and columns are the most important points for design engineers to determine the diameter or thickness of a column or beam.

5. References

Gore, V. V., & Kumbhar, P. D. Performance of Concrete Filled Steel Tube (CFST) Section: A Review.

Han, L. H. (2004). Flexural behavior of concrete-filled steel tubes. Journal of Constructional Steel Research, 60(2), 313-337.

Bozkurt, N., & Taşkin, V. (2017). Design of Self Compacting Lightweight Concrete Using Acidic Pumice with Different Powder Materials. Acta Physica Polonica, A, 132(3), 779-782. DOI: 10.12693/APhysPolA.132.779.

Davraz, M., Pehlıvanoğlu, H., Kilinçarslan, Ş., & Akkurt, İ. (2017). Determination of Radiation Shielding of Concrete Produced from Portland Cement with Boron Additives. Acta Physica Polonica, A, 132(3), 702-704. DOI: 10.12693/APhysPolA.132.702.

Abakay, E., Durmaz, M., Sen, S., & Sen, U. (2017). An Electrochemical Study of the Corrosion Resistance of Niobium-Aluminum Carbonitride Coating Produced on Steels by Thermo-Reactive Diffusion Technique. Acta Physica Polonica, A, 132(3), 682-684, DOI: 10.12693/APhysPolA.132.682.

Kanca, E., Eyercioğlu, O., Karahan, I. H., Günen, A., & Göv, K. (2016). Effects of Blanking Speed on the Shear Surface of Mild Steel (St37). Acta Physica Polonica, A, 130(1). DOI: 10.12693/APhysPolA.130.370.

Acar, İ., Sıksık, V., Varol, F., & Aslanlar, S. (2017). Investigation of Mechanical Properties of Butt Joints of DP800 Thin Zinc-Coated Steel Plates, CMT-Brazed Using Different Current Intensities. Acta Physica Polonica, A, 132(3), 849-851, DOI: 10.12693/APhysPolA.130.370.

AISC. 360-16. Specification for structural steel buildings. Chicago, IL, USA: AISC; 2016.

Eurocode. Eurocode 4: design of composite steel and concrete structures. Part 1-1: General rules and rules for buildings. Brussels, Belgium: CEN; 2004.

Montgomery, D. C. (2017). Design and analysis of experiments. John Wiley & Sons.

Avrupa Bilim ve Teknoloji Dergisi
Özel Sayı, S. 65-69, Aralık 2017

Konferans Bildirisi

www.ejosat.com ISSN:2148-2683

European Journal of Science and Technology
Special Issue, pp. 65-69, December 2017

Conference Paper

Signal Flow Graph – The Right Presentation of an Electrical Circuit[#]

Feim Ridvan RASIM[*], Sebastian M. SATTLER

Chair of Reliable Circuits and Systems, LZS, Friedrich-Alexander-University Erlangen-Nuremberg, Paul-Gordan-Str. 5, 91052 Erlangen, Germany,
Email: feim.rasim@fau.de,sebastian.sattler@fau.de

[#] Presented in "3rd International Conference on Computational and Experimental Science and Engineering (ICCESEN-2016)"

Abstract

In this paper a method called "signal flow graph (SFG)" is presented, which represents a system by its signal flows, in abstract term it is a directed and weighted graph with signals in nodes and functions on edge. The edges of this graph are small processing units which process the incoming signals in specific form and send the result to all outgoing nodes. The SFG allows a good visual inspection into complex feedback problems. Furthermore such a presentation allows for a clear and unambiguous description of a generating system, for example, a netview. A Signal Flow Graph (SFG) allows a fast and practical network analysis based on a clear data presentation in graphic format of the mathematical linear equations of the circuit. During creation of SFGs the Direct Current-Case (DC-Case) was observed since the correct current and voltage directions was drawn from zero frequency. In addition, the mathematical axioms, which are based on field algebra, are declared.

Keywords: Analog Circuit, Transfer Function, Symbolic Analysis, Signal Flow Graph, Network Theory.

1. Introduction

There are diverse methods to calculate transfer functions of electrical circuits such as two-port network theory, nodal analysis method (Schmidt et al. 2006) and time constant method (Gaetano et al. 2003). These methods are generally time-consuming and computationally intensive. Furthermore, it is always useful to develop a common graphical model, with using this model to make a connection between the state variables (parameters) and the transfer function as well as to obtain a better understanding of the complex functionality of a network. Using mesh rules, node rules and Ohm's equations can a signal flow graph set up. Targeted minimization of subgraphs, allows the calculation of a transfer function easier. In this work we repeat the mathematical methodology for the symbolic analysis of real electronic circuits on the basis of a given real circuitry. It is based on graph theory, the so called SFG method. To present the application we use a Common-X circuit as a use case. First, the Common-X circuit is split into its subcircuits and for each subcircuit it associated SFG is established. Then by the superposition of the SFGs of the subcircuits the total SFG for the Common-X circuit results.

2. Theoretical foundations

Signal flow graph: A signal-flow graph describes a system by its signal flows by directed and weighted graph (Samuel et al. 1956). Similarly, an SFG provides a graphical representation of a set of linear relationships (Brzozowski et al. 1963). For this reason, signal flow graph can be constructed between the materials using the Kirchhoff's laws the current and voltage relationship. The directed and undirected graphs, the signals are applied to nodes and functions on edges, the direction is given by an arrow on the edge. The nodes of the signal flow graphs are small processing units, through which the incoming signals are processed in a certain form. In this case, the result is sent to the outgoing edges (Richard et al. 2006). In network theory often are used ohmic resistors, capacitors and inductors. When considering these elements, the direction of the directed and weighted signal flow graph cannot be interchanged easily. Prior to changing the direction of the arrow direction, the function on the edge has to be inverted. The below material equation is shown as an example. The signal flow graph with the respective function on the edge is shown in Figure 1 (Fakhfakh et al. 2012).

Figure 1. SFG an ohmic resistance

Elements of a signal flow graph: A signal-flow graph exists next to edges and nodes of paths, loops, input node and output node. A node is a point or a circle, which reproduces a signal or a variable. Input node, also known as source node, has only outgoing paths and represent independent variables. An output node, also known as sink node, has only incoming paths and is in contrast to the input node a dependent variable. A path is a connected sequence of edges in one direction. The path gain is the product of the functions on the edges along a path. A reverse path is a path that leads towards the entrance node. A feedback loop is present when the start and end nodes are the same. Loops are equal oriented edges forming a closed path and will touch no node multiply. A self-referential loop is exactly present when a path flows from one node in the same node without crossing other nodes (Frieder et al. 2012).

Modifications of signal flow graph: By **associative law** sequential edges can be catenated (Figure 2). As soon as three nodes which are interconnected via a path so present, that there are the $x_0 \to x_1 \to x_2$ connected, the central node x_1 is eliminated from the graph:

$$x_0 \cdot a = x_1;\ x_1 \cdot b = x_2 \implies x_0 \cdot a \cdot b = x_2$$

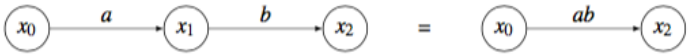

Figure 2: Summary sequential edges - associative law

Parallel running edges with the same input node x_0 and output node x_1 can be concatenated with the **distributive law** (Figure 3). The resulting graph is minimized to an edge. For example, two edges from node x_0 flow into the node x_1. Algebraically, the node x_1 be expressed as:

$$x_0 \cdot a + x_0 \cdot b = x_0(a + b) = x_1$$

Figure 3: Summary of parallel edges – distributive law

Dissolving a feedback loop (Figure 4): In order to eliminate the node x_1, be first the functions multiplied on the edges along the forward path. Next, forming the product of the individual loop gains. This is the signal-flow graph of two edges $a \cdot b$ and $b \cdot c$, in which $b \cdot c$ is a self-referential loop. Thus, the node x_1 is removed from the graph and the feedback has been summarized in a reflexive edge:

$$x_0 \cdot a = x_1 \text{ with } x_1 \cdot b = x_2 \implies x_0 \cdot a \cdot b + x_2 \cdot b \cdot c = x_2 \implies x_0 \cdot a \cdot b = x_2(1 - b \cdot c) \implies x_1 \frac{a.b}{1-b \cdot c} = x_2$$

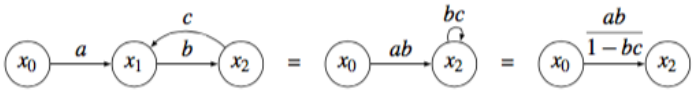

Figure 4: Dissolving a feedback loop

A reflexive edge (self-referential loop) can be eliminated, in which one by one divides the product of the functions on the

edges toward the reflective edge minus the product of the functions on the reflexive edges.

For more reflexive edges can use the same procedure. In Figure 5, the resolution reflexive edge is shown with the corresponding weights (Samuel et al. 1956, Brzozowski et al. 1963).

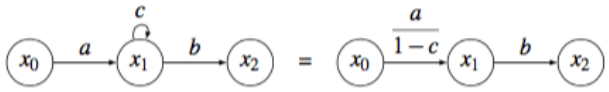

Figure 5: Dissolving a reflexive edge

3. Analysis of Common X-circuit

The Common X circuit (Figure 6) is chosen as an example of the determination of the signal flow graph in the course of work. Therefore, at this point the members of the small-signal model are explained:

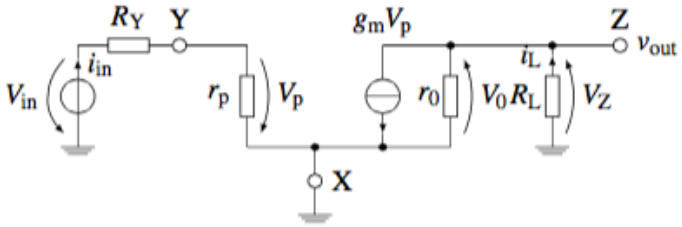

Figure 6: Small signal equivalent circuit of the CX-circuit

V_{in} is the input voltage, V_Z is the output voltage, R_Y is a lead resistance the internal resistance of the voltage source, r_p the baseband resistance of a BJT, g_m is the transconductance or the steepness of the CX circuit with $g_m = i_{out}/V_{in}$.

To apply now the method SFG, the circuit is divided into partial circuits. The intention in the division is to reduce the complexity of the analysis and to win by the sub-steps a better and clearer view of the functioning of the structure. The small-signal equivalent circuit diagram of the CX circuit can be divided into two parts following circuits: In order to simplify the effort of calculation, in the first step the circuit is broken. This results in two subcircuits (Figure 7). The first subcircuit is a simple voltage divider.

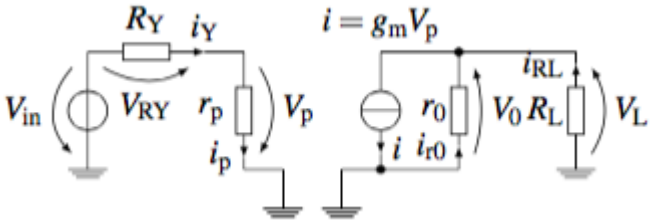

Figure 7: Small signal equivalent circuit of the CX-circuit in separate form

Based on the above considerations can now be derived for the first subcircuit of the signal-flow graph (Figure 8). It is desirable that the total voltage V_{in} of the voltage source drop across the resistor r_P. In reality, however, a small part of the voltage at the to much smaller resistance R_Y drops. The desired voltage at the resistor r_P can thus be adjusted with the resistance R_Y. Thus, the mesh equation for the first sub-circuit can be established:
$V_P = V_{in} - V_{R_Y}$. Depending on the resistance r_P is generated by the voltage V_P of the current i_P. The material equation is: $i_P = V_P \cdot \frac{1}{r_P}$; $V_{R_Y} = i_Y \cdot R_Y$; $i_P = i_Y$.

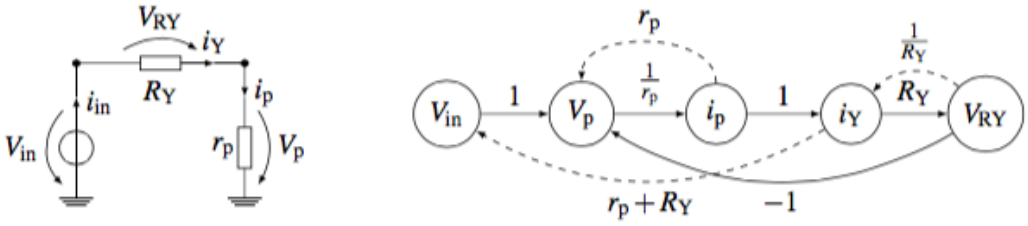

Figure 8: First subcircuit (left) of the CX-circuit and SFG (right) of the first partial circuit

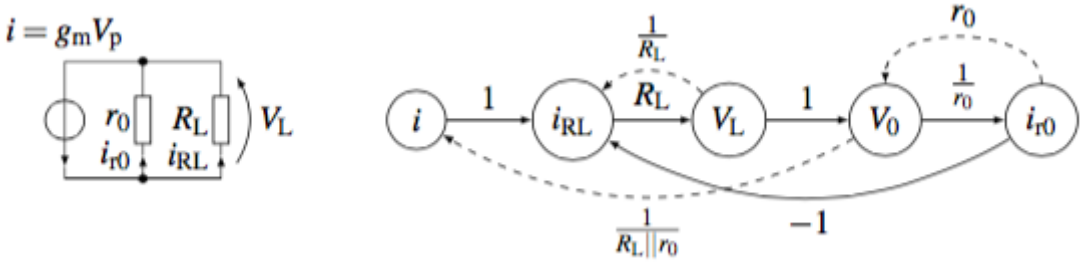

Figure 9: (Left) Second subcircuit of CX-circuit and (right) SFG of the second subcircuit

The current i_P flowing through the resistor R_Y and generates the voltage V_{R_Y}.Thus, the signal-flow graph of the first partial circuit may be formed by expansion of the signal flow graph of the ideal case without R_Y. This only needs around the edge (i_Y, V_{R_Y}) of the circuit to be supplemented. The dashed edges complement the axiomatic identity of the signal-flow graph.

When partitioning the common X-circuit, the second subcircuit between the nodes X and Z in Figure 6 is a current divider. In reality, not all of the current i of the source through the load resistor R_L:

$$i_{R_L} = i - i_{r_0}; i_{r_0} = V_0 \cdot \frac{1}{r_0}; V_L = V_0; V_L = i_{R_L} \cdot R_L.$$

Thus, the total current i can flowing through the load resistor R_L, the resistance r_0 would be infinite. But the resistance r_0 not infinitely large, flowing through it is a small portion of the source current.

The current i_{R_L} through the load resistor R_L can be adjusted by the appropriate choice of resistance r_0 or reduced by this resistance. Thus, the nodes usually can be placed. The current i_{R_L} generated at the load resistor R_L voltage V_L which is equal to the voltage drop across r_0. With the mesh analysis, this relationship can be traced. The voltage across resistor r_0 generates the current i_{r_0} which acts back to the current i_{R_L} through a negative feedback. In summary, the node and mesh and the material equations for the second subcircuit can now be set up. Extending the signal flow graph of the simple circuit around the edge (V_0, i_{r_0}) of the circuit based on the above equations, then there is the signal flow graph of the second subcircuit. The material equations can be inverted. To make the signal flow graphs of CX-circuit, the individual subgraph must be combined into a graph.

The current source i is a voltage controlled current source. It is controlled by the voltage V_P. The current is determined by $i = g_m.V_P$. In order for the two signal flow graph can about the relationship between the current source i and the voltage V_P interconnected (V_{in} (source), i_{R_L} (sink), i_P and V_L states).

4. Conclusion

The SFG analysis can offer a faster and more effective alternative to complex structures with the right approach and solution patterns. However, the signal-flow graph represents only a projection of the solution of the network equations. Superimposed by the inverted solution of the system all the states of the structure with self-imposed and unweighted loops are obtained. For the analysis of a network the SFG-method provides an important alternative, since you are saving in complex systems not only long calculus, but also get a suitable overview in the interaction of the system components and spare parts. The method is rarely used, and the existing literature on the subject is little. One can always encounter various problems in the analysis of a circuit that can be easily understood with the knowledge of this method and verified. The key to understanding a circuit is always their real structure, SFG is the structure faithful model, which real physics and underlying theory brings together suitable.

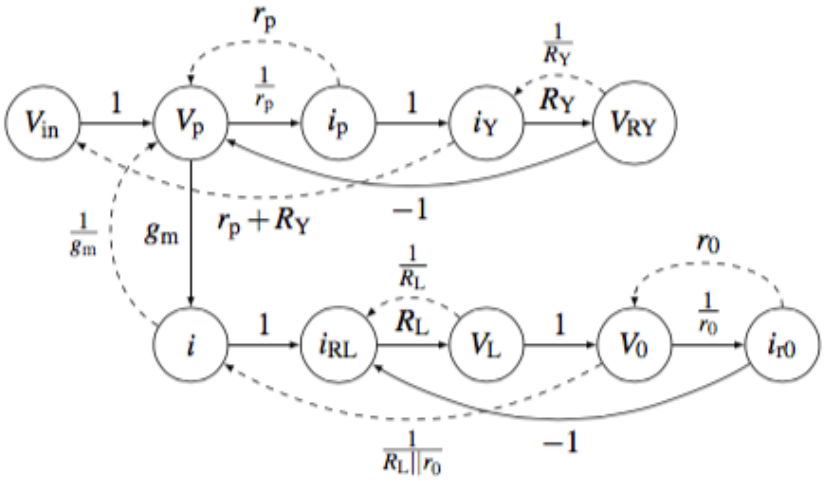

Figure 10: Signal flow graph of the CX-circuit for $r_P \to \infty$ and R_L □ r_0

References

Brzozowski J. A.; E. J. McCluskey. *Signal Flow Graph Techniques for Sequential Circuit State Diagrams.* IEEE vol. EC-12, pp. 67-76;1963.

Fakhfakh M.; M. Pierzchala; B. Rodanski. *An Improved Design of VCCS-Based Active Inducators.* Synthesis, Modeling, Analysis and Simulation Methods and Applications to Circuit Design (SMACD); 2012.

Frieder Strauß. *Grundkurs Hochfrequenztechnik*. Vieweg+Teubner Verlag, 2012.

Gaetano Palumbo und Salvatore Pennisi. *Feedback Amplifiers: Theory and Design*. Kluwer Academic Bublischers, 2003.

Richard C. Dorf and Robert H. Bishop. *Moderne Regelungssysteme*. Pearson Studium, 2006.

Samuel J. Mason. *Feedback Theory-Further Properties of Signal Flow Graphs.* IEEE, vol. 44, pp. 920-926; 1956.

Schmidt Lorenz-Peter, Gerd Schaller, Siegfried Martius: *Grundlagen der Elektrotechnik 3 Netzwerke*. Pearson Studium, München 2006